



**UNIVERSITÀ DEGLI STUDI DI NAPOLI  
“FEDERICO II”**



**Doctoral Thesis**

**“ Morphometric applications in Veterinary  
Diagnostic Imaging”**

**Coordinatore**

Prof. Paolo De  
Girolamo

**Candidato**

Dott. Dario  
Costanza

**Tutor**

Prof. Leonardo  
Meomartino



<b>List of abbreviations</b>	8
<b>List of figures</b>	10
<b>List of tables</b>	19
<b>General overview</b>	23
<b>Aims of the thesis</b>	24
<b>Summary of the Results and Conclusions</b>	26
<b>Chapter I – Introduction</b>	
1.1	The domestication and selection process 30
1.2	Age determination through the skeletal development 31
1.3	Skull morphology 35
1.4	Cardiac silhouette dimensions 39
1.5	Renal dimensions 45
1.6	References 48
<b>Chapter II – Radiographical age determination in puppies using the dimension of the ossification centers: preliminary results with the distal radius.</b>	
2.1	Abstract 62
2.2	Introduction 64
2.3	Materials and Methods 65
2.4	Results 69
2.5	Discussion 72
2.6	References 75

**Chapter III – A computed tomography based method for the assessment of canine retrobulbar cone volume for ophthalmic anaesthesia.**

3.1	Abstract	81
3.2	Introduction	83
3.3	Materials and Methods	85
3.4	Results	89
3.5	Discussion	94
3.6	References	97

**Chapter IV – Retrobulbar filling for enophthalmos treatment in dogs: technique, description and computed tomography evaluation. Preliminary cadaveric study**

4.1	Abstract	102
4.2	Introduction	103
4.3	Materials and Methods	104
4.4	Results	108
4.5	Discussion	113
4.6	References	117

**Chapter V – Computed tomographic assessment of pituitary gland dimensions and reference values in domestic short-haired cats.**

5.1	Abstract	122
5.2	Introduction	123
5.3	Materials and Methods	125
5.4	Results	131
5.5	Discussion	137
5.6	References	141

**Chapter VI – The heart-to-single vertebra radio: A new objective method for radiographic assessment of cardiac silhouette size in dogs.**

6.1	Abstract	50
6.2	Introduction	52
6.3	Materials and Methods	58
6.4	Results	65
6.5	Discussion	69
6.6	References	

**Chapter VI - Ultrasonographic measurement of kidney-to-aorta parameters in Whippets**

7.1	Abstract	147
7.2	Introduction	148
7.3	Materials and methods	150
7.4	Results	155
7.5	Discussion	160
7.6	References	164

ANOVA,	one-way analysis of variance
AoD,	aortic luminal diameter;
AoDL,	aortic luminal diameter on longitudinal scan;
AoDT,	aortic luminal diameter on transversal scan;
ASCVP,	American Society for Veterinary Clinical Pathology
BA,	brain area
CCC,	concordance correlation coefficient;
CI,	confidence interval;
CLSI,	Clinical Laboratory and Standards Institute
CrCa,	craniocaudal radiographic view
CT,	computed tomography;
DICOM,	digital imaging and communications in medicine;
DROC,	distal radius ossification center
DSH,	domestic short-haired cats
HSD test,	Tukey's honest significance difference test
HSVR,	heart to single vertebra ratio;
HSVR <sup>T4</sup> ,	heart to single vertebra ratio determined using the fourth thoracic vertebra;
HSVR <sup>T5</sup> ,	heart to single vertebra ratio determined using the fifth thoracic vertebra;
HSVR <sup>T6</sup> ,	heart to single vertebra ratio determined using the sixth thoracic vertebra;
HSVR <sup>T7</sup> ,	heart to single vertebra ratio determined using the seventh thoracic vertebra;
HSVR <sup>T8</sup> ,	heart to single vertebra ratio determined using the eighth thoracic vertebra;
HU,	Hunsfield units
ICC,	intraclass correlation coefficient;
IGF-1,	insuline-like growth factor-1
KL,	kidney length.
kVp,	Kilovoltage peak;
LA,	cardiac long axis;
M <sub>1</sub> ,	CT-based method 1;
M <sub>2</sub> ,	CT-based method 2;
mA,	milliamperes;
MAE,	mean absolute error;
ML,	mediolateral radiographic view
MPR,	multiplanar reconstruction;

## List of abbreviations

MRI,	Magnetic Resonance Imaging
OC,	ossification center
P:B ratio,	pituitary-to-brain ratio
PH,	pituitary height
PHS,	maximal pituitary height visible on the sagittal plane
PHT,	maximal pituitary height visible on the transverse plane
PL,	pituitary length
PW,	pituitary width
SA,	cardiac short axis;
SD,	standard deviation;
T4,	fourth thoracic vertebra;
T5,	fifth thoracic vertebra;
T6,	sixth thoracic vertebra;
T7,	seventh thoracic vertebra;
T8,	eighth thoracic vertebra;
VHS,	vertebral heart size;
VTBI,	volume to be injected
WL,	window level;
WW,	window width.

**FIGURE 1.1** Sequential stages (A–E) in enchondral ossification leading to the formation of a long bone. The histological appearance of a region where is replaced by bone is illustrated. From McGeady, et al.,- Veterinary Embryology 2nd ed. – Chapter 17 Muscular and skeletal system, modified.

**FIGURE 1.2** Determination of the cephalic index using CT dorsal 3D volume rendering images of canine skull: (A) brachycephalic, (B) dolichocephalic and (C) mesocephalic. The cephalic index, is computed by multiplying the cranial width (blue lines) by 100 and dividing the product by the cranial length (red lines).

**FIGURE 1.3** Computed tomography transverse postcontrast images of the brain in two different dogs with confirmed pituitary adenoma. In (A) the pituitary adenoma is readily visible (macroadenoma) and compress the surrounding brain parenchyma. In (B) there is a subtle increase in pituitary dimensions with a pituitary-to-brain (P:B) ratio of 0.37. In dogs a P:B ratio > 31 is suggestive of enlarged pituitary gland.

**FIGURE 1.4** Left-lateral thoracic radiographs in an Afghan Hound (A), Mixbreed dog (B) and French Bulldog (C) illustrating the effect of body constitution on the appearance of the cardiac silhouette.

**FIGURE 1.5** Dorsal-ventral (DV) thoracic radiograph illustrating the cardio-thoracic index proposed by Hamlin. Normally, the distance between the left ventricular free-wall and the left thoracic wall (blue line) is approximately equal to the distance between the right ventricular free-wall and the right thoracic wall (yellow line). Similarly, the left ventricular free wall (orange line) extends as far to the left of the middle as the right ventricular free-wall (green line) extends. In healthy dogs, the total expanse of both right and left sides of the heart (green and orange lines respectively) is equal to less than 65% of the total transversal width of the thorax (pink line).

**FIGURE 1.6** Left-lateral thoracic radiograph in a mixed breed dog depicting the Vertebral Heart Score (VHS) method. The cardiac long axis (red line) is measured from the tracheal bifurcation (carina) to the cardiac apex. The cardiac short axis is measured perpendicular to the long axis at the point of maximal cardiac silhouette width. To calculate VHS, the two axes are repositioned over the thoracic vertebrae starting from the cranial endplate of T4. The VHS is then expressed as the number of thoracic vertebrae (v) to the nearest 0.1v. In this dog the obtained VHS is equal to 10,1v and considered within reference values.

**FIGURE 1.7** Dorsal ultrasonographic image of the left kidney (**A**) and of the aorta (**B**) acquired just caudal to the origin of the renal artery. In (**A**) the renal length and width are measured in the point of maximal renal length. In (**B**) the maximal luminal diameter is obtained after reviewing cine-loop frames to account for pulsation of the aorta; measurement cursors were placed at the margin of the lumen excluding the vessel walls.

**FIGURE 2.1** Close up view of the DROC in a Cavalier King Charles Spaniel (**A**), Golden Retriever (**B**) and Bullmastiff (**C**). The DROC area is obtained by multiplying the DROC width (red lines) by the height (white lines)

**FIGURE 2.2** Correlation between DROC area (in  $\text{mm}^2$ ) and age (in days) in all the dogs included in the final sample. From day 60<sup>th</sup> there are two different growth trends.

**FIGURE 2.3** Linear correlation between DROC area ( $\text{mm}^2$ ) and age (in days) for medium/large-sized dogs.

**FIGURE 2.4** Logarithmic correlation between DROC area ( $\text{mm}^2$ ) and age (in days) for medium/large-sized dogs.

**FIGURE 3.1** Multiplanar reconstruction of a dolichocephalic dog skull; **(A)** sagittal, **(B)** axial and **(C)** dorsal planes are displayed. The yellow line represents the sagittal plane, the violet line the axial plane and the blue line the dorsal plane. Images show the centring of the sagittal and the axial planes on the right globe, and the tilting of the dorsal plane to fully expose the retrobulbar cone and optic foramen.

**FIGURE 3.2** A representative example of the retrobulbar cone volume measurements in a dolichocephalic dog skull, made in the dorsal plane. **(A)** The anatomical landmarks used to trace the cone base diameter and the cone height are displayed: insertion points of medial and lateral rectus muscles (white asterisks); optic canal (black asterisk); 1 = medial rectus muscle; 2 = optic nerve; 3 = lateral rectus muscle. **(B)** The measurements of retrobulbar cone base diameter (white line) and retrobulbar cone height (black line).

**FIGURE 3.3** Computed tomography 3D volume rendering images of the morphology groups of three dogs' skulls: **(A)** dolichocephalic, **(B)** mesocephalic and **(C)** brachycephalic.

**FIGURE 3.4** Retrobulbar cone volume grouped by size and by skull morphology. **(A)** The distribution of retrobulbar cone volume grouped by skull size (large, medium and small). The horizontal lines refer, for each group, to the mean  $\pm$  standard deviation; *P* values were obtained using post-hoc Tukey's honest significant difference (HSD) test. **(B)** The distribution of retrobulbar cone volume grouped by skull morphology (brachycephalic, dolichocephalic and mesocephalic). The horizontal lines refer, for each group, to the mean  $\pm$  standard deviation; *P* values were obtained using post-hoc Tukey's HSD test. **(C)** The scatter plot shows the correlation between the dog's body weight (kg) and retrobulbar cone volume (mL). The straight blue line represents the regression line obtained using the least squares method, and the grey area shows the confidence band, setting confidence level at 95%.

**FIGURE 3.5** Graphical representation of the prediction sum of squares associated with estimated nested model; *P* values refer to the analysis of variance comparison between models

**FIGURE 4.1** (A) Dorsal-oblique, (B) transverse and (C) dorsal post-injection MPR image of the skull of a 17-year-old male mixed-breed dog. Soft tissue algorithm (manually windowed to WW = 350, WL = 40), slice thickness 0.625 mm, kVp 120, mAs 220. (A) In  $M_1$ , the eyeball displacement was evaluated on a dorsal-oblique plane, drawing a line from the optic foramen to the ipsilateral corneal surface (red lines). (B) In  $M_2$ , the lateral displacement was assessed on the transverse plane, drawing a line from the frontal to the zygomatic bone (black lines) and then from this line to the corneal surface (red lines), while the rostral displacement was evaluated on the dorsal plane (C), drawing a line from the maxillary to the zygomatic bone (black lines) and then from this line to the corneal surface (red lines). The contrast media mixed with the viscoelastic solutions (black arrowheads) is visible within the retrobulbar space.

**FIGURE 4.2** Scatter plot comparing the rostro-lateral displacement in millimeters (mm) between the pre- and post-injection groups using Method 1 ( $M_1$ ). The solid black lines represent the mean

**FIGURE 4.3** Scatter plots comparing the lateral (A) and rostral (B) displacement in millimeters (mm) between the pre- and post-injection groups using Method 2 ( $M_2$ ). The black solid lines represent the mean.

**FIGURE 5.1** (A-C) transverse and (D) sagittal soft tissue algorithm postcontrast CT images of the skull of a twelve-month-old DSH cat. (A), Pituitary height (blue line) measured on the transverse plane (PHT) at the level of the pituitary fossa, perpendicular to the basisphenoid bone. (B), Brain area (BA, green line) measured on the transverse plane, at the same level of the PTH using an automated segmentation tool. (C), Pituitary width (red line) measured on the transverse plane (PW) at the point of maximal width of the gland. (D), Pituitary height (blue line) measured on the sagittal plane (PHS) perpendicular to the basisphenoid bone and pituitary length (PL, red line) measured where the maximal length of the pituitary gland was visible and parallel to the basisphenoid bone. (A, C, D) manually windowed to WW = 455, WL = 234; (B) manually windowed to WW = 2000, WL = 800. Ca: Caudal; L: Left; R: Right; Ro: Rostral

**FIGURE 5.2** Bland-Altman plot comparing measurements of the pituitary gland height measured in the transverse (PHT) and sagittal (PHS) plane. The  $y$ -axis shows the difference between the two measurements, and the  $x$ -axis shows the average. The blue dotted lines represent the 95% confidence intervals, and the red dotted line represents the bias.

**FIGURE 6.1** Representative right lateral thoracic radiographic image (kVp 80; mAs 4) of a mixed-breed dog depicting the measurements of the length of each single vertebral body between T4 and T8, including the corresponding caudal intervertebral disc spaces (black and white dotted arrows labelled T4–T8). The cardiac long axis (LA) and short axis (SA) were measured as described by Buchanan and Bücheler. In this method, the LA (doubled-headed black arrow) was traced from the ventral border of the carina to the cardiac apex and the SA (doubled-headed white arrow) was traced perpendicular to LA at the point of the maximum width of the cardiac silhouette, and then transposed ventral to the column starting from the T4 cranial endplate.

**FIGURE 6.2** Lin's concordance correlation coefficient (CCC) and related Bland–Altman plots. **(A–E)** Lin's CCC comparing VHS with HSVRI determined using T4 **(A)**, T5 **(B)**, T6 **(C)**, T7 **(D)** and T8 **(E)**. The *y*-axes show the VHS index, and the *x*-axes show the HSVR. The continuous lines represent the lines of perfect agreement (i.e. the ideal condition where HSVR equals VHS), the dashed lines represent the estimated least squares lines, and the red dots represent outliers. **(F–J)** Bland–Altman plots comparing VHS with HSVR obtained using T4 **(F)**, T5 **(G)**, T6 **(H)**, T7 **(I)** and T8 **(J)**. The *x*-axes show the mean of both measurements, the *y*-axes show the difference between the two measurements, the dashed lines represent the 95% confidence intervals, and the continuous lines represent the bias.

**FIGURE 7.1** (A) Measurement of the kidney length (7.15 cm) on a dorsal ultrasound scan (patient in right lateral recumbency; multifrequency microconvex probe working at 6,5 MHz. (B) The abdominal aorta is scanned from the left side and the aortic luminal diameter is measured just caudal to the emergence of the left renal artery. The aortic luminal diameter is measured on longitudinal (1.13 cm) and transversal (1.11 cm) scans by placing the electronic calipers at the border of the lumen, after excluding the vessel walls.

**FIGURE 7.2** Correlation between kidney length (in cm) and bodyweight (in kg).

**FIGURE 7.3** (A) Correlation between aortic luminal diameter measured on longitudinal scans (AoDL) and age (in months) of male Whippets. (B) Correlation between the aortic luminal diameter measured on transversal scans (AoDT) and age (in months) of female Whippets.

**FIGURE 7.4** (A) Bland–Altman plot comparing the aortic luminal diameters, measured on longitudinal and transversal scans (AoDL and AoDT). (B) Bland–Altman plot comparing the kidney-to-aorta ratio obtained from longitudinal and transversal scans of the abdominal aorta (KL/AoDL and KL/AoDT). The *y*-axis shows the difference between the two measurements and the *x*-axis shows the average of both measurements. The dotted lines represent the 95% confidence intervals and the dashed line represents the bias

**TABLE 2.1** Secondary ossification centers (OCs) visible in the considered period (7<sup>th</sup> – 120<sup>th</sup> day) that can be evaluated with the adopted radiographic protocol.

**TABLE 4.1** Descriptive statistics for M<sub>1</sub> pre- and post- retrobulbar injection. Abbreviations: CI, confidence interval; GROUPED; grouped data of right and left eyeballs; POST, post-injection; PRE, pre-injection; LE, left; MIN, minimum; MAX, maximum; RT, right; SD, standard deviation.

**TABLE 4.2** Descriptive statistics for M<sub>2</sub> pre- and post-retrobulbar injection. Abbreviations: CI, confidence interval; GROUPED; grouped data of right and left eyeballs; POST, post-injection; PRE, pre-injection; LE, left; LD, lateral displacement of the eyeball; MIN, minimum; MAX, maximum; RD, rostral displacement of the eyeball; RT, right; SD, standard deviation.

**TABLE 5.1** Intraclass correlation coefficients (ICC), relative 95% confidence intervals and *P*-values for the inter-observer reliability test. Abbreviations: PHT: pituitary height in the transverse plane; PHS: pituitary height in the sagittal plane; PL: pituitary length; PW: pituitary width; BA: brain area.

**TABLE 5.2** Intraclass correlation coefficients (ICC), relative 95% confidence intervals and *P*-values for the intra-observer reliability test. Abbreviations: CI, confidence interval; BA, brain area; ICC, intraclass correlation coefficient; P:B ratio, pituitary gland height to brain area ratio; PHS, maximal pituitary height on the sagittal plane; PHT, maximal pituitary height on the transverse plane; PL: pituitary length; PW: pituitary width

**TABLE 5.3** Mean  $\pm$  standard deviation, upper and lower limits of the reference value (and corresponding 90% CI) of the pituitary gland linear measurements, brain area and pituitary-to-brain ratio. Abbreviations. CI, confidence interval; BA, brain area; Max, maximum; Min, minimum; P:B ratio, pituitary gland height to brain area ratio; PHS, maximal pituitary height on the sagittal plane; PHT, maximal pituitary height on the transverse plane; PL: pituitary length; PW: pituitary width; SD, standard deviation.

**TABLE 5.4** Mean  $\pm$  standard deviation, upper and lower limits of the reference value (and corresponding 90% CI) of the pituitary gland linear measurements, brain area and pituitary-to-brain ratio. Abbreviations. CI, confidence interval; BA, brain area; Max, maximum; Min, minimum; P:B ratio, pituitary gland height to brain area ratio; PHS, maximal pituitary height on the sagittal plane; PHT, maximal pituitary height on the transverse plane; PL: pituitary length; PW: pituitary width; SD, standard deviation.

**TABLE 6.2** Reasons for thoracic radiography for included dogs and numbers (%) of dogs in each reason category

**TABLE 6.2** Intraclass correlation coefficients for inter-observer agreement among the three observers. Abbreviations: CI, confidence interval; ICC, intraclass correlation coefficient; HSVR<sup>T4</sup>, heart to single vertebra ratio determined using the fourth thoracic vertebra; HSVR<sup>T5</sup>, heart to single vertebra ratio determined using the fifth thoracic vertebra; HSVR<sup>T6</sup>, heart to single vertebra ratio determined using the sixth thoracic vertebra; HSVR<sup>T7</sup>, heart to single vertebra ratio determined using the seventh thoracic vertebra; HSVR<sup>T8</sup>, heart to single vertebra ratio determined using the eighth thoracic vertebra; VHS, vertebral heart size index

**TABLE 6.3** Intraclass correlation coefficients for intra-observer agreement between the three observers. Abbreviations: CI, confidence interval; ICC, intraclass correlation coefficient; HSVR<sup>T4</sup>, heart to single vertebra ratio determined using the fourth thoracic vertebra; HSVR<sup>T5</sup>, heart to single vertebra ratio determined using the fifth thoracic vertebra; HSVR<sup>T6</sup>, heart to single vertebra ratio determined using the sixth thoracic vertebra; HSVR<sup>T7</sup>, heart to single vertebra ratio determined using the seventh thoracic vertebra; HSVR<sup>T8</sup>, heart to single vertebra ratio determined using the eighth thoracic vertebra; VHS, vertebral heart size index

**TABLE 7.3** Descriptive statistics for the kidney lengths, aortic luminal diameter and the kidney-to-aorta ratios in a sample of clinically normal Whippets. Values in the sample were normally distributed. Abbreviations: KL= kidney length; AoDL= aortic luminal diameter measured on longitudinal scans; AoDT= aortic luminal diameter measured on transversal scans; KL/AoDL= kidney-to-aorta ratio obtained from longitudinal scans of the abdominal aorta; KL/AoDT= kidney-to-aorta ratio obtained from transversal scans of the abdominal aorta; SD= standard deviation; 95% CI= confidence interval; Min= minimum ; Max= maximum

## GENERAL OVERVIEW

The morphological diversity within the canine and feline species constitutes a daily challenge for veterinarians. In addition, to knowing specific or prevalent pathologies within a breed, the clinician must discern between normal anatomical variations and pathological findings. Diagnostic Imaging is particularly susceptible to such variations. The wide fluctuation among different breeds makes absolute measures such as length, height, and thickness unreliable, as linear measurements considered pathological in one breed may be considered within the normality in others. To address this breed-related variation, over the years, different morphometric indices, where the dimensions of a given organ or anatomical structure are normalized with respect to a different organ or anatomical structure, have been proposed. Nevertheless, fluctuations within the proposed normal values are observed. Consequently, attempts have been made to establish narrower reference intervals using samples consisting of specimens of the same breed or breeds with overlapping morphological features.

This thesis addresses different topics linked by the common thread of morphometric applications in small animals Diagnostic Imaging.

The thesis is structured in two different parts. The introduction illustrates the various morphotypes of canines and felines created through human selection, the specific pathologies resulting from this process relevant to the research aims, and the most frequent morphometric measurements performed during ultrasonographic, radiographic, and computed tomographic exams of canine and feline patients. The second part illustrates the results presented as journal articles or conference contributions.

### AIMS

The aims of this thesis were:

1. To describe a new radiographic method that provide a more accurate age estimation in puppies, through the evaluation of OCs development, in particular the distal radius ossification centre (DROC).
2. To determine a comprehensive formula for calculating the retrobulbar cone volume in dogs with different skull morphologies (brachycephalic, dolichocephalic and mesaticephalic) and, consequently, the volume of the local anaesthetic to be injected for optimal retrobulbar anaesthesia.
3. To describe and evaluate the feasibility of the retrobulbar filling, a new technique for enophthalmos treatment, assessing the eyeball displacement and the position of the injected material in the retrobulbar space by means of two different CT-based methods.
4. To establish reference values for pituitary linear dimensions (height, width, and depth) and pituitary-to-brain (P:B) ratio in domestic short-haired cats. Additionally, to evaluate the effect of age, body weight, and sex on pituitary dimensions and the P:B ratio. Finally, to assess the intra- and inter-observer agreement between two observers with different levels of expertise.

5. To describe a new objective method for radiographic assessment of cardiac silhouette dimensions in patients where VHS cannot be determined, due to alterations affecting the thoracic vertebral bodies or intervertebral disc spaces, assess the level of agreement between the new method and VHS and to evaluate the intra- and inter-observer agreement among three observers with different levels of experience.
  
6. To determine cut-off values of the kidney-to-aorta ratio in healthy Whippets, compare the results with the previously published reference values, and investigate the influence of sex, age, weight, and side on kidney-to-aorta ratio.

## SUMMARY OF RESULTS AND CONCLUSIONS

1. The measurement of the width, height, and area of the DROC, in combination with the time of its appearance, can more accurately and precisely estimate the puppy's age. Our research also found distinct growth patterns in DROC development between small and medium/large breed dogs, with small breeds slowing down growth around sixty days of age and medium/large breeds experiencing continued growth. As a result, separate mathematical formulas to estimate age in small and large/giant breed dogs are proposed.

2. Based on our data, body weight and skull morphology were the main variables required to calculate the retrobulbar cone volume in dogs. Brachycephalic and dolichocephalic dogs showed a larger retrobulbar cone volume than mesaticephalic dogs of the same weight. Consequently, the volume of the anaesthetic solution to be injected for adequate retrobulbar anaesthesia can be determined using the proposed mathematical formulas for each canine skull morphology.

3. The retrobulbar lipofilling determined a significant rostro-lateral displacement of the eyeballs and, therefore, demonstrated to be a possible technique in the enophthalmos resolutions in dogs. The supratemporal approach adopted for retrobulbar injection proved to be safe and without macroscopic and histopathological lesions to relevant retrobulbar structures. Computed tomography permitted to accurately establish the localisation of the material injected within the retrobulbar space. Both the proposed CT

methods demonstrated to be reliable for quantifying the rostro-lateral displacement of the eyeball.

4. The obtained values for pituitary linear dimensions and P:B ratio were significantly different from those previously reported. Significant correlations were found between body weight and pituitary size and between age and pituitary height and length. No differences between genders were found. Furthermore, CT pituitary linear dimensions and P:B ratio showed a good intra-operator agreement but a moderate inter-operator agreement, likely consequent to the millimetric dimensions of the gland and its relatively low contrast enhancement compared to the brain parenchyma.

5. The new proposed method, called the heart-to-single vertebra ratio (HSVR), obtained by dividing the sum of the cardiac long and short axes by the length of a single thoracic vertebral body could be determined in dogs with alterations affecting the thoracic vertebral bodies or intervertebral disc spaces, allowing an objective determination of the cardiac silhouette dimensions in these dogs. The HSVR revealed a strong correlation with VHS, especially when considering T7 and a good to excellent inter- and intra-observer agreement.

6. The proposed cut-off values for the kidney-to-aorta ratio in Whippets (6.3 – 6.9), were significantly narrower than the previously reported range (5.5 – 9.1). The obtained values did not differ between right versus left sides or male versus female sexes. This last finding was notable since the kidney lengths in Whippets exhibits marked sexual dimorphism. Additionally, there were no differences in assessing aorta diameter between the longitudinal and transversal scans. Our findings support the use of breed-specific kidney-to-aorta ratio values for characterizing abnormal renal size in canine breeds and minimize possible overlap with values obtained from healthy dogs.

## **Chapter I**

### Introduction

### **1.1 THE DOMESTICATION AND SELECTION PROCESSES IN THE DOG AND CAT**

Domestication, selective breeding for desirable traits, and propagation of specific breeds have made the dog unparalleled in its diversity among land mammals. Selective breeding has allowed dogs to adapt to various roles, such as herding, guarding, hunting, rescue, and companionship. The range of sizes among dogs extends beyond that of wolves and jackals, giving dogs the distinction of being the most morphologically diverse terrestrial mammalian species.<sup>1</sup> This diversity is demonstrated through both a high degree of variation between breeds and a high degree of similarity within breeds.<sup>2,3</sup> In the XIX century, a trend of breeding and trading dogs for specific physical and behavioral traits had become popular in Europe and the United Kingdom. The Kennel Club, founded in 1873, standardised dog breeding by categorizing them based on their lineage, appearance, and behaviour. There are over four hundred breeds of dogs worldwide, of which the Kennel Club officially recognizes approximately half.<sup>4</sup> Differently, cat domestication likely started 10 000 years ago in the Near East.<sup>5</sup> The cat probably began its association with humans as a commensal, feeding on the rodent pests that infested the grain stores of the first farmers.<sup>6</sup> In recent years, breed selection has resulted in tens of morphologically differing breeds through intentional breeding and purely dictated by aesthetic purposes. Today, the International Cat Association currently recognizes seventy-one breeds.

## 1.2 AGE DETERMINATION THROUGH THE SKELETAL DEVELOPMENT

There are two critical phases in the development of bone. The first occurs in utero, during embryonic and foetal development when bone tissue starts to form in certain regions called ossification centres (OCs). These latter develop in the approximate positions that will determine the basic skeletal pattern of the adult. The second development phase occurs in postnatal life as the animal grows. During this time, bones elongate and change shape, assuming the adult form;<sup>7</sup> besides, although the size and shape of each bone are genetically determined, its final form may be influenced by a number of environmental and dietary factors.<sup>8</sup> Bone develops by the replacement of pre-existing tissue. When it is formed in a sheet of vascular loose connective tissue, the process is called intramembranous ossification; on the contrary, when bone replaces calcified cartilage is referred to as endochondral ossification.<sup>8</sup> The latter is responsible for the development of long bones. The process begins in the embryonic stage and continues after birth until the bones reach definitive size and shape. The process of enchondral ossification begins with the formation of a cartilage model, which serves as a template for the future bone (Figure 1.1A). In the first step, chondrocytes proliferate in the region where bone formation is occurring. Then these cells differentiate and form a matrix of extracellular material (Figure 1.1B). As the matrix mineralizes, blood vessels invade the cartilage model, bringing in osteoblasts (Figure 1.1C). The osteoblasts deposit bone matrix around the chondrocytes, eventually enclosing them within small spaces called lacunae. As the bone matrix continues to be deposited, the chondrocytes in the

lacunae degenerate and are replaced by bone (Figure 1.1 D,E). This process continues until the entire cartilage model has been replaced by bone. The bones formed through endochondral ossification are composed of a dense, hard outer layer of cortical bone and a spongy inner layer of trabecular bone.<sup>9, 10</sup>

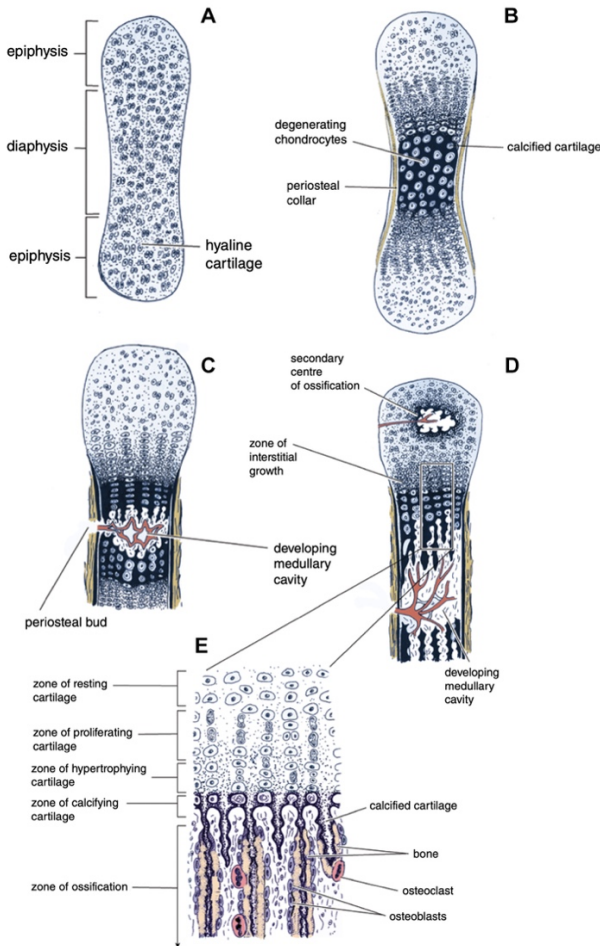


*FIGURE 1.1 Sequential stages (A–E) in endochondral ossification leading to the formation of a long bone. The histological appearance of a region where is replaced by bone is illustrated. From McGeady, et al., Veterinary Embryology 2nd ed. – Chapter 17 Muscular and skeletal system, modified.*

Differently from enchondral ossification, intramembranous ossification does not involve the replacement of a cartilage model with bone. Some mesenchymal cells differentiate into osteoblasts, producing an osteoid matrix that subsequently mineralise, forming bone spicules. When more spicules become interconnected, they form a trabecular network of cancellous bone referred to as an ossification centre.<sup>8</sup> This process is responsible for the formation of flat bones such as the mandible and skull bones.<sup>8,9</sup> Most long bones develop from at least three OCs: the primary OC is located at the diaphysis and starts during foetal life, while secondary OCs are located at the epiphyses and start their function after birth. The number of secondary OCs depends on the shape of the bone and its function. The sequence of events which leads to bone formation at the secondary OCs is similar to that described for bone formation at the primary OCs.<sup>8</sup> During the bones' growth in length, the proliferation of the reserve cartilage is balanced against the rate of osseous replacement until it is exceeded by the latter resulting in the eventual replacement of the epiphyseal plate. There is a wide variation of the times in which growth plate closure occurs in different bones within a given animal, species and breed.<sup>11</sup> The modality of choice for determining age in human forensic medicine is through the examination of physeal and OCs development and closure rates. This technique is effective for individuals ranging in age from birth to around 24-26 years and is well-documented in radiographic atlases, which illustrate the gradual progression of various bones as a person ages.<sup>12, 13</sup> Similarly, in veterinary medicine, during the first half of the XX century, the appearance and closure rate of OCs has been investigated to understand their implication in the pathogenesis of skeletal growth diseases.<sup>16-25</sup> Unfortunately, from those

studies, the OCs exhibit a wide range of appearance and fusion and, consequently, were quite unreliable in age estimation.<sup>14, 15</sup> This wide variation in veterinary patients are related, for example, to the different times in reaching skeletal maturity. Small breed dogs reach skeletal maturity before one year, while large and giant breeds can take up to sixteen months. Furthermore, even puppies within the same breed can show variations in skeletal growth due to factors such as nutrition, congenital disorders, or acquired diseases.<sup>11</sup> Due to OCs' variability, the use of dentition as an alternative method for age determination for forensic purposes was proposed. However, dental eruption times are only reliable in animals at around 6-7 months.<sup>15</sup> Furthermore, various external factors such as poor diet, infectious diseases, antibiotic therapies or dental care can cause wear and tear on the teeth, leading to missing, decayed, or damaged teeth, making age determination via dentition unreliable.<sup>16</sup> This is particularly relevant in forensic cases as neglected animals often have poor diets and malnourishment, resulting in poor dentition.<sup>11</sup> More recently, with the rise in illegal puppy trafficking and growing public awareness, there has been renewed interest in the radiographic assessment of OCs to estimate the age of dogs.<sup>14, 17, 18</sup>

### 1.3 SKULL MORPHOLOGY

The phenotypic differences within the canine and, to a lesser extent, in feline species can be well-represented by their skull shape. The wide range of morphological variation among these breeds is so distinct that skull shape is often used as a defining characteristic of a breed.<sup>19</sup> Currently, dogs and cats are classified into three groups: dolichocephalic, mesaticephalic, and brachycephalic, based on the cephalic index, computed by multiplying the cranial width (measured from zygomatic arch to zygomatic arch) by 100 and dividing the product by the cranial length (from the occiput to the prosthion).<sup>20-25</sup> According to Evans and De Lahunta<sup>26</sup> brachycephalic dog breeds, such as French Bulldog, Pug, etc., or cat breeds, such as Persian, Himalayan, etc. have shorter and larger skulls with a cephalic index approximately of 81 or greater (Figure 1.2 A). On the opposite end of the spectrum, there are dog breeds such as Collie, Greyhound, Irish Wolfhound, etc. or cat breeds such as Siamese, Abyssinian, Sphynx, etc. which have a dolichocephalic appearance, showing a more significant development of the skull's longitudinal axis with a cephalic index of 39 or smaller (Figure 1.2 B). Between the two extremes of brachycephaly and dolichocephaly are mesaticephalic breeds. These breeds have skulls that are of intermediate length and width with a cranial index approximately of 52 (Figure 1.2 C). Examples of mesaticephalic dog breeds include Beagle, Golden Retriever, Labrador Retriever, etc. while as cat breeds, Domestic short-haired cat, Ragdoll, Russian blue, etc.

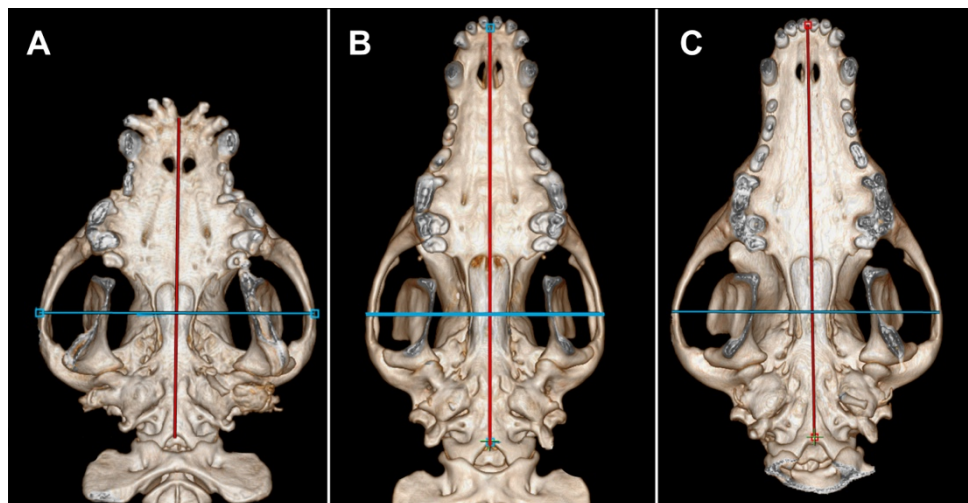


*FIGURE 1.2 Determination of the cephalic index using CT dorsal 3D volume rendering images of canine skull: (A) brachycephalic, (B) dolichocephalic and (C) mesocephalic. The cephalic index, is computed by multiplying the cranial width (blue lines) by 100 and dividing the product by the cranial length (red lines)*

The differences between skull morphotypes affect the splanchnocranium and the neurocranium and can have clinical relevance. For example, dogs with similar body weight but differing in skull morphology might display different retrobulbar cone volumes and shapes. Therefore, this variation in skull conformation must be considered when performing specific clinical procedures as the retrobulbar anaesthesia in which the volume of local anaesthetic solution to be injected can vary widely among morphotypes. Underestimating this volume can result in an ineffective block, while overestimating it can cause severe collateral effects, including toxicity, proptosis, and increased intraocular pressure.<sup>27, 28</sup> Therefore, the volume of anaesthetic solution required for retrobulbar anaesthesia should be carefully calculated. Furthermore, certain breeds (Afghan Hound, Golden Retriever,

Great Dane, Labrador Retriever, Newfoundland, Standard Poodle, Rottweiler, Weimaraner and Persian), due to refined aesthetic conformations, may also develop ocular alterations such as the entropion, caused by inherited enophthalmos. This condition, characterized by the inward turning of the eyelid (entropion) that causes traumatic corneal lesions provoked by the eyelashes and formation of a pocket in the lower conjunctival area where foreign material can accumulate and lead to chronic conjunctivitis, redness of the third eyelid, and a slight mucous discharge, known as the "medial canthal pocket syndrome". These alterations can lead to impaired vision and discomfort for the affected patient.<sup>29</sup> Many small brachycephalic breeds feature the neurocranial appearance of human turricephaly, hydrocephalus,<sup>30</sup> persistent fontanelles,<sup>31</sup> Chiari-like malformation and secondary syringomyelia.<sup>32</sup> The different cranial configurations can also alter the cut-off values established for some morphometric indices already described for the dog and cat. In particular, the detection of anatomical alterations of the pituitary gland is performed using Magnetic Resonance Imaging (MRI) or Computed Tomography (CT). In many cases, the diagnosis of pituitary macroadenoma is straightforward since the pituitary mass dorsally protrudes from the sella turcica and compresses the adjacent brain parenchyma (Figure 1.3 A). Differently, in pituitary microadenomas, there are only subtle and often not visible changes in pituitary size and contours (Figure 1.3 B).<sup>33</sup> In order to address variation in pituitary gland size between dogs and cats of different sizes and breeds, the pituitary-to-brain ratio (P:B ratio) computed by multiplying the pituitary height (in mm) by 100 and dividing the product by the brain area (in mm<sup>2</sup>) obtained on the same slice was introduced to

address variations in pituitary gland size between dogs and cats of different sizes.<sup>34-37</sup> However, it has been shown that the cut-off values for dogs and cats with different skull morphology can be different from those originally proposed. Therefore, the use of breed-specific cut-off values is necessary.<sup>38</sup>

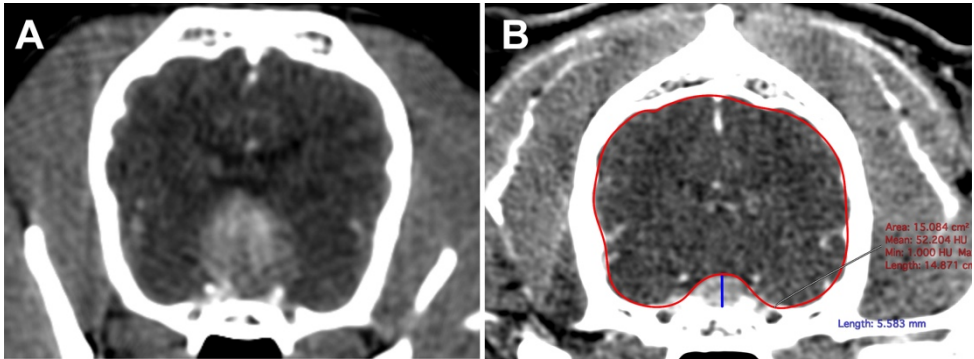


*FIGURE 1.3 Computed tomography transverse postcontrast images of the brain in two different dogs with confirmed pituitary adenoma. In (A) the pituitary adenoma is readily visible (macroadenoma) and compress the surrounding brain parenchyma. In (B) there is a subtle increase in pituitary dimensions with a pituitary-to-brain (P:B) ratio of 0.37. In dogs a P:B ratio > 31 is suggestive of enlarged pituitary gland.*

## 2.4 CARDIAC SILHOUETTE DIMENSIONS

Morphological differences between animals of different breeds also affect the evaluation of the heart. While the morphological difference between breeds has little influence on the typical appearance of a feline thoracic radiograph,<sup>39</sup> it has a considerable impact on the evaluation of canine thorax, especially in the evaluation of structures such as the mediastinum and cardiac silhouette. Breed-associated conformational variations are considered the most important cause of variation in interpreting the canine cardiac silhouette.<sup>40</sup> Dogs with wide shallow thorax (brachymorphus) have shorter, rounder cardiac silhouette at a large inclination to the spine; additionally, the cardiac silhouette has an extended contact area with the sternum mimicking right-sided cardiomegaly. On the other hand, dogs with a deep narrow thorax (dolycomorphus) have long oval cardiac silhouette with a vertical position in the thorax, almost perpendicular to the spine. Finally, in dogs with intermediate thoracic conformation (mesomorphus) the cardiac silhouette appears ovoid.<sup>40</sup> Consequently, the radiographic evaluation of cardiovascular disease in veterinary patients using is complex due to variations in individual and breed-specific characteristics (Figure 1.4).

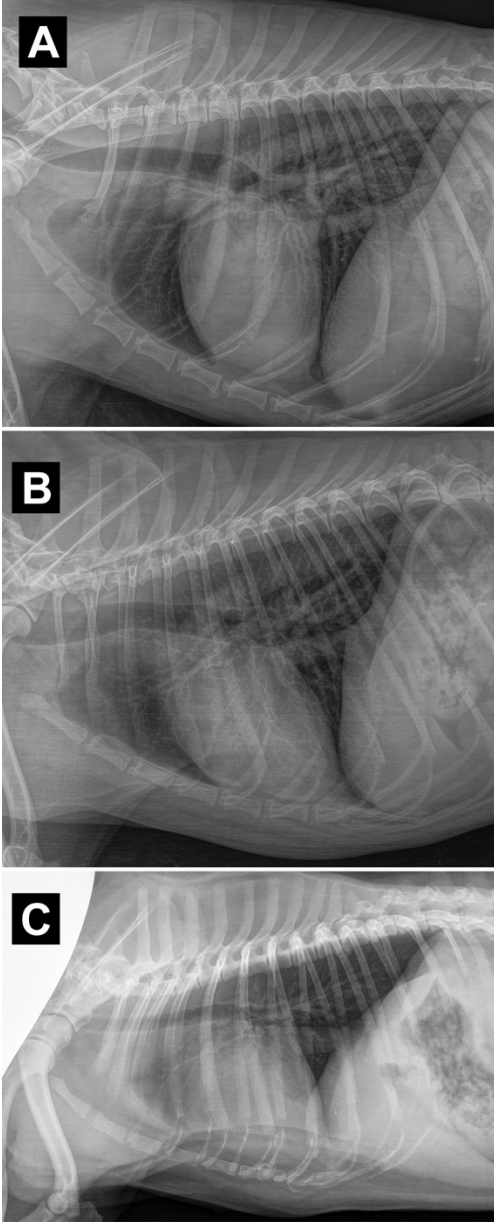


*FIGURE 1.4 Left-lateral thoracic radiographs in an Afghan Hound (A), Mixbreed dog (B) and French Bulldog (C) illustrating the effect of body constitution on the appearance of the cardiac silhouette*

Although radiography is not the gold standard for evaluating the heart in small animal practice, it remains a straightforward modality to assess cardiac dimensions, evaluate concurrent pulmonary diseases, and monitor the progression of cardiomyopathy over time.<sup>41</sup> Several methods considering ratios between the dimensions of the heart and the thorax were proposed<sup>39, 42</sup> but are applicable only within the same breed or in dogs with closely similar thoracic conformations.<sup>40, 43</sup> The cardio-thoracic index proposed by Hamlin in 1968<sup>42</sup> compared the cardiac dimensions to the thoracic width but it relies on radiographs made with a consistent technique (Figure 1.5). Minimal obliquity of projection, shifting of the cardiac apex or the expiratory phase precludes the use of this method since obtained values are artifactually increased or decreased. Additionally, the position of the diaphragm, obesity, skeletal deformities of the thorax or spine, and uneven lung lobe inflation have similar effects.<sup>44-46</sup>

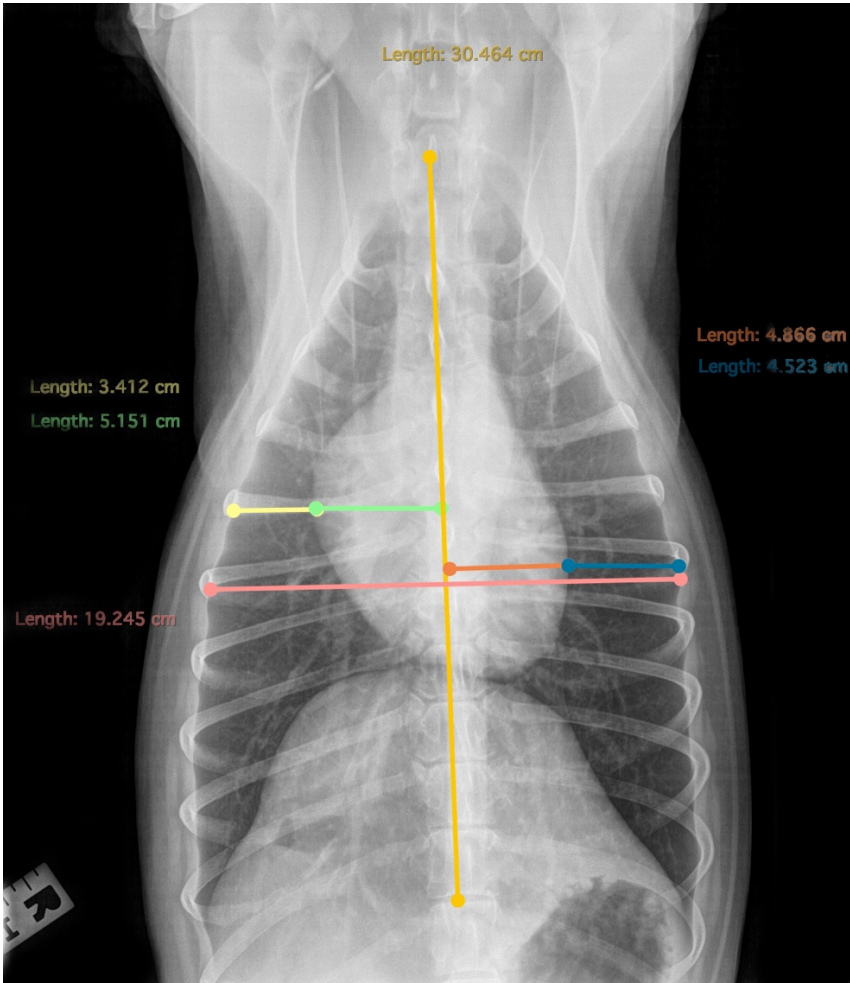


*FIGURE 1.5 Dorsal-ventral (DV) thoracic radiograph illustrating the cardio-thoracic index proposed by Hamlin. Normally, the distance between the left ventricular free-wall and the left thoracic wall (blue line) is approximately equal to the distance between the right ventricular free-wall and the right thoracic wall (yellow line). Similarly, the left ventricular free wall (orange line) extends as far to the left of the middle as the right ventricular free-wall (green line) extends. In healthy dogs, the total expanse of both right and left sides of the heart (green and orange lines respectively) is equal to less than 65% of the total transversal width of the thorax (pink line).*

In 1995, Buchanan and Bücheler described the vertebral heart score (VHS) as an objective method to estimate heart size.<sup>47</sup> To determine the VHS, the long axis of the cardiac silhouette is measured from the tracheal bifurcation to the cardiac apex. The short axis is measured perpendicular to the long axis at the point of the largest cardiac silhouette width. The obtained axes are transposed on the vertebral column starting from the cranial endplate of the fourth thoracic vertebra. The VHS value, expressed in the number of thoracic vertebrae ( $v$ ), is then obtained by the cardiac length and width sum (Figure 1.6). Dogs' normal vertebral heart score has been reported as  $9.7 \pm 0.5$  (range 8.5–10.5). The wide diffusion of the method in clinical practice is testified by the large number of scientific publications that in the following years have evaluated the method's reliability and the influence on VHS score of variables such as respiratory phase, cardiac cycle, recumbency and determined indices for individual breeds that tend to deviate from the initially reported cut-off values.<sup>48-61</sup> However, among the method's limitation, there is its inapplicability in patients with spinal abnormalities, such as *spondylosis deformans*, reduced intervertebral disc spaces or malformations, like hemivertebrae or butterfly vertebrae, which are common in elderly dogs and in brachycephalic breeds, respectively.<sup>48, 60, 62</sup>

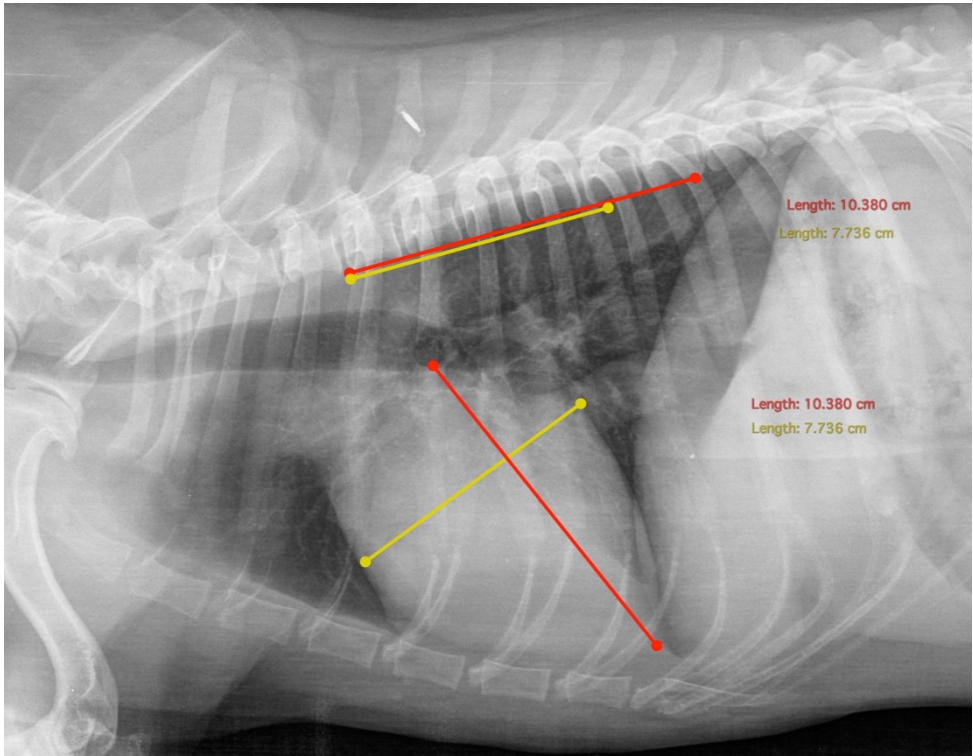


*FIGURE 1.6 Left-lateral thoracic radiograph in a mixed breed dog depicting the Vertebral Heart Score (VHS) method. The cardiac long axis (red line) is measured from the tracheal bifurcation (carina) to the cardiac apex. The cardiac short axis is measured perpendicular to the long axis at the point of maximal cardiac silhouette width. To calculate VHS, the two axes are repositioned over the thoracic vertebrae starting from the cranial endplate of T4. The VHS is then expressed as the number of thoracic vertebrae ( $v$ ) to the nearest  $0.1v$ . In this dog the obtained VHS is equal to  $10.1v$  and considered within reference values.*

## 1.5 RENAL DIMENSIONS

Variations in the patient's weight and size significantly impact the abdominal organs. As expected, larger dogs generally have larger organs than smaller dogs.<sup>63</sup> To account for this intra-specific variation, morphometric indices have been proposed. In particular, several studies have focused on determining renal size in healthy patients.<sup>64-70</sup> Some pathologic conditions, like acute kidney disease, pyelonephritis, neoplasia, and hydronephrosis, can cause slight to severe increase in kidney dimensions; others, like chronic kidney disease, hypoplasia and renal dysplasia, can determine slight to severe reduction.<sup>71</sup> Among diagnostic modalities, survey radiographs can be used to estimate kidney size by comparing the renal length to the length of the second lumbar vertebra.<sup>64</sup> However, this ratio is limited by factors such as renal depth and inclination, which can cause variable radiographic magnification and distortion. Moreover, any loss in abdominal detail, for example, due to peritoneal or retroperitoneal effusion or cachexia, can affect renal visibility.<sup>72</sup>

Nowadays, ultrasonography is considered the first level technique to evaluate the kidneys since it can provide information about size, shape, and internal structure, even in patients where radiography cannot visualize them. Additionally, it can also be used for ultrasound assisted renal fine needle aspirations, biopsies and therapeutic procedures such as ethanol sclerotherapy for renal cysts.<sup>71, 73</sup> Finally, Doppler and contrast-enhanced ultrasonography allows for functional assessment of renal blood flow.<sup>71, 74</sup> Unfortunately, still today, there is not a widely accepted method for determining renal size in dogs using ultrasounds.<sup>71</sup> Several studies have

attempted to correlate kidneys' linear dimensions or volume with body weight or surface area but have found limited success since as they are time-consuming, require sedation and therefore of limited clinical relevance.<sup>65-68</sup> More recently, two studies have tried to correlate renal dimension with other anatomical structures of the same patient.<sup>69, 70</sup> In one of these studies,<sup>69</sup> the authors correlated the renal length, width, and height with the lengths of the fifth and sixth lumbar vertebrae. The obtained renal:vertebral-length index ranged from 1.3 to 2.7, a normality range similar to the radiographic method proposed by Finco<sup>64</sup> for the radiographic evaluation. However, the proposed method faces several limitations, including the difficulty in identifying with certainty and in obtaining an accurate longitudinal scan of the vertebral bodies, the impossibility in visualizing the intervertebral spaces in patients with spondylosis deformans and the reduced vertebral length in chondrodystrophic dogs.<sup>75</sup> In 2007, Mareschal et al.<sup>70</sup> proposed the kidney-to-aorta ratio, a new method for assessing more objectively the canine renal size. In this method, the renal length is related to the aortic diameter measured just caudal to the left renal artery (Figure 1.7). This method demonstrated to have a good reproducibility, when used by different operators, and to be quick and easy to perform and therefore optimal for routinary application. The method's popularity is reflected by its inclusion in the ACVR/EVDI consensus on abdominal ultrasound, which suggests its usage for detecting renal abnormalities.<sup>76</sup> Unfortunately, the normal cut-off values proposed by the authors has a wide range (5.5 – 9.1) and, consequently, a low sensitivity and specificity. One possible reason for the wide range of normal values could be related to the sample included in the

study, represented by dogs belonging to different morphologies, breeds and different body weights.<sup>75, 77</sup>

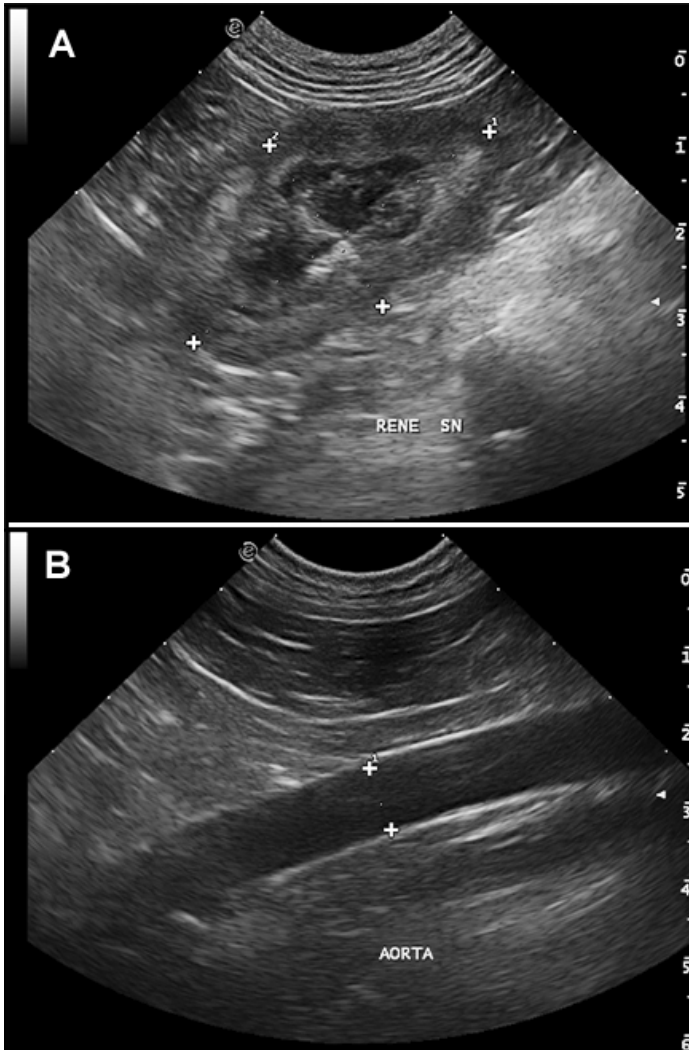


*FIGURE 1.7 Dorsal ultrasonographic image of the left kidney (A) and of the aorta (B) acquired just caudal to the origin of the renal artery. In (A) the renal length and width are measured in the point of maximal renal length. In (B) the maximal luminal diameter is obtained after reviewing cine-loop frames to account for pulsation of the aorta; measurement cursors were placed at the margin of the lumen excluding the vessel walls*

## 1.6 REFERENCES

1. Stockard CR. The genetic and endocrine basis for differences in form and behaviour as elucidated by studies of contrasted pure-line dog breeds and their hybrids. With special contributions on behaviour by OD Anderson and WT James. Amer Anat Mem. 1941.
2. Shearin AL, Ostrander EA. Canine Morphology: Hunting for Genes and Tracking Mutations. PLOS Biology. 2010;8: e1000310. 10.1371/journal.pbio.1000310
3. Wilcox B, Walkowicz C. Atlas of dog breeds of the world. New rev, 1989.
4. Club TK. Breeds A to Z. 2023 [cited 2023 26 Jan 2023]; Available from: <https://www.thekennelclub.org.uk/search/breeds-a-to-z/>
5. Driscoll CA, Menotti-Raymond M, Roca AL, Hupe K, Johnson WE, Geffen E, et al. The Near Eastern origin of cat domestication. Science. 2007;317: 519-523.
6. Kitchener A. The natural history of the wild cats: Comstock Pub. Associates, 1991.
7. Summerlee A. Bone formation and development. In: G Sumner-Smith GF (ed): Bone in Clinical Orthopedics: AO Publishing, 2002;1 - 21.

8. T. A. McGeady PJQ, E. S. Fitzpatrick, M. T. Ryan, D. Kilroy, P. Lonergan. Muscular and skeletal systems. In: T. A. McGeady PJQ, E. S. Fitzpatrick, M. T. Ryan, D. Kilroy, P. Lonergan (ed): *Veterinary Embriology*: Wiley Blackwell, 2017;195-213.
9. Berendsen AD, Olsen BR. Bone development. *Bone*. 2015;80:14-18. [10.1016/j.bone.2015.04.035](https://doi.org/10.1016/j.bone.2015.04.035)
10. McNamara L. 2.210 - Bone as a Material. In: Ducheyne P (ed): *Comprehensive Biomaterials*. Oxford: Elsevier, 2011;169-186.
11. Von Pfeil D, DeCamp C, Abood SK. The Epiphyseal Plate: Nutritional and Hormonal Influences; Hereditary and Other Disorders. *Compendium Continuing Education for Veterinarians*. 2009;31.
12. Cavallo F, Mohn A, Chiarelli F, Giannini C. Evaluation of Bone Age in Children: A Mini-Review. *Frontiers in Pediatrics*. 2021;9. [10.3389/fped.2021.580314](https://doi.org/10.3389/fped.2021.580314)
13. Indicators of Skeletal Maturity in Children and Adolescents. In: Gilsanz V, Ratib O (eds): *Hand Bone Age: A Digital Atlas of Skeletal Maturity*. Berlin, Heidelberg: Springer Berlin Heidelberg, 2005;9-17.
14. Modina SC, Andreis ME, Moioli M, Di Giancamillo M. Age assessment in puppies: Coming to terms with forensic requests. *Forensic*

Science International. 2019;297: 8-15.

<https://doi.org/10.1016/j.forsciint.2019.01.003>

15. Sutton LK, Byrd JH, Brooks JW. Age Determination in Dogs and Cats. In: Brooks JW (ed): *Veterinary Forensic Pathology, Volume 2*. Cham: Springer International Publishing, 2018;151-163.

16. Roccaro M, Peli A. Age determination in dog puppies by teeth examination: legal, health and welfare implications, review of the literature and practical considerations. *Veterinaria Italiana*. 2020;56: 149-162.

17. Modena SC, Veronesi MC, Muioli M, Meloni T, Lodi G, Bronzo V, et al. Small-sized newborn dogs skeletal development: radiologic, morphometric, and histological findings obtained from spontaneously dead animals. *BMC Veterinary Research*. 2017;13: 175. 10.1186/s12917-017-1092-6

18. Roccaro M, Diana A, Linta N, Rinnovati R, Freo M, Peli A. Limb development in skeletally-immature large-sized dogs: A radiographic study. *PLoS One*. 2021;16: e0254788. 10.1371/journal.pone.0254788

19. Schoenebeck JJ, Ostrander EA. The Genetics of Canine Skull Shape Variation. *Genetics*. 2013;193: 317-325. 10.1534/genetics.112.145284

20. Johnson D, Wilkie AOM. Craniosynostosis. *European Journal of Human Genetics*. 2011;19: 369-376. 10.1038/ejhg.2010.235
21. Seiferle E. On the topography of the brain on long and short skulls in dog breeds. *Acta Anat (Basel)*. 1966;63: 346-362.
22. Brehm H, Loeffler K, Komeyli H. Skull forms in dogs. *Anat Histol Embryol*. 1985;14: 324-331. 10.1111/j.1439-0264.1985.tb00828.x
23. Onar V, Ozcan S, Pazvant G. Skull typology of adult male Kangal dogs. *Anat Histol Embryol*. 2001;30: 41-48. 10.1046/j.1439-0264.2001.00292.x
24. Schmidt MJ, Neumann AC, Amort KH, Failing K, Kramer M. Cephalometric measurements and determination of general skull type of Cavalier King Charles Spaniels. *Vet Radiol Ultrasound*. 2011;52: 436-440. 10.1111/j.1740-8261.2011.01825.x
25. Koch D, Wiestner T, Balli A, Montavon P, Michel E, Scharf G, et al. Proposal for a new radiological index to determine skull conformation in the dog. *Schweiz Arch Tierheilkd*. 2012;154: 217-220. 10.1024/0036-7281/a000331
26. Evans H. The skeleton In: Evans HE, de Lahunta A, eds. *Miller's Anatomy of the Dog* St Louis, MO: Saunders. 2013: 80-157.

27. Klaumann PR, Moreno JCD, Montiani-Ferreira F. A morphometric study of the canine skull and periorbita and its implications for regional ocular anesthesia. *Veterinary Ophthalmology*. 2018;21: 19-26.  
<https://doi.org/10.1111/vop.12471>
28. Giuliano EA. Regional Anesthesia as an Adjunct for Eyelid Surgery in Dogs. *Topics in Companion Animal Medicine*. 2008;23: 51-56.  
<https://doi.org/10.1053/j.ctsap.2007.12.007>
29. Rubin LF. *Inherited Eye Diseases in Purebred Dogs*: Williams & Wilkins, 1989.
30. Schmidt M, Ondreka N. Hydrocephalus in Animals. In: Cinalli G, Özek MM, Sainte-Rose C (eds): *Pediatric Hydrocephalus*. Cham: Springer International Publishing, 2019;53-95.
31. Kiviranta AM, Rusbridge C, Lappalainen AK, Junnila JJT, Jokinen TS. Persistent fontanelles in Chihuahuas. Part I. Distribution and clinical relevance. *J Vet Intern Med*. 2021;35: 1834-1847. 10.1111/jvim.16151
32. Knowler SP, Galea GL, Rusbridge C. Morphogenesis of Canine Chiari Malformation and Secondary Syringomyelia: Disorders of Cerebrospinal Fluid Circulation. *Frontiers in Veterinary Science*. 2018;5: 10.3389/fvets.2018.00171

33. Hecht S, Schwarz T. Pituitary Gland. *Veterinary Computed Tomography*, 2011;197-203. Wiley
34. Kooistra HS, Voorhout G, Mol JA, Rijnberk A. Correlation between impairment of glucocorticoid feedback and the size of the pituitary gland in dogs with pituitary-dependent hyperadrenocorticism. *J Endocrinol*. 1997;152: 387-394. 10.1677/joe.0.1520387
35. Wallack ST, Wisner ER, Feldman EC. Mensuration of the pituitary gland from magnetic resonance images in 17 cats. *Vet Radiol Ultrasound*. 2003;44: 278-282. 10.1111/j.1740-8261.2003.tb00455.x
36. Nadimi S, Molazem M, Jarolmasjed S, Esmaili Nejad MR. Volumetric evaluation of pituitary gland in dog and cat using computed tomography. *Vet Res Forum*. 2018;9: 337-341. 10.30466/vrf.2018.33073
37. Tyson R, Graham JP, Bermingham E, Randall S, Berry CR. Dynamic computed tomography of the normal feline hypophysis cerebri (Glandula pituitaria). *Vet Radiol Ultrasound*. 2005;46: 33-38. 10.1111/j.1740-8261.2005.00006.x
38. Häußler TC, von Pückler KH, Thiel C, Enderlein S, Failing K, Ondreka N, et al. Measurement of the normal feline pituitary gland in brachycephalic and mesocephalic cats. *J Feline Med Surg*. 2018;20: 578-586. 10.1177/1098612x17723774

39. Lord PF. Quantitative Left Ventricular Cineangiography in the Dog: Measurement and Usefulness of Left Ventricular Volume. *Veterinary Radiology*. 1977;18: 51-57.
40. Suter PF, Lord PF. Cardiac Diseases. In: Suter PF (ed): *Thoracic Radiography: A Text Atlas of Thoracic Diseases of the Dog and Cat*. Wettswil, Switzerland: Peter F. Suter, 1984;351 - 516.
41. Bahr R. Chapter 35 - Canine and Feline Cardiovascular System. In: Thrall DE (ed): *Textbook of Veterinary Diagnostic Radiology (Seventh Edition)*: W.B. Saunders, 2018;684-709.
42. Hamlin R. Analysis of the cardiac silhouette in dorsoventral radiographs from dogs with heart disease. *Amer Vet Med Ass J*. 1968.
43. Wyburn R, Lawson D. Simple radiography as an aid to the diagnosis of heart disease in the dog. *Journal of Small Animal Practice*. 1967;8: 163-170.
44. Silverman S, Suter P. Influence of inspiration and expiration on canine thoracic radiographs. *Journal of the American Veterinary Medical Association*. 1975;166: 502-510.
45. Buchanan JW. Radiographic aspects of patent ductus arteriosus in dogs before and after surgery. *Acta Radiologica Diagnosis*. 1972;13: 271-278.

46. Suter P, Lord P. A critical evaluation of the radiographic findings in canine cardiovascular diseases. *Journal of the American Veterinary Medical Association*. 1971;158: 358-371.
47. Buchanan JW, Bücheler J. Vertebral scale system to measure canine heart size in radiographs. *J Am Vet Med Assoc*. 1995;206: 194-199.
48. Jepsen-Grant K, Pollard RE, Johnson LR. Vertebral heart scores in eight dog breeds. *Vet Radiol Ultrasound*. 2013;54: 3-8. 10.1111/j.1740-8261.2012.01976.x
49. Baisan RA, Vulpe V. Vertebral heart size and vertebral left atrial size reference ranges in healthy Maltese dogs. *Vet Radiol Ultrasound*. 2021. 10.1111/vru.13027
50. Bavegems V, Van Caelenberg A, Duchateau L, Sys SU, Van Bree H, De Rick A. Vertebral heart size ranges specific for whippets. *Vet Radiol Ultrasound*. 2005;46: 400-403. 10.1111/j.1740-8261.2005.00073.x
51. Lamb CR, Wikeley H, Boswood A, Pfeiffer DU. Use of breed-specific ranges for the vertebral heart scale as an aid to the radiographic diagnosis of cardiac disease in dogs. *Vet Rec*. 2001;148: 707-711. 10.1136/vr.148.23.707

52. Puccinelli C, Citi S, Vezzosi T, Garibaldi S, Tognetti R. A radiographic study of breed-specific vertebral heart score and vertebral left atrial size in Chihuahuas. *Vet Radiol Ultrasound*. 2021;62: 20-26.  
10.1111/vru.12919
53. Luciani MG, Withoef JA, Mondardo Cardoso Pissetti H, Pasini de Souza L, Silvestre Sombrio M, Bach EC, et al. Vertebral heart size in healthy Australian cattle dog. *Anat Histol Embryol*. 2019;48: 264-267.  
10.1111/ahe.12434
54. Birks R, Fine DM, Leach SB, Clay SE, Eason BD, Britt LG, et al. Breed-Specific Vertebral Heart Scale for the Dachshund. *J Am Anim Hosp Assoc*. 2017;53: 73-79. 10.5326/jaaha-ms-6474
55. Marin LM, Brown J, McBrien C, Baumwart R, Samii VF, Couto CG. Vertebral heart size in retired racing Greyhounds. *Vet Radiol Ultrasound*. 2007;48: 332-334. 10.1111/j.1740-8261.2007.00252.x
56. Kraetschmer S, Ludwig K, Meneses F, Nolte I, Simon D. Vertebral heart scale in the beagle dog. *J Small Anim Pract*. 2008;49: 240-243.  
10.1111/j.1748-5827.2007.00531.x
57. Taylor CJ, Simon BT, Stanley BJ, Lai GP, Thieman Mankin KM. Norwich terriers possess a greater vertebral heart scale than the canine reference value. *Vet Radiol Ultrasound*. 2020;61: 10-15.  
10.1111/vru.12813

58. Bodh D, Hoque M, Saxena AC, Gugjoo MB, Bist D, Chaudhary JK. Vertebral scale system to measure heart size in thoracic radiographs of Indian Spitz, Labrador retriever and Mongrel dogs. *Vet World*. 2016;9: 371-376. 10.14202/vetworld.2016.371-376
59. Kallassy A, Calendrier E, Bouhsina N, Fusellier M. Vertebral Heart Scale for the Brittany Spaniel: Breed-Specific Range and Its Correlation with Heart Disease Assessed by Clinical and Echocardiographic Findings. *Vet Sci*. 2021;8. 10.3390/vetsci8120300
60. Bagardi M, Locatelli C, Manfredi M, Bassi J, Spediacci C, Ghilardi S, et al. Breed-specific vertebral heart score, vertebral left atrial size, and radiographic left atrial dimension in Cavalier King Charles Spaniels: Reference interval study. *Vet Radiol Ultrasound*. 2022;63: 156-163. 10.1111/vru.13036
61. Greco A, Meomartino L, Raiano V, Fatone G, Brunetti A. Effect of left vs. right recumbency on the vertebral heart score in normal dogs. *Veterinary Radiology & Ultrasound*. 2008;49: 454-455. <https://doi.org/10.1111/j.1740-8261.2008.00406.x>
62. Ryan R, Gutierrez-Quintana R, Ter Haar G, De Decker S. Prevalence of thoracic vertebral malformations in French bulldogs, Pugs and English bulldogs with and without associated neurological deficits. *Vet J*. 2017;221: 25-29. 10.1016/j.tvjl.2017.01.018

63. LEE R, LEOWIJUK C. Normal parameters in abdominal radiology of the dog and cat. *Journal of Small Animal Practice*. 1982;23: 251-269.  
<https://doi.org/10.1111/j.1748-5827.1982.tb01664.x>
64. Finco DR, Stiles NS, Kneller SK, Lewis RE, Barrett RB. Radiologic estimation of kidney size of the dog. *J Am Vet Med Assoc*. 1971;159: 995-1002.
65. Barr FJ, Holt PE, Gibbs C. Ultrasonographic measurement of normal renal parameters. *Journal of Small Animal Practice*. 1990;31: 180-184. <https://doi.org/10.1111/j.1748-5827.1990.tb00764.x>
66. Nyland TG, Kantrowitz BM, Fisher P, Olander HJ, Hornof WJ. ULTRASONIC DETERMINATION OF KIDNEY VOLUME IN THE DOG. *Veterinary Radiology*. 1989;30: 174-180.  
<https://doi.org/10.1111/j.1740-8261.1989.tb00771.x>
67. Nyland TG, Fisher PE, Gregory CR, Wisner ER. Ultrasonographic evaluation of renal size in dogs with acute allograft rejection. *Vet Radiol Ultrasound*. 1997;38: 55-61. [10.1111/j.1740-8261.1997.tb01604.x](https://doi.org/10.1111/j.1740-8261.1997.tb01604.x)
68. Felkai CS, Vörös K, Vrabély T, Karsai F. ULTRASONOGRAPHIC DETERMINATION OF RENAL VOLUME IN THE DOG. *Veterinary Radiology & Ultrasound*. 1992;33: 292-296.  
<https://doi.org/10.1111/j.1740-8261.1992.tb00146.x>

69. Barella G, Lodi M, Sabbadin LA, Faverzani S. A new method for ultrasonographic measurement of kidney size in healthy dogs. *J Ultrasound*. 2012;15: 186-191. 10.1016/j.jus.2012.06.004
70. Mareschal A, d'Anjou MA, Moreau M, Alexander K, Beauregard G. Ultrasonographic measurement of kidney-to-aorta ratio as a method of estimating renal size in dogs. *Vet Radiol Ultrasound*. 2007;48: 434-438. 10.1111/j.1740-8261.2007.00274.x
71. Widmer WR, Mattoon JS, Vaden SL. 16 - Urinary tract. In: Mattoon JS, Sellon RK, Berry CR (eds): *Small Animal Diagnostic Ultrasound (Fourth Edition)*. St. Louis (MO): W.B. Saunders, 2021;583-634.
72. Seiler GS. Chapter 41 - Kidneys and Ureters. In: Thrall DE (ed): *Textbook of Veterinary Diagnostic Radiology (Seventh Edition)*: W.B. Saunders, 2018;823-845.
73. Agut A, Soler M, Laredo FG, Pallares FJ, Seva JI. Imaging diagnosis--Ultrasound-guided ethanol sclerotherapy for a simple renal cyst. *Vet Radiol Ultrasound*. 2008;49: 65-67. 10.1111/j.1740-8261.2007.00319.x
74. Ohlerth S, O'Brien RT. Contrast ultrasound: general principles and veterinary clinical applications. *Vet J*. 2007;174: 501-512. 10.1016/j.tvjl.2007.02.009

75. Sohn J, Yun S, Lee J, Chang D, Choi M, Yoon J. Reestablishment of radiographic kidney size in Miniature Schnauzer dogs. *J Vet Med Sci.* 2017;78: 1805-1810. 10.1292/jvms.16-0003
76. Seiler GS, Cohen EB, d'Anjou M-A, French J, Gaschen L, Knapp S, et al. ACVR and ECVDI consensus statement for the standardization of the abdominal ultrasound examination. *Veterinary Radiology & Ultrasound.* 2022;63: 661-674. <https://doi.org/10.1111/vru.13151>
77. Lobacz MA, Sullivan M, Mellor D, Hammond G, Labruyère J, Dennis R. Effect of breed, age, weight and gender on radiographic renal size in the dog. *Vet Radiol Ultrasound.* 2012;53: 437-441. 10.1111/j.1740-8261.2012.01937.x

## Chapter II

Radiographical age determination in puppies using the dimension of the ossification centers: preliminary results with the distal radius.

Dario Costanza, Erica Castiello, Pierpaolo Coluccia, Orlando Paciello, Gianluca Miletta, Adelaide Greco & Leonardo Meomartino.

Portions of this study were presented as an oral communication at the 73rd SISVET Congress, Olbia (Italy), 18 – 22 June 2018.

## 2.1 ABSTRACT

The illegal trafficking of puppies has led to a need for a more precise method of determining their age, since the movement of puppies across the European Union is only allowed after they reach 15 weeks of age. Currently, the assessment of dental eruption and the radiographic secondary ossification centers (OCs) are the most used methods, but both have wide temporal windows, making them unreliable in procedural debates. This study aimed to evaluate the relevance of the distal radius OC (DROC) in estimating puppies' age. The study design involved two distinct components, one utilizing a sample of live subjects (“*in vivo*” group) and the other utilizing a sample of cadaver specimens (“*ex vivo*” group) whose age was known. The *in vivo* group was composed of puppies of different breeds, who were radiographically examined starting from the day 7<sup>th</sup> up to 4 months of age, with a mean interval of 11 days between each examination. In the *ex vivo* group, a single radiographic examination was performed. The same radiographic protocol, including mediolateral and craniocaudal projections of the right forelimb and mediolateral projection of the right hindlimb, was used for both groups. The age of appearance, the linear dimensions (width and height) and the area of the DROC were recorded. The data were analyzed using descriptive statistics, the Mann-Whitney *U*-test, and Spearman's rank correlation. The DROC was visible in all 68 puppies at 27 days, and its growth was gradual. The statistical analysis revealed a strong correlation between the DROC area and age ( $P < 0.0001$ ,  $R^2=0.99$ ), while there were no significant differences between sexes ( $P = 0.49$ ). Equations to calculate age were derived from the correlations, with an accuracy value of  $\pm 5$  days in 80% of the sample. These results demonstrate that the DROC

dimensions can aid in obtaining a more accurate evaluation of puppies' age and provide support in a forensic scenario.

## 2.2 INTRODUCTION

The illegal trafficking of puppies is a growing issue in forensic Veterinary Medicine. Fifteen weeks is the legal age at which puppies can be moved abroad within and across the European Union (EU) states (EU Reg. No. 576/20139) but puppies of illegal trafficking are usually younger than 15 weeks. These puppies are mostly irregularly imported from eastern European countries and are often accompanied by certificates attesting to a fake age.<sup>1,2</sup> In puppies, the more accredited methods for determining age are dental examination and secondary ossification centers (OCs) radiographic evaluation.<sup>3</sup> Unfortunately, both methods have a wide range of errors, estimated in  $\pm 15$  days, and are potentially unreliable in a legal court.<sup>4, 5</sup> Additionally, studies on these methods have only been conducted on specific breeds, making their results unreliable to all dogs.<sup>2, 3, 6</sup> The canine species exhibits a wide range of morphological variation due to the extensive human selection process, which has led to the development of breeds of varying sizes that exhibit different skeletal growth patterns.<sup>7</sup> In small or medium-sized dogs, skeletal maturity is reached before the age of one year, while for large/giant breeds dogs, skeletal growth can last up to sixteen months. This difference inevitably affects the timing of appearance, growth rate, and age of the closure of the epiphyseal growth plates.<sup>8</sup> Additionally, even puppies of the same breed can exhibit variations in skeletal growth related to variables such as nutrition, congenital pathologies, or acquired diseases.<sup>9</sup> The most of the literature on OCs dates back to the early 1900s. These studies were conducted on small samples of specific dog breeds, and the investigation protocols often were not provided.<sup>10-21</sup> Despite this, these studies are still referenced in veterinary radiology textbooks.<sup>3, 8, 22-25</sup> More

recently, due to the increased illegal trafficking of dog puppies and public awareness, a renewed interest has invested the OCs' radiographic evaluation, their time of appearance, growth rate and reliability as a method of age estimation.<sup>6, 26</sup> However, the usefulness of radiographic assessment of OCs in a forensic scenario remains questionable. Specifically, studies in the literature consider only the time of appearance of OCs but none of them consider the OCs growth rate and how this differs between small-breed puppies and large or giant-sized ones. Notably, small-breed puppies represent the large portion of illegally trafficked dogs. This study aimed to develop a radiographic method for determining the age of puppies that considers not only the timing of the appearance of OCs but also their growth rate. In this preliminary section of the study, our investigation focused on the distal radius OC (DROC).

### 2.3 MATERIALS AND METHODS

The prospective, reference interval, longitudinal study was approved by the Ethical Animal Care and use committee of the University of Naples "Federico II" (protocol number PG/2018/0050378).

The study design involved two distinct components, one utilizing a sample of live dogs ("*in vivo*" group) and the other utilizing a sample of cadavers ("*ex vivo*" group). The *in vivo* component was longitudinal in design and was performed on a cohort of puppies of three different sizes, including one giant breed (Bullmastiff), one large breed (Golden Retriever), and one small breed (Cavalier King Charles spaniel). All the dogs of each breed come from the same litter and the same breeder. Each dog was radiographically examined on a bi-weekly basis, starting from the day 7<sup>th</sup> to 4 months (120

days), considering the breeder's availability. Before each radiographic examination, each puppy underwent a clinical assessment to ensure its overall health. Criteria for exclusion from the study included suboptimal health status, the presence of clinically and/or radiographically evident skeletal diseases, and a diet that differed from that of other puppies in the same litter. The radiographic examinations were performed using a portable device (Orange 1040HF, EcoRay, Seoul, South Korea) coupled with a digital radiography system. The film-focus distance was fixed at 100 cm. All the radiographical examinations were performed without sedation with puppies manually restrained by a single operator. During the execution of the radiographic exams, all necessary radiation exposure protections were strictly adopted, including personal protective equipment such as lead aprons, thyroid shields, and lead glasses. Furthermore, exposure parameters (kVp and mAs) were minimized as low as reasonably achievable, and narrow collimation was adopted to minimize scattered radiation. After each radiograph acquisition, if the obtained images were deemed inadequate due to motion artifacts or excessive limb rotation, only one additional attempt was made in order to minimize the puppy's and operator's exposure to radiations. Furthermore, all the operators involved in these activities were equipped with radiation badges and included in a radiation protection program. The *ex vivo* component of the study consisted of puppies whose age was known and whose death occurred from causes unrelated to this study. In these puppies, a single radiographic examination was performed using a direct digital (DR) radiographic system (Agfa-Gevaert DR 14e Agfa HealthCare, Mortsels, Belgium). For both *in vivo* and *ex vivo* groups, the radiographic protocol included the acquisition of

mediolateral (ML) and craniocaudal (CrCa) views of the right forelimb and a ML view of the right hindlimb. All the radiographic images in DICOM format were stored in the picture archiving and communication system (dcm4chee-arc-light version 5.11.1, <http://www.dcm4chee.org>) of the Interdepartmental Centre of Veterinary Radiology<sup>27</sup> and reviewed on a workstation (iMac 5K, 27-inch, Apple Inc., Cupertino CA, USA) using an open-source DICOM viewer (Horos version 3.3.6, 64-bit, Nimble Co LLC d/b/a Purview, Annapolis, MD, USA, <https://www.horosproject.org>). Images deemed inadequate due to motion artifacts or poorly projected were excluded from the analysis. Of all visible secondary ossification centers, the distal radius ossification center (DROC) in the CrCa projection was considered at this stage. The DROC width (in mm) and height (in mm) were measured by a professor of veterinary radiology with a Ph.D. and >25 years of experience, using the 'line' function. The DROC area (in mm<sup>2</sup>) was obtained using the formula for calculating the area of a rectangle (length \* width) (Figure 2.1). All data were reported in an electronic spreadsheet (Microsoft Excel version 16.52 2021, Microsoft Corp). Statistical analyses were performed by one of the authors (L.M.) using commercial statistics software (Prism version 9.5.0 (525), GraphPad Software San Diego, California). Given the heterogeneity of the sample, the data were analyzed using non-parametric models. The Mann-Whitney's U test and Spearman's rank correlation coefficient ( $r_s$ ) were used to investigate possible differences between sexes and the correlation with age, respectively. The correlation was made considering the entire sample and the subcategories represented by dog size and sex. The best equations for predicting age based on DROC

were derived from these correlations. In all analyses,  $P < .05$  was considered statistically significant.



*FIGURE 2.1* Close up view of the DROC in a Cavalier King Charles Spaniel (A), Golden Retriever (B) and Bullmastiff (C). The DROC area is obtained by multiplying the DROC width (red lines) by the height (white lines)

**2.4 RESULTS**

The final sample consisted of 291 radiographic studies performed on 68 puppies, starting from 7 days to 142 days of age (20 weeks). Twenty-five out of sixty-eight of the puppies examined came from the *in vivo* component and were divided as follows: 9 Bull mastiffs (5 females, 4 males), 10 Golden Retrievers (7 females, 3 males), and 6 Cavalier King Charles Spaniels (4 females, 2 males). The remaining 43 puppies came from the *ex vivo* component. The OCs visible during the analyzed period using the proposed radiographic protocol are summarised in Table 1.

<b>Forelimb</b>
Radius distal epiphysis
Ulna distal epiphysis
Radial carpal bone
Central carpal bone
Intermediate carpal bone
Accessory carpal bone
Carpal bone I - IV
Metacarpal bone I proximal epiphysis
Metacarpal bone II - V distal epiphysis
Proximal phalanx (digit I - V) proximal epiphysis
Middle phalanx (digit II - V) proximal epiphysis
Palmar sesamoid bones
Dorsal sesamoid bones
<b>Hindlimb</b>
Femur distal epiphysis (trochlea and condyles)
Patella
Tibial tuberosity
Tibial proximal epiphysis
Tibial distal epiphysis
Fibula proximal epiphysis
Fibula distal epiphysis
Calcaneal tuber
Central tarsal bone
Tarsal bone I - IV

*TABLE 2.1 Secondary ossification centers (OCs) visible in the considered period (7th – 120th day) that can be evaluated with the adopted radiographic protocol.*

The DROC was visible from day 22, with a steady increase in size over the days. The statistical analysis showed a strong correlation between age, linear dimensions (width and height), and area. Notably, the DROC had different growth in medium/large-sized and small-sized dogs (Figure 2.2).

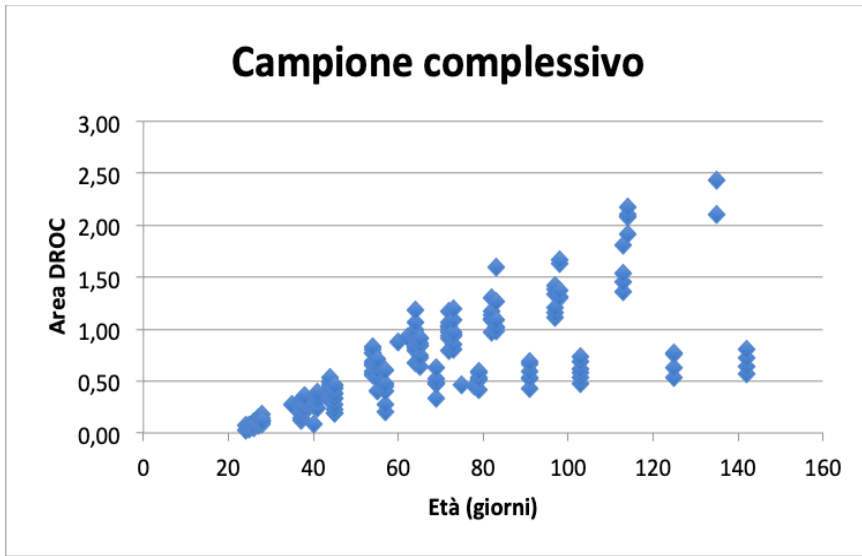


*FIGURE 2.2 Correlation between DROC area (in mm<sup>2</sup>) and age (in days) in all the dogs included in the final sample. From day 60th there are two different growth trends.*

Furthermore, considering these two categories independently, medium/large-sized dogs exhibit a linear correlation between age (in days) and DROC ( $R^2 = 0.93$ ,  $P < 0.0001$ ) (Figure 2.3), while small-sized dogs had a logarithmic correlation ( $R^2 = 0.97$ ,  $P < 0.0001$ ) (Figure 2.4).

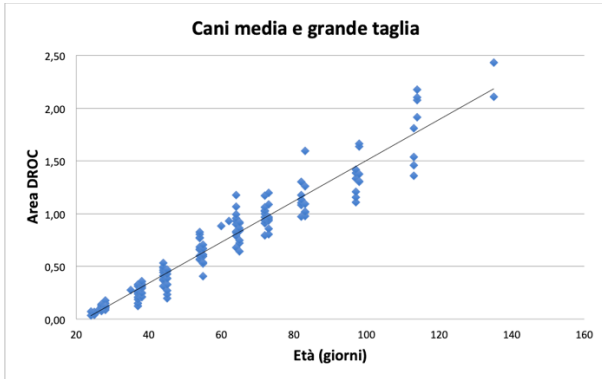


FIGURE 2.3 Linear correlation between DROC area (mm<sup>2</sup>) and age (in days) for medium/large-sized dogs.

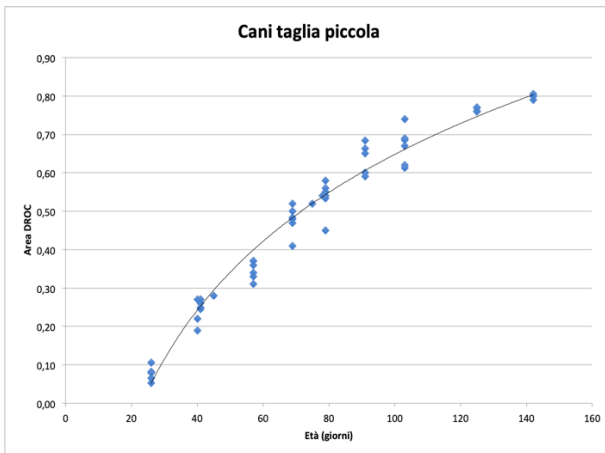


FIGURE 2.4 Logarithmic correlation between DROC area (mm<sup>2</sup>) and age (in days) for medium/large-sized dogs..

No differences were found between the sexes ( $P = 0.49$ ). Based on our model, the age (in days) can be estimated using the following formulae that had a variability of  $\pm 5$  days on 80% of the sample:

Age (in days) =  $\text{DROC (mm}^2\text{)}/1,983 + 43,36$  for medium/large-sized dogs

Age (in days) =  $\text{DROC (mm}^2\text{)}/\log 0,4428 + 1,3914$

## 2.5 DISCUSSION

This study aimed to describe a radiographic method for determining the age of puppies that considers the date of appearance and growth rate of OCs.

The illegal trafficking of puppies has become a prevalent concern in Europe in recent years. These animals are sold without proper documentation, vaccinations and are often plagued by severe health issues.<sup>1, 2</sup> The puppy trade has become a highly profitable business for criminals who are taking advantage of the growing demand for popular breeds of dogs and cats. The proceeds from illegal trafficking are often funnelled back into organized crime, further exacerbating the problem.<sup>1</sup> The minimum age for animal movement within the European Union countries is set at 15 weeks, because at 12<sup>th</sup> week of age it is administered the mandatory vaccination against the rabies and 3 weeks is the necessary period for developing anti-rabies immunity (EU Reg. No. 576/20139). To ensure compliance, judicial authorities have placed increasing demands on veterinarians to determine the age of animals, particularly dogs, being moved within and outside the EU. Traditionally, in veterinary medicine, age estimation has relied on the assessment of dentition. However, the reliability of this technique is limited to animals around 6-7 months of age, and external factors such as poor diet,

infectious diseases and antibiotic treatments, can result in missing, decayed, or damaged teeth, making dentition an unreliable method for age determination in legal debates.<sup>3,4</sup> In human forensic medicine, the preferred method for determining age is through the examination of OCs development and closure rates. This technique is considered effective for individuals ranging in age from birth to approximately 24-26 years. According to the authors, the protocol adopted constitutes a reasonable compromise by limiting X-ray exposure while allowing to visualise numerous OCs. In this preliminary part, our investigation focused on the DROC as this is readily visible since the third week of life, has a regular, roughly rectangular shape and is thus relatively easy to measure. The puppies of the *in vivo* component became progressively accustomed to manipulation over the weeks. Furthermore, the progressive body growth made their handling easier, thus making the need for repeat X-rays less frequent. The DROC was visible in all subjects from day 22. The profiles became more defined as the weeks passed, making measurement easier. Statistical analysis revealed that the DROC had different growth patterns among the different body size dog's breeds included in the sample. In detail, till the fourth month of life, the DROC area in medium and large dogs showed a geometrical growth pattern while, in small-sized dogs, a logarithmic growth pattern characterized by an initial rapid growth pattern, followed by a quite levelled one. This variation in the DROC growth pattern is probably linked to these breeds' different skeletal growth rates. Medium, large and giant-sized dogs must reach a significant size in a few months. Differently, small-sized dogs, after a few weeks, reach body dimensions similar to those they will have as adults. In both groups considered, the correlation between the area of the DROC

and the age showed a high correlation that allowed the calculation of the above-reported formulae. As there are no significant differences between the sexes at this age, these formulae are applicable regardless of sex. Even though this was a preliminary study and with a limited number of dogs, especially for the *in vivo* component, differences in OCs growth rate pattern were already evident. The different growth pattern found in the current study is greater than that already reported in the literature between large breed dogs of different breeds.<sup>4</sup> Although this difference have to be confirmed also for other OCs, this can be one of the reasons for the wide range of OCs appearance and physéal closure reported in the literature, since most of this studies were performed on small samples made by large breed dogs or mixed breed.<sup>10-21</sup> Consequently, in order to determine the age of the puppies with a reasonable narrow margin of error not only the time of appearance and physéal closure of OCs must be taken into account but also their progressive growth, together with other variables, such as breeds and body sizes, . Limitations of our study include the small number of subjects from the *in vivo* component, which limited the number of longitudinal radiographic evaluations. Furthermore, since all the dogs of the *in vivo* component came from the same breeder, the influence of variables such as diet was not evaluated. In conclusion, morphometric indices such as DROC's area could be a reliable method in establishing the age of puppies during their first weeks with a reasonable precision. Further studies are needed to reduce the margin of error by combining the information obtained from the analysis of multiple OCs visible through the proposed protocol.

## 2.6 REFERENCES

1. Maher J, Wyatt T. European illegal puppy trade and organised crime. *Trends Organ Crime*. 2021;**24**: 506-525. 10.1007/s12117-021-09429-8
2. Modina SC, Andreis ME, Moioli M, Di Giancamillo M. Age assessment in puppies: Coming to terms with forensic requests. *Forensic Science International*. 2019;**297**: 8-15.  
<https://doi.org/10.1016/j.forsciint.2019.01.003>
3. Sutton LK, Byrd JH, Brooks JW. Age Determination in Dogs and Cats. In: Brooks JW (ed): *Veterinary Forensic Pathology, Volume 2*. Cham: Springer International Publishing, 2018;151-163.
4. Roccaro M, Peli A. Age determination in dog puppies by teeth examination: legal, health and welfare implications, review of the literature and practical considerations. *Veterinaria Italiana*. 2020;**56**: 149-162.
5. Loráskó G, Rác B, Ózsvári L. Changes in the Dentition of Small Dogs up to 4 Months of Age. *Animals*. 2022;**12**: 1417.
6. Roccaro M, Diana A, Linta N, Rinnovati R, Freo M, Peli A. Limb development in skeletally-immature large-sized dogs: A radiographic study. *PLoS One*. 2021;**16**: e0254788. 10.1371/journal.pone.0254788

7. Howard E. Evans AdL. The Dog and Its Relatives. In: Howard E. Evans AdL (ed): *Miller's Anatomy of the dog*. 3251 Riverport Lane St. Louis, Missouri 63043: Elsevier Saunders, 2013;1 - 12.
8. Nerissa Stander NC. Long bones – juvenile. In: Robert M. Kirberger FJM (ed): *BSAVA Manual of Canine and Feline Musculoskeletal Imaging*. Woodrow House, 1 Telford Way, Waterwells Business Park, Quedgeley, Gloucester GL2 2AB: British Small Animal Veterinary Association, 2016;87 - 107.
9. Von Pfeil D, DeCamp C, Abood SK. The Epiphyseal Plate: Nutritional and Hormonal Influences; Hereditary and Other Disorders. *Compendium Continuing Education for Veterinarians*. 2009;**31**.
10. Seoudi K. X-ray examination of epiphyseal union as an aid to the estimation of the age in dogs. *Br Vet J*. 1947;**103**: 150-155.
11. Hare WC. Radiographic anatomy of the canine pectoral limb. II. Developing limb. *J Am Vet Med Assoc*. 1959;**135**: 305-310.
12. Hare WC. Radiographic anatomy of the canine pelvic limb. Part II. Developing limb. *J Am Vet Med Assoc*. 1960;**136**: 603-611.
13. SMITH RN. Radiological Observations on the Limbs of Young Greyhounds. *Journal of Small Animal Practice*. 1960;**1**: 84-90.  
<https://doi.org/10.1111/j.1748-5827.1960.tb06056.x>

14. Smith R, Allcock J. Epiphysial fusion in the greyhound. *Veterinary Record*. 1960;**72**: 75-79.
15. Hare WC. The ages at which the centers of ossification appear roentgenographically in the limb bones of the dog. *Am J Vet Res*. 1961;**22**: 825-835.
16. Chapman WL, Jr. Appearance of ossification centers and epiphysial closures as determined by radiographic techniques. *J Am Vet Med Assoc*. 1965;**147**: 138-141.
17. Sumner-Smith G. Observations on epiphysal fusion of the canine appendicular skeleton. *J Small Anim Pract*. 1966;**7**: 303-311.  
10.1111/j.1748-5827.1966.tb04447.x
18. Van Sickle D. The relationship of ossification to canine elbow dysplasia. *J Am Anim Hosp Assoc*. 1966;**2**: 24-31.
19. Gustafsson P-O, Kasström H, Olsson S-E, Wennman B. Skeletal Development and Sexual Maturation in German Shepherds, Greyhounds and Their Crossbreed Offspring: An Investigation with Special Reference to Hip Dysplasia. *Acta Radiologica Diagnosis*. 1972;**13**: 187-190.  
10.1177/0284185172013s31936

20. Riser WH. Growth and Development of the Normal Canine Pelvis, Hip Joints and Femurs from Birth to Maturity: A Radiographic Study1. *Veterinary Radiology*. 1973;**14**: 24-34. <https://doi.org/10.1111/j.1740-8261.1973.tb00654.x>
21. Yonamine H, Ogi N, Ishikawa T, Ichiki H. Radiographic studies on skeletal growth of the pectoral limb of the beagle. *Nihon Juigaku Zasshi*. 1980;**42**: 417-425. 10.1292/jvms1939.42.417
22. Schebitz H, Wilkens H. Toracic limb; Pelvic limb. *Atlas of radiographic anatomy of the dog and cat 5th ed Berlin: Paul Parey*. 1989: 56-104.
23. Dennis R, Kirberger R, Barr F, Wrigley R. Chapter 3: Appendicular skeleton. *Handbook of small animal radiology and ultrasound 2nd ed Edinburgh: Churchill Livingstone Elsevier*. 2010: 51-80.
24. Kealy J, McAllister H. Chapter 4: Bones and joints. *Diagnostic radiology and ultrasonography of the dog and cat 5th ed St Louis: Elsevier Saunders*. 2011: 351-361.
25. Thrall DE, Robertson ID. Chapter 1 - Basic Imaging Principles and Physeal Closure Time. In: Thrall DE, Robertson ID (eds): *Atlas of Normal Radiographic Anatomy and Anatomic Variants in the Dog and Cat (Second Edition)*: W.B. Saunders, 2016;1-19.

26. Modena SC, Veronesi MC, Moioli M, Meloni T, Lodi G, Bronzo V, et al. Small-sized newborn dogs skeletal development: radiologic, morphometric, and histological findings obtained from spontaneously dead animals. *BMC Veterinary Research*. 2017;**13**: 175. 10.1186/s12917-017-1092-6
27. Costanza D, Coluccia P, Castiello E, Greco A, Meomartino L. Description of a low-cost picture archiving and communication system based on network-attached storage. *Veterinary Radiology & Ultrasound*. 2022;**63**: 249-253. <https://doi.org/10.1111/vru.13061>

## Chapter III

### A computed tomography-based method for the assessment of canine retrobulbar cone volume for ophthalmic anaesthesia

Adelaide Greco, Dario Costanza, Andrea Senatore, Dario Bruzzese, Fabiana Micieli, Ludovica Chiavaccini, Mauro Di Giancamillo, Giovanni Della Valle, Giancarlo Vesce, Arturo Brunetti, Leonardo Meomartino.

Veterinary Anaesthesia and Analgesia 2021, **48**, 759 - 766  
<https://doi.org/10.1016/j.vaa.2021.03.015>

### 3.1 ABSTRACT

Objective of this retrospective cohort imaging study was to develop a comprehensive formula for calculating the volume of local anaesthetic solution used for retrobulbar anaesthesia in dogs with different skull morphologies. Skull computed tomography (CT) images of 188 dogs of different breeds collected between January 2009 and December 2017. Anatomical integrity of the orbit and adjacent structures, presenting complaint, clinical signs and CT findings were verified to exclude ocular abnormalities. The volume of the retrobulbar cone of 376 eyes was calculated using CT scans of the dogs' skulls. Additional data recorded included morphology of the skull, body weight, sex and size of the dogs, all of which were matched for possible association to the retrobulbar cone volume through univariable and multivariable linear regression models. Results of linear regression models were expressed as estimated beta coefficients with the corresponding 95% confidence intervals (95% CIs). Using univariate analysis, the retrobulbar cone volume was positively associated with weight and male sex. In addition, brachycephalic and dolichocephalic dogs showed a larger retrobulbar cone volume than mesocephalic dogs, while sex was no longer significantly associated with the retrobulbar cone volume. In multivariate analysis, when considering all variables in the model, weight emerged as the strongest predictor (beta coefficient:  $0.062 \text{ mL kg}^{-1}$ , 95% CI:  $0.056 - 0.067 \text{ mL kg}^{-1}$ ,  $P < 0.001$ ). In the veterinary literature, there is no agreement on the precise volume of local anaesthetic solution that should be used to achieve intraconal retrobulbar anaesthesia in dogs. Here we suggest a formula to calculate the

retrobulbar cone volume and, accordingly, the injection volume of local anaesthetic solution for effective retrobulbar anaesthesia.

### 3.2 INTRODUCTION

Among multimodal analgesia techniques, the analgesic efficacy of regional anaesthesia is unrivalled.<sup>1, 2</sup> Locoregional anaesthesia of the eye anaesthetizes the sensory, motor and autonomic innervation of the globe and its adnexa, sparing general anaesthesia requirement, decreasing the need for systemic analgesia and avoiding the use of neuromuscular blocking agents.<sup>3-</sup>

<sup>5</sup> One of the most well-documented regional anaesthesia techniques for ophthalmic surgery is retrobulbar anaesthesia. It consists of the injection of local anaesthetic caudal to the globe in close proximity to the optic foramen and orbital fissure. The optic (II), oculomotor (III), trochlear (IV), abducens (VI), and ophthalmic and maxillary branches of the trigeminal (V) cranial nerves emerge from this fissure. These nerves are in close proximity to the rostral alar foramen carrying the zygomatic nerve and to the ethmoidal foramen allowing passage of the ethmoidal nerve. Retrobulbar anaesthesia allows eye akinesia, exerts effective sparing effects on perioperative anaesthetic and analgesic treatments,<sup>6-8</sup> and inhibits the oculocardiac reflex.<sup>9, 10</sup>

Despite the widespread use of retrobulbar anaesthesia, there is currently no agreement on the volume of anaesthetic required to obtain good clinical efficacy. Nor is there agreement on a formula to easily calculate that volume for daily use. Shilo-Benjamini<sup>11</sup> reviewed different retrobulbar anaesthetic techniques in dogs, remarking that most of the authors reported a different volume of local anaesthetic solution for injection. This was mostly calculated empirically and based solely on the dog's body weight. However, studies compared by Shilo-Benjamini<sup>11</sup> lacked homogeneous morphometry of the subjects. Dogs are the most morphologically variable land mammals on earth.<sup>12</sup> Within the considerable

variation in their size and morphology, the cranial index has been used to categorize approximately 400 dog breeds into three broad classes: dolichocephalic, mesocephalic and brachycephalic.<sup>13</sup> Within these categories, there exists a wide variation in the ocular anatomy, which means that the practitioners must consider several variables when they perform retrobulbar anaesthesia. One of these variables is the volume of local anaesthetic solution for injection. Underestimating this volume can result in an ineffective block. An overestimation of this volume can cause severe undesirable effects including toxicity, proptosis and increased intraocular pressure.<sup>14</sup> Since mixed breed dogs represent a large part of the canine population, cranial index categorization has been hindered by an absence of clearly defined craniofacial margins.<sup>13, 15</sup> As a consequence, dogs with similar body weight but with a differing skull morphology might display different retrobulbar cone volumes and shapes. Therefore, the volume of anaesthetic solution required for retrobulbar anaesthesia should be calculated accordingly. Klaumann et al.<sup>16</sup> were the first authors to consider a dog's skull morphology, as distinct from their body weight, to calculate the required injection volume. However, a limited number of subjects were enrolled in that study. To the authors' knowledge, there are currently no studies assessing the differences in the retrobulbar cone volume between dolichocephalic, mesocephalic, and brachycephalic dogs via computed tomography (CT) examination. The objective of our study was to develop a comprehensive formula for calculating the volume of the retrobulbar cone in dogs with different skull morphologies. For this purpose, our retrospective study evaluated the retrobulbar cone volume variations between dolichocephalic, mesocephalic and brachycephalic dogs in a large

population. Using morphometric data of canine skulls acquired by CT, we describe a comprehensive formula for estimating the actual volume to be injected (VTBI) for retrobulbar anaesthesia in dogs. We hypothesized that not only bodyweight but also skull morphology would affect the retrobulbar cone volume in dogs of different breeds.

### 3.3 MATERIALS AND METHODS

The protocol received full approval by the ethical committee for animal use at the Animal Welfare Committee of the University of Naples Federico II (PG/2020/0043383). All canine head CT studies performed during general anaesthesia for different clinical reasons, between January 2009 and December 2017 at the Interdepartmental Center of Veterinary Radiology, University of Napoli “Federico II”, were retrospectively evaluated. Due to the retrospective nature of the study, anaesthetic protocols were not standardized. Inclusion criteria were complete visualization of the globes. Exclusion criteria included the presence of ocular, retrobulbar and/or orbital diseases. All CT studies were performed using a slice thickness of 1.5 - 2.5 mm and were then post-processed using ‘standard’ and ‘bone’ convolution filters. Images were evaluated through a soft tissue window (window width = 350 HU and window level = 40 HU) using a DICOM viewer software (Horos Version 3.0.1; 64-bit, Nimble Co LLC d/b/a Purview, Annapolis, MD, USA, <https://www.horosproject.org>). For measurement of the retrobulbar cone volume, all CT examinations were processed through a multiplanar reformation technique along the axial, sagittal and dorsal planes. The lateral and medial ocular rectus muscles and the orbital canal were chosen as the anatomical landmarks for retrobulbar cone volume

measurements because they were easily identified. The axial plane was positioned at the level of the eye lenses and oriented until a symmetrical image of both eyes was obtained. The sagittal plane was placed in the centre of the globe and then the dorsal plane was tilted until the optic canal and retrobulbar cone were entirely visible (Figure 3.1).

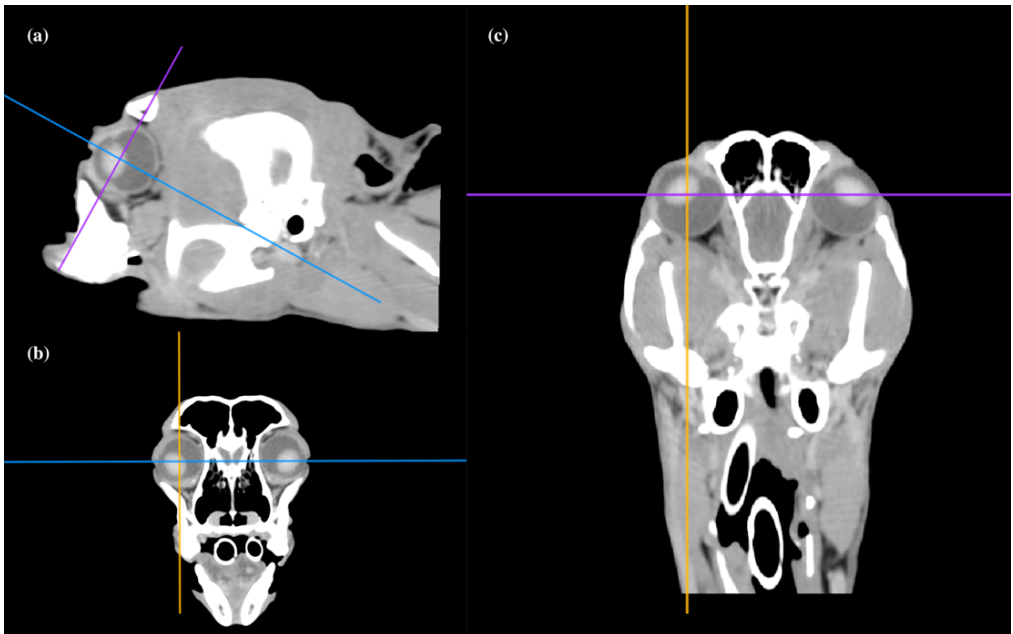


*FIGURE 3.1 Multiplanar reconstruction of a dolichocephalic dog skull; (a) sagittal, (b) axial and (c) dorsal planes are displayed. The yellow line represents the sagittal plane, the violet line the axial plane and the blue line the dorsal plane. Images show the centring of the sagittal and the axial planes on the right globe, and the tilting of the dorsal plane to fully expose the retrobulbar cone and optic foramen.*

After obtaining the images, the cone base diameter and its height were traced. The diameter of the retrobulbar cone base was measured between the insertion points of the lateral and medial rectus muscles on the globe. The height of the cone was then measured as the line running from the centre of the traced cone base diameter to the optic foramen (Figure. 3.2).

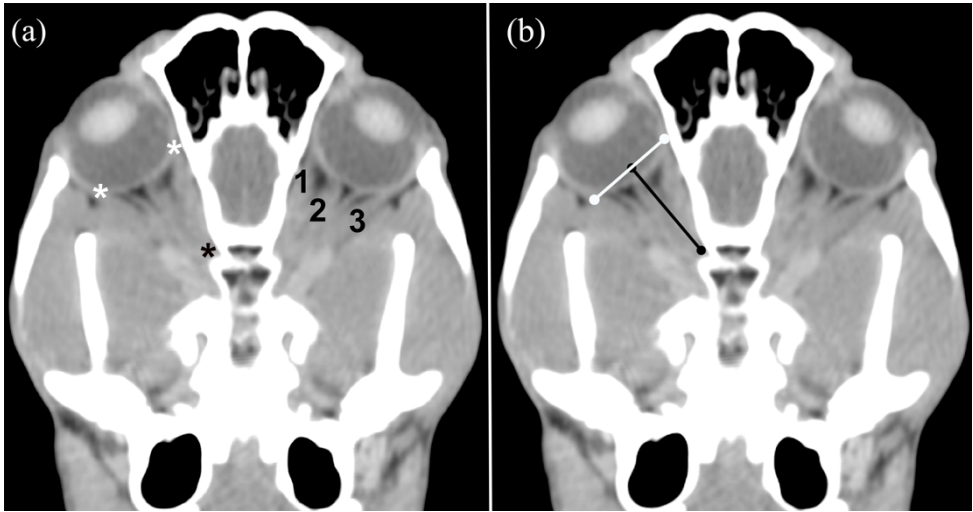


*FIGURE 3.2 A representative example of the retrobulbar cone volume measurements in a dolichocephalic dog skull, made in the dorsal plane. (a) The anatomical landmarks used to trace the cone base diameter and the cone height are displayed: insertion points of medial and lateral rectus muscles (white asterisks); optic canal (black asterisk); 1 = medial rectus muscle; 2 = optic nerve; 3 = lateral rectus muscle. (b) The measurements of retrobulbar cone base diameter (white line) and retrobulbar cone height (black line).*

For each eye, the retrobulbar cone volume (expressed in mL) was calculated according to the formula:  $(\pi * r^2 * h) / 3$  where  $\pi$  was pi,  $r$  was the cone base radius expressed in centimetres (one half of the cone base diameter) and  $h$  was the cone height expressed in centimetres. All CT measurements were made by a radiologist with 10 years experience. In addition, the sex, body weight (expressed in kg), skull morphology and the size of each animal were recorded as possible variables affecting the retrobulbar cone volume. Canine skulls were classified based on the cranial index (skull width \* 100/skull length) as dolichocephalic (cranial index approximately 39), mesocephalic (cranial index approximately 52) and brachycephalic dogs (cranial index approximately 81 or greater).<sup>17</sup> Based on body weight, the size of the dogs was classified as small (< 8 kg), medium (> 8 but 22 kg) and large (> 22 kg). We used the statistical platform R (Version 3.5.1, R Foundation for Statistical Computing, Austria, <https://www.R-project.org/>) for data manipulation, descriptive analysis and linear regression. Standard descriptive statistics were used to describe the characteristics of the sample, and data are reported as mean  $\pm$  standard deviation (SD) or frequencies (percentages). Potential violations from normality were visually checked using boxplots. Univariate comparisons between groups were based on one-way analysis of variance (ANOVA) test, followed by Tukey's honest significant difference *post-hoc* tests. Pearson correlation coefficients were used to assess the collinearity between continuous variables. Multivariate linear regression was used to derive the best equation for predicting retrobulbar cone volume according to the selected predictors. Variable selection was guided by recognition of the importance of the variables in the literature and no automatic procedure was undertaken. All clinically relevant

interactions terms were tested. The prediction sum of squares<sup>18</sup> was used to select the best model. Results of the final model were expressed as estimated beta coefficients with the corresponding 95% confidence intervals (95% CIs). All analyses were conducted at an alpha level of 0.05

### 3.4 RESULTS

The initial sample included 213 skull CT scans. A total of 25 dogs were excluded from the study because they had presented with lesions of the eyes, of the ocular annexes and/or of the retrobulbar space, orbital or periorbital bones. Therefore, the final number of dogs enrolled in the study was 188 and 376 eyes. There were 83 (44.1%) female (32 ovariohysterectomized) and 105 (55.9%) male (11 castrated) dogs. According to the cranial index categorization of the skulls, 22 (11.7%) were brachycephalic, 153 (81.4%) were mesocephalic and 13 (6.9%) were dolichocephalic. Representative 3D volume rendering CT images are reported in Figure 3.3

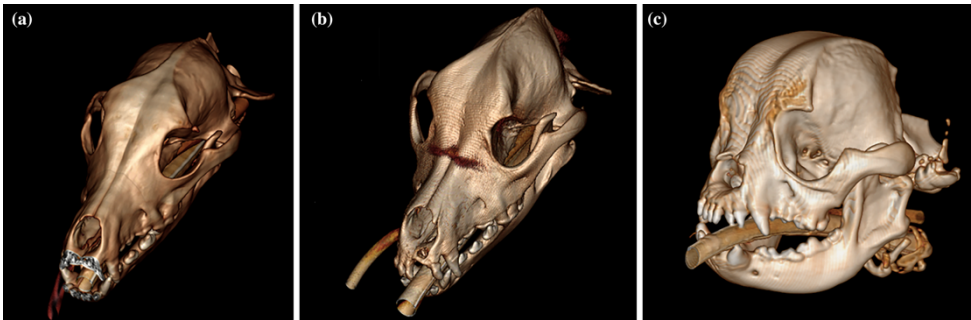


*FIGURE 3.3 Computed tomography 3D volume rendering images of the morphology groups of three dogs' skulls: (a) dolichocephalic, (b) mesocephalic and (c) brachycephalic.*

The mean  $\pm$  SD body weight was  $18.8 \pm 13.4$  kg, and the mean  $\pm$  SD age was  $6.8 \pm 4.0$  years. According to the ANOVA test, the cone volume was significantly larger in the large dogs ( $2.8 \pm 0.77$  mL) than in medium ( $1.88 \pm 0.63$  mL,  $P < 0.001$ ) and small dogs ( $0.94 \pm 0.31$  mL,  $P < 0.001$ ) (Figure 3.4A). Sex also affected the retrobulbar cone volume, being larger in male dogs than in female dogs with the same skull morphology ( $2.19 \pm 1.09$  mL versus  $1.6 \pm 0.84$  mL;  $P < 0.001$ ), while no significant differences were found between castrated male and ovariohysterectomized female dogs. Significant skull morphology-linked retrobulbar cone volume differences were found (Figure 3.4B). Mesocephalic dogs displayed a smaller volume ( $1.82 \pm 0.91$  mL) than brachycephalic ( $2.45 \pm 1.36$  mL,  $P = 0.012$ ) and dolichocephalic dogs ( $2.46 \pm 0.69$  mL,  $P < 0.037$ ). Finally, a positive correlation between retrobulbar cone volume and animal body weight was also found (Pearson  $r = 0.84$ ;  $P < 0.001$ ; Fig. 3.4C). In the multivariate analysis, because there was a strong correlation between size and body weight, only the latter was used. When all the variables were considered, weight persisted as the strongest retrobulbar cone volume predictor, with a significant difference between skull morphologies. When accounting for all the variables in the model, sex was no longer significantly associated with retrobulbar cone volume, thus it was excluded.

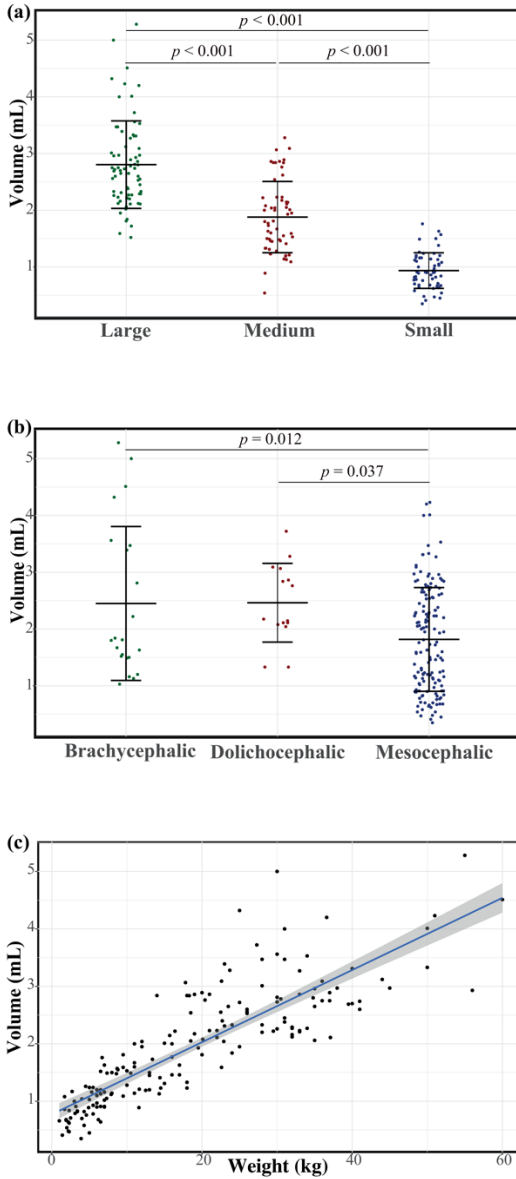


**FIGURE 3.4** Retrobulbar cone volume grouped by size and by skull morphology. **(a)** The distribution of retrobulbar cone volume grouped by skull size (large, medium and small). The horizontal lines refers, for each group, to the mean  $\pm$  standard deviation; P values were obtained using post-hoc Tukey's honest significant difference (HSD) test. **(b)** The distribution of retrobulbar cone volume grouped by skull morphology (brachycephalic, dolichocephalic and mesocephalic). The horizontal lines refer, for each group, to the mean  $\pm$  standard deviation; P values were obtained using post-hoc Tukey's HSD test. **(c)** The scatter plot shows the correlation between the dog's body weight (kg) and retrobulbar cone volume (mL). The straight blue line represents the regression line obtained using the least squares method, and the grey area shows the confidence band, setting confidence level at 95%.

To assess the relative value of each predictor, we built several nested models by starting with the simplest one, in which only body weight was used. The predictive accuracy of the different models is displayed in Figure 3.5. By adding the skull morphology to the weight, a relevant reduction in the prediction error was gained while the inclusion of the first-order interaction between morphology and weight, although significant, did not account for a further decrease in the prediction error.

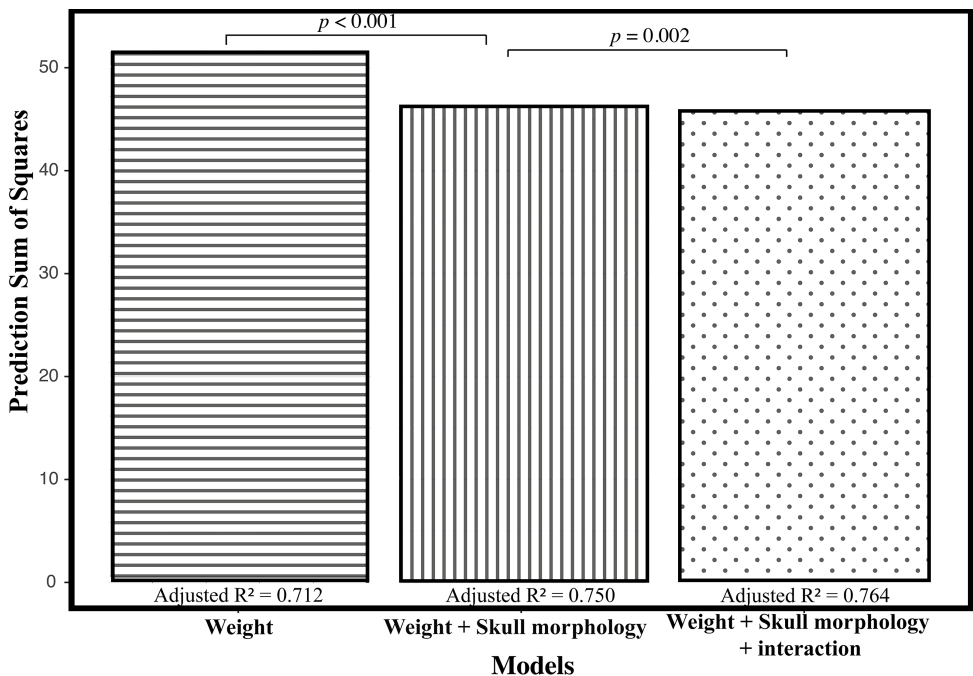


FIGURE 3.5 Graphical representation of the prediction sum of squares associated with estimated nested model; P values refer to the analysis of variance comparison between models.

Therefore, body weight and skull morphology were the only variables retained in the final model, accounting for 75% of the whole variability of the cone volume ( $R^2 = 0.75$ ). The model was overall significant ( $P < 0.001$ ). When accounting for all the variables in the model, for each kg increase in body weight, the retrobulbar cone volume increased by 0.06 mL (95% CI: 0.06 - 0.07 mL kg<sup>-1</sup>;  $P < 0.001$ ). In addition, in brachycephalic and dolichocephalic dogs, the retrobulbar cone volume was larger than in mesocephalic dogs (difference: + 0.57 mL, 95% CI 0.34 - 0.80 mL,  $P < 0.001$  and + 0.37 mL, 95% CI 0.11 - 0.64 mL,  $P < 0.001$ , respectively). Based on our model, the retrobulbar cone volume can be estimated in dogs based on their morphology and body weight using the following formulae, where coefficients are reported up to the fifth decimal digit to improve accuracy:

Retrobulbar cone volume (mL)

- 1)  $0.69238 + 0.06177 \times \text{BW in kg}$  for mesocephalic skull morphology dogs.
- 2)  $0.69238 + 0.06177 \times \text{BW in kg} + 0.57034$  for brachycephalic skull morphology dogs.
- 3)  $0.69238 + 0.06177 \times \text{BW in kg} + 0.37414$  for dolichocephalic skull morphology dogs.

### 3.5 DISCUSSION

In this study we were able to develop a formula to predict the volume of the intraconal space, as defined by the periorbita, using the dog's body weight and conformation. We found a positive association between the retrobulbar cone volume and dog's body weight, size, skull morphology and sex. In particular, using univariate analysis, the dog's size showed a positive linear association with cone volume, where larger sized dogs displayed significantly larger retrobulbar cone volumes than medium and small sized dogs. Sex also showed a significant association with retrobulbar cone volume, being larger in male dogs than in female dogs of the same skull morphology group. Such sexual dimorphism was not observed between the castrated or ovariohysterectomized dogs of either sex. As expected, skull morphology showed a significant association with retrobulbar cone volume, being larger in dolichocephalic and brachycephalic dogs than in mesocephalic dogs. Based on our findings, we were able to easily calculate the retrobulbar cone volume. For each of the three skull morphologies, an estimated coefficient was proposed to multiply by the dog's body weight (in kg). The numerical value, expressed in  $\text{mL}^{-1}$  eye, resulting from this mathematical calculation, theoretically corresponds to the VTBI required for intraconal retrobulbar anaesthesia. For the intraconal retrobulbar anaesthesia technique, a smaller volume of local anaesthetic solution is used to achieve anaesthesia and akinesia of the eye, compared with that needed for extraconal or periorbital infiltration techniques. Previously, different retrobulbar anaesthesia techniques and different injection volumes have been reported in dogs.<sup>11</sup> Accola et al.<sup>3</sup> injected 2 mL

(0.2 mL kg<sup>-1</sup>) of a 2% lidocaine solution through an inferior-temporal-palpebral approach in 10 kg Beagle dogs. They obtained adequate analgesia and a suitable distribution of the injectate within the retrobulbar cone. More recently, Chiavaccini et al.<sup>19</sup> reported a novel supratemporal approach for intraconal retrobulbar anaesthesia in canine cadavers. They suggested that an injection volume of only 0.1 mL kg<sup>-1</sup> of local anaesthetic solution versus 2 mL was needed for the inferior-temporal-palpebral approach. In their study, a 1:1 mixture of 0.5% bupivacaine with a contrast agent was deemed sufficient for intraconal retrobulbar anaesthesia in dogs, essentially filling 60% of the extraocular muscle cone. Klaumann et al.<sup>16</sup> used dogs' morphometric features, in addition to body weight, to estimate the ideal injection volume for retrobulbar anaesthesia. Given that the dog's splanchnocranium is less variable than the neurocranium, those authors correlated cranial length with periorbital length and suggested an injection volume of 0.1 mL of anaesthetic solution for each cm of cranial length. Based on the author's experience, an ultrasound-guided supratemporal approach for intraconal injection facilitates retrobulbar block in dogs, using volumes as small as 0.1 mL kg<sup>-1</sup>. The advantages derived from injecting a smaller volume within the extraocular muscle cone include a reduced risk of local anaesthetic toxicity avoiding proptosis and also an associated increase in the intraocular pressure. Under these circumstances, the availability of a mathematical formula to calculate the VTBI for intraconal retrobulbar anaesthesia could be a valuable aid for ophthalmic surgery.<sup>20</sup> The intraconal volume of 0.06 mL kg<sup>-1</sup> resulting from our calculation allows plenty of freedom for possible drug dilution and the use of drug combinations. Our data increase the practitioners' awareness of the

high variability in the retrobulbar cone volume between dogs of differing breeds and of the need to adjust this volume according to a dog's size and skull morphology. The main limitation of the present study was the relatively small number of dolichocephalic dogs in the analysed sample, probably owing to their low presence in the south of Italy. Moreover, the derived model should be validated using an independent external cohort in order to correct for overoptimism of the estimated prediction sum of squares. Further multicentre imaging studies will be needed to expand our statistical findings; additionally, several clinical intraconal retrobulbar anaesthesia studies will be required to test the effectiveness of the VTBI calculated using our formula. Based on our data, body weight and skull morphology are the main variables required to calculate the retrobulbar cone volume in dogs. Thereby, the volume of anaesthetic solution to be injected for an effective intraconal retrobulbar anaesthesia can be determined. A mathematical formula to calculate retrobulbar cone volume for each of the three canine skull morphologies is proposed. Further studies are needed to confirm the clinical effectiveness of the VTBI calculated when the proposed formula is used.

### 3.6 REFERENCES

1. Mathews K, Kronen PW, Lascelles D, Nolan A, Robertson S, Steagall PV, et al. Guidelines for Recognition, Assessment and Treatment of Pain. *Journal of Small Animal Practice*. 2014;**55**: E10-E68. <https://doi.org/10.1111/jsap.12200>
2. Shilo-Benjamini Y, Pascoe PJ, Maggs DJ, Hollingsworth SR, Strom AR, Good KL, et al. Retrobulbar vs peribulbar regional anesthesia techniques using bupivacaine in dogs. *Veterinary Ophthalmology*. 2019;**22**: 183-191. <https://doi.org/10.1111/vop.12579>
3. Accola PJ, Bentley E, Smith LJ, Forrest LJ, Baumel CA, Murphy CJ. Development of a retrobulbar injection technique for ocular surgery and analgesia in dogs. *Journal of the American Veterinary Medical Association*. 2006;**229**: 220-225. 10.2460/javma.229.2.220
4. Ahn J, Jeong M, Park Y, Lee Y, Lee E, Kim S, et al. Comparison of systemic atracurium, retrobulbar lidocaine, and sub-Tenon's lidocaine injections in akinesia and mydriasis in dogs. *Veterinary Ophthalmology*. 2013;**16**: 440-445. <https://doi.org/10.1111/vop.12026>
5. Palte HD. Ophthalmic regional blocks: management, challenges, and solutions. *Local and regional anesthesia*. 2015: 57-70.

6. Myrna KE, Bentley E, Smith LJ. Effectiveness of injection of local anesthetic into the retrobulbar space for postoperative analgesia following eye enucleation in dogs. *Journal of the American Veterinary Medical Association*. 2010;**237**: 174-177. 10.2460/javma.237.2.174
7. Ploog CL, Swinger RL, Spade J, Quandt KM, Mitchell MA. Use of lidocaine-bupivacaine–infused absorbable gelatin hemostatic sponges versus lidocaine-bupivacaine retrobulbar injections for postoperative analgesia following eye enucleation in dogs. *Journal of the American Veterinary Medical Association*. 2014;**244**: 57-62. 10.2460/javma.244.1.57
8. Zibura AE, Posner LP, Ru H, Westermeyer HD. A preoperative bupivacaine retrobulbar block offers superior antinociception compared with an intraoperative splash block in dogs undergoing enucleation. *Veterinary Ophthalmology*. 2020;**23**: 225-233. <https://doi.org/10.1111/vop.12708>
9. Oel C, Gerhards H, Gehlen H. Effect of retrobulbar nerve block on heart rate variability during enucleation in horses under general anesthesia. *Veterinary Ophthalmology*. 2014;**17**: 170-174. <https://doi.org/10.1111/vop.12061>
10. Vézina-Audette R, Steagall PVM, Gianotti G. Prevalence of and covariates associated with the oculocardiac reflex occurring in dogs during enucleation. *Journal of the American Veterinary Medical Association*. 2019;**255**: 454-458. 10.2460/javma.255.4.454

11. Shilo-Benjamini Y. A review of ophthalmic local and regional anesthesia in dogs and cats. *Veterinary Anaesthesia and Analgesia*. 2019;**46**: 14-27. <https://doi.org/10.1016/j.vaa.2018.10.004>
12. Shearin AL, Ostrander EA. Canine Morphology: Hunting for Genes and Tracking Mutations. *PLOS Biology*. 2010;**8**: e1000310. [10.1371/journal.pbio.1000310](https://doi.org/10.1371/journal.pbio.1000310)
13. Schoenebeck JJ, Ostrander EA. The Genetics of Canine Skull Shape Variation. *Genetics*. 2013;**193**: 317-325. [10.1534/genetics.112.145284](https://doi.org/10.1534/genetics.112.145284)
14. Giuliano EA. Regional Anesthesia as an Adjunct for Eyelid Surgery in Dogs. *Topics in Companion Animal Medicine*. 2008;**23**: 51-56. <https://doi.org/10.1053/j.ctsap.2007.12.007>
15. Abby Grace Drake, Christian Peter Klingenberg. Large-Scale Diversification of Skull Shape in Domestic Dogs: Disparity and Modularity. *The American Naturalist*. 2010;**175**: 289-301. [10.1086/650372](https://doi.org/10.1086/650372)
16. Klaumann PR, Moreno JCD, Montiani-Ferreira F. A morphometric study of the canine skull and periorbita and its implications for regional ocular anesthesia. *Veterinary Ophthalmology*. 2018;**21**: 19-26. <https://doi.org/10.1111/vop.12471>
17. Evans H. The skeleton In: Evans HE, de Lahunta A, eds. *Miller's Anatomy of the Dog St Louis, MO: Saunders*. 2013: 80-157.

18. Allen DM. The Relationship Between Variable Selection and Data Augmentation and a Method for Prediction. *Technometrics*. 1974;**16**: 125-127. 10.1080/00401706.1974.10489157
  
19. Chiavaccini L, Micieli F, Meomartino L, Duffee LR, Vesce G. A novel supra-temporal approach to retrobulbar anaesthesia in dogs: Preliminary study in cadavers. *The Veterinary Journal*. 2017;**223**: 68-70. <https://doi.org/10.1016/j.tvjl.2017.04.013>
  
20. Lin C-T, Hu C-K, Liu C-H, Yeh L-S. Surgical Outcome and Ocular Complications of Evisceration and Intraocular Prosthesis Implantation in Dogs with End Stage Glaucoma: a Review of 20 Cases. *Journal of Veterinary Medical Science*. 2007;**69**: 847-850. 10.1292/jvms.69.847

## Chapter IV

Retrobulbar filling for enophthalmos treatment in dogs: technique, description and computed tomography evaluation. Preliminary cadaveric study.

Dario Costanza, Leonardo Meomartino, Barbara Lamagna, Adelaide Greco, Erica Castiello, Pierpaolo Coluccia, Giuseppe Piegari, Ilaria D'Aquino, Francesco Lamagna.

Portions of this study were presented at the 2022 annual EVDI Congress, Edinburgh, Scotland, UK, 14 – 17 September 2022

#### 4.1 ABSTRACT

A new therapeutic approach for enophthalmos may be the retrobulbar lipofilling. This experimental, prospective, one group pre-test, post-test, method comparison study aims to standardize a technique of intraconal filling and to evaluate the degree of eyeball displacement by computed tomography (CT). Skull CT was performed on six dog cadavers before and after intraconal injection of two 5% iodinated, viscoelastic solutions, one per eye, using an ultrasound-guided supratemporal approach. The volume to be injected was estimated using formulas found in the literature for retrobulbar cone anaesthesia. After the CT, the dogs underwent necropsy and histopathology to evaluate damages eventually occurred to retrobulbar structures. Eyeball displacement was estimated using two CT-based methods, named  $M_1$  and  $M_2$ . The Wilcoxon signed-rank test revealed no significant difference between the two injected materials in both  $M_1$  ( $P > 0.99$ ), and  $M_2$  (lateral  $P = 0.84$ ; and rostral displacement  $P = 0.84$ ). A statistically significant difference was found between the pre- and post-injection group  $M_1$  ( $P = 0.002$ ),  $M_2$  ( $P = 0.004$ ) for the lateral and ( $P = 0.003$ ) for rostral displacement. Although the slight eyeball displacement, the retrobulbar filling can lead to enophthalmos resolution. Compared to  $M_1$ ,  $M_2$  has better defined anatomical landmarks. Further, preclinical in vivo studies are necessary to assess retrobulbar filling efficacy and safety.

## 4.2 INTRODUCTION

Enophthalmos is relatively common in dogs. It can result from Horner's syndrome, atrophy of the orbital and masticatory muscles or fat due to myositis or cellulitis, orbital, nasolacrimal duct or retrobulbar neoplasia, tetanus, orbital fractures secondary to trauma or resulting from orbitotomy<sup>1, 2</sup>. Furthermore, many dog breeds (i.e. Afghan Hound, Golden Retriever, Great Dane, Labrador Retriever, Newfoundland, Standard Poodle, Rottweiler and Weimaraner) could have enophthalmos due to the selective breeding processes for refined skull conformation. Additionally, the posterior displacement creates a pocket in the ventral conjunctival fornix where foreign material accumulates, leading even to altered tear drainage. This process hesitates in chronic conjunctivitis, nictitans hyperemia, and a slight mucoid discharge (medial canthal pocket syndrome).<sup>3</sup> In human medicine, the autologous fat intraconal injection (retrobulbar lipofilling) for enophthalmos resolution, mainly resulting from blow-out fractures or tumour resection, is well-described with excellent results and a low complication rate.<sup>4-10</sup> Among diagnostic imaging modalities, magnetic resonance imaging could provide detailed information regarding the nature and extent of concurrent soft tissue injuries within the retrobulbar space. On the other hand, computed tomography (CT) is the modality of choice for evaluating the orbital bony structures.<sup>11-13</sup> Furthermore, CT, due to its wide distribution, speed of acquisition, high spatial resolution, multiplanar reconstructions (MPR), 3D volume rendering, and the simultaneous visualization of the eyeball, skeletal structures, retrobulbar space and adnexa, is widely used for the evaluation of retrobulbar space.<sup>14</sup> In Veterinary Medicine, except for a single experimental study in rabbits,<sup>15</sup>

there are no published studies assessing the technique and feasibility of intraconal lipofilling for enophthalmos resolution in dogs. In the Authors opinion, as in humans, intraconal lipofilling could be a valuable method for enophthalmos treatment. Therefore, the primary aims of this study were to describe and evaluate a technique to inoculate within the retrobulbar space, two different materials, one per eye, with viscoelastic proprieties similar to the adipose tissue, and to evaluate the eyeball rostral displacement using CT. Secondary objective was to evaluate the presence of eventually occurring damage to retrobulbar structures through macroscopic and histopathological examination.

### **4.3 MATERIALS AND METHODS**

The single-centre experimental, prospective, one group pre-test, post-test, method comparison study was approved by the Clinical Ethical Review Board of the University of Napoli "Federico II" (PG/2022/0063335), and written owner consent was obtained for all the dogs included in the study. Dogs were included in the sample if: a) were euthanized for reasons unrelated to this study, b) had a certain degree of enophthalmos, c) intraconal injection and necropsy were performed on the same day. Exclusion criteria were the presence of alterations found on clinical examination or following CT examination in the eyeballs, retrobulbar space and ocular adnexa. The morphotype (dolichocephalic, mesaticephalic, brachycephalic), sex, weight and age of each dog cadaver included in the final sample were recorded. Skull CT was performed on each dog cadaver using a 16-slices computed tomography unit (GE BrightSpeed, GE Healthcare, Milwaukee, WI, USA). The images were acquired using a

standardized institutional protocol for the skull with the following parameters: sternal recumbency, tube potential 120 kVp, mA 180-250, rotation speed 0,8 seconds, slice thickness 0.625 mm, slice interval 0.625 mm, pitch: 0.925. Images were reconstructed using soft tissue and bone convolution algorithm (General Electric proprietary 'standard' and 'bone' respectively) with matching soft tissue window level (WL): 40, windows width (WW): 350 and bone windows (WL: 300, WW: 1500). After CT acquisition, two viscoelastic solutions: a) 3% sodium hyaluronate (VISCO-3 Sodium Hyaluronate, Zimmer Biomet, Warsaw, Poland) and b) carmellose sodium gel with 2,5% lidocaine (Luan 2,5% gel, Molteni Farmaceutici S.p.A, Scandicci FI, Italy) were mixed with methylene blue (Methylene Blue solution, Merck KGaA, Darmstadt, Germany) and 5% iodine-based, nonionic contrast medium (Iopamidol, Iopamiro 370 mgI/ml, Bracco Imaging S.p.A, Milano, Italy). The total volume of solution to be injected, expressed in mL, was estimated using the formula proposed by Greco et al.<sup>16</sup> for retrobulbar cone volume, taking into account the morphotype and the weight of each dog. The solutions were injected within retrobulbar space through a 18 Gauge needle using an ultrasound-guided supratemporal approach.<sup>17</sup> The same operator executed all injections. Solution A was injected within the right retrobulbar space of each specimen, while solution B in the left ones. After the injection, the CT exam was repeated using the same settings as the first acquisition. Finally, the dogs underwent necropsy for a macroscopic and histopathological examination to evaluate eventual damages to the eyeball, retrobulbar space and adnexa following the retrobulbar filling maneuver. Pre- and post-injection CT images of each dog were compared by a professor of Veterinary Radiology with a

Ph.D. and >25 of experience (L.M.) on a computer workstation (iMac 5K, 27-inch, Apple Inc., Cupertino, CA, USA) using an open-source DICOM viewer (Horos version 3.3.6, 64-bit, Nimble Co LLC d/b/a Purview, Annapolis, MD, USA, <https://www.horosproject.org>). Any eventual intraocular or extraconal distribution of the contrast medium was recorded.

Eyeball displacement was estimated subjectively, observing the macroscopic position of the eyeballs, and objectively, using two methods, named  $M_1$  and  $M_2$ . In  $M_1$  (Fig. 4.1A), the rostro-lateral displacement was evaluated on a dorsal-oblique plane tracing a line from the corneal surface to the optic canal. In  $M_2$ , the lateral displacement was assessed on the transverse plane (Fig. 4.1B), drawing a line from the frontal to the zygomatic bone and then from this line to the corneal surface, while the rostral displacement was evaluated on the dorsal plane (Fig. 4.1C), drawing a line from the maxillary to the zygomatic bone and then from this line to the corneal surface.

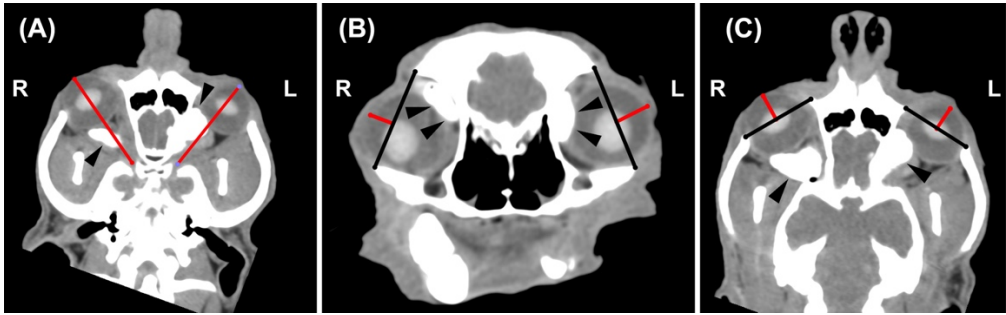


**FIGURE 4.4** (A) Dorsal-oblique, (B) transverse and (C) dorsal post-injection MPR image of the skull of a 17-year-old male mixed-breed dog. Soft tissue algorithm (manually windowed to  $WW = 350$ ,  $WL = 40$ ), slice thickness 0.625 mm, kVp 120, mAs 220. (A) In  $M_1$ , the eyeball displacement was evaluated on a dorsal-oblique plane, drawing a line from the optic foramen to the ipsilateral corneal surface (red lines). (B) In  $M_2$ , the lateral displacement was assessed on the transverse plane, drawing a line from the frontal to the zygomatic bone (black lines) and then from this line to the corneal surface (red lines), while the rostral displacement was evaluated on the dorsal plane (C), drawing a line from the maxillary to the zygomatic bone (black lines) and then from this line to the corneal surface (red lines). The contrast media mixed with the viscoelastic solutions (black arrowheads) is visible within the retrobulbar space.

Statistical analyses were performed by one of the authors (D.C.), a third-year Ph.D. student in Veterinary Diagnostic Imaging, using commercial statistical software (Prism version 9.5.0 (525), GraphPad Software San Diego, California, USA). Descriptive statistics were calculated for both pre- and post-injections groups using  $M_1$  and  $M_2$ . The Wilcoxon signed-rank test was used to assess the presence of significant differences between the left and right eyeballs in pre- and post-injection groups and then to evaluate the degree of rostro-lateral displacement for both methods. In all analyses,  $P < 0.05$  was considered statistically significant.

#### 4.4 RESULTS

The final sample consisted of 6 dogs [3 females (1 spayed) and 3 males) (4 mesaticephalic and 2 brachycephalic) for a total of 12 retrobulbar spaces. The breed represented were mixed breed (n = 4), English Cocker spaniel (n = 1), and Chihuahua (n = 1). The median weight was 9,4 kg (range 5 – 12,7 kg). The volume to be injected was between 0,4 – 0,9 mL. The ultrasound-guided intraconal filling was achieved in all the dogs without significant difficulties. An evident anterior displacement of the eyeballs was subjectively deemed adequate for all the dogs. The contrast medium, mixed within the injected solutions, was visible within all the retrobulbar spaces. The iodinated viscoelastic solution was completely intraconal in 7 retrobulbar space, while was partially or completely in the extraconal space in 3 and 2 retrobulbar space respectively. On necropsy, the injected material was still visible in the retrobulbar space in all the dogs. The ocular muscles and the optic nerve, macroscopically, were not damaged as they retained their original shape, position and colour. On histopathological examination, the examined ocular muscles and optic nerve were intact. Descriptive statistics, including the mean, range (minimum to maximum), standard deviation ( $\pm$ SD) and 95% confidence interval (CI) of the mean, for eyeball displacement calculated for the left, right and pooled eyeballs in both pre- and post-injection groups considering both M<sub>1</sub> and M<sub>2</sub> are reported in Table 4.1 and Table 4.2 respectively.

	MEAN ( $\pm$ SD)	95% CI	RANGE (MIN - MAX)
PRE RT (n = 6)	42.93 ( $\pm$ 3.44)	39.32 - 46.55	39.9 - 47.5
PRE LE (n = 6)	43.22 ( $\pm$ 3.59)	39.44 - 46.99	39.5 - 47.6
POST RT (n = 6)	45.03 ( $\pm$ 2.97)	41.91 - 48.15	41.6 - 48.5
POST LE (n = 6)	44.45 ( $\pm$ 3.61)	40.66 - 48.24	39 - 48
PRE GROUPED (n = 12)	43.08 ( $\pm$ 3.36)	40.94 - 45.21	39.5 - 47.6
POST GROUPED (n = 12)	44.74 ( $\pm$ 3.16)	42.73 - 46.75	39 - 48.5

TABLE 4.1 Descriptive statistics for  $M_1$  pre- and post- retrobulbar injection. Abbreviations: CI, confidence interval; GROUPED; grouped data of right and left eyeballs; POST, post-injection; PRE, pre-injection; LE, left; MIN, minimum; MAX, maximum; RT, right; SD, standard deviation.

DISPLACEMENT		MEAN ( $\pm$ SD)	95% CI	RANGE (MIN - MAX)
PRE RT (n = 6)	LD	0.63 ( $\pm$ 0.37)	0.24 - 1.02	0.27 - 1.25
	RD	0.72 ( $\pm$ 0.24)	0.46 - 0.98	0.47 - 1.09
PRE LE (n = 6)	LD	0.62 ( $\pm$ 0.32)	0.28 - 0.96	0.31 - 1.19
	RD	0.76 ( $\pm$ 0.21)	0.53 - 0.98	0.55 - 1.02
POST RT (n = 6)	LD	0.78 ( $\pm$ 0.33)	0.43 - 1.13	0.46 - 1.39
	RD	0.87 ( $\pm$ 0.26)	0.60 - 1.15	0.53 - 1.19
POST LE (n = 6)	LD	0.77 ( $\pm$ 0.31)	0.44 - 1.1	0.43 - 1.33
	RD	0.85 ( $\pm$ 0.18)	0.66 - 1.04	0.61 - 1.12
PRE GROUPED (n = 12)	LD	0.63 ( $\pm$ 0.33)	0.42 - 0.84	0.27 - 1.25
	RD	0.74 ( $\pm$ 0.22)	0.6 - 0.88	0.47 - 1.09
POST GROUPED (n = 12)	LD	0.77 ( $\pm$ 0.30)	0.58 - 0.97	0.43 - 1.39
	RD	0.86 ( $\pm$ 0.21)	0.73 - 1	0.53 - 1.19

TABLE 4.2 Descriptive statistics for  $M_2$  pre- and post-retrobulbar injection. Abbreviations: CI, confidence interval; GROUPED; grouped data of right and left eyeballs; POST, post-injection; PRE, pre-injection; LE, left; LD, lateral displacement of the eyeball; MIN, minimum; MAX, maximum; RD, rostral displacement of the eyeball; RT, right; SD, standard deviation.

The Wilcoxon signed-rank test revealed no significant difference between the right and left eyeballs in the pre-injection group for the rostro-lateral displacement in  $M_1$  ( $P = 0.53$ ), and for the lateral ( $P = 0.31$ ) and rostral ( $P > 0.9$ ) displacement in  $M_2$ . No significant differences were also found between the right and left eyeball in the post-injection group for the rostro-lateral displacement in  $M_1$  ( $P > 0.99$ ), and for the lateral ( $P = 0.84$ ) and rostral ( $P = 0.84$ ) displacement in  $M_2$ . Consequently, for the following statistical analyses, the eyeballs and respective retrobulbar spaces were pooled together. The Wilcoxon signed-rank test revealed a statistically significant difference between the pre- and post-injection group for the pooled data for the rostro-lateral displacement in  $M_1$  ( $P = 0.002$ ; Figure 4.2), lateral ( $P = 0.004$ ; Figure 4.3A) and rostral displacement in  $M_2$  ( $P = 0.003$ ; Figure 4.3B).

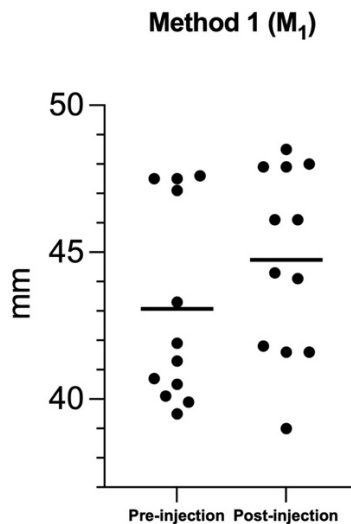


FIGURE 4.2 Scatter plot comparing the rostro-lateral displacement in millimeters (mm) between the pre- and post-injection groups using Method 1 ( $M_1$ ). The solid black lines represent the mean.

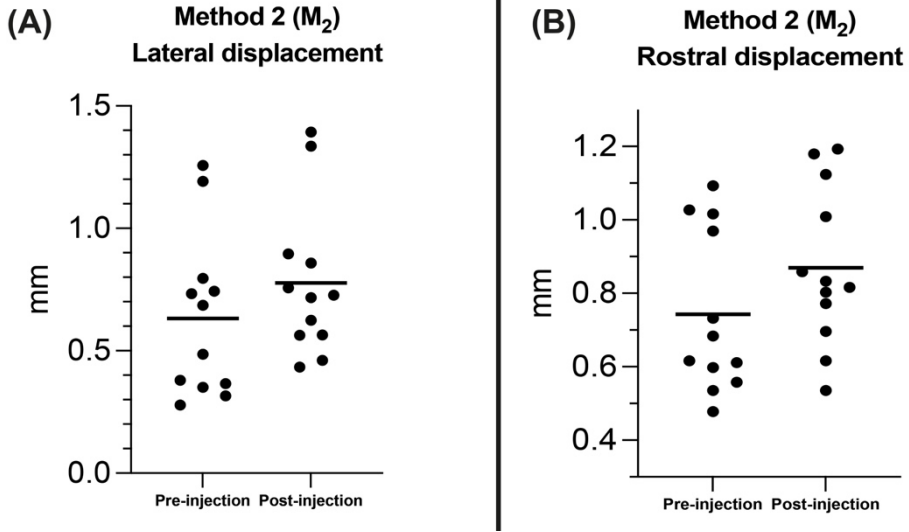


FIGURE 4.2 Scatter plots comparing the lateral (A) and rostral (B) displacement in millimeters (mm) between the pre- and post-injection groups using Method 2 (M<sub>2</sub>). The black solid lines represent the mean..

## 4.5 DISCUSSION

The primary aims of this study was to describe a technique to treat enophthalmos by injecting two different materials, with viscoelastic properties similar to adipose tissue, within the retrobulbar space and to evaluate the eyeball rostro-lateral displacement using CT. The results demonstrated that the retrobulbar filling is a technique relatively simple to perform and without any contraindications. The injection technique adopted was derived from the supratemporal approach proposed by Chiavaccini *et al.*<sup>17</sup> However, differently from the original method, in our study, the injection was performed under ultrasound guidance to avoid possible damage to the eyeballs and retrobulbar structures, (i.e. the optic nerve and the vessels). The degree of eyeball rostral and lateral displacement was judged subjectively good and the amount of material injected, nevertheless it was only a few mL, was enough to obtain it.

Anyway, the eyeball rostral and lateral displacement was objectively evaluated using two different CT-based methods. The statistical analyses found no significant differences between the two injected materials. and both CT methods we proposed to evaluate the eyeball's degree of cranial and lateral displacement confirmed a significant displacement compared to the starting condition. Both the CT methods demonstrate to be reliable. However, although  $M_1$  allows the assessment of the rostral and lateral eyeball advancement with a single measurement,  $M_2$  provides more defined anatomical landmarks and makes it easier to compare the pre- and post-injection series. Our methods are similar to the lateral and superior protrusion indexes described by Ye *et al.*<sup>4</sup> in human medicine and confirm

the usefulness of CT in pre-operative planning and evaluation of the degree of correction of enophthalmos. In human medicine, only a few studies estimated the amount of fat to be injected before the retrobulbar filling.<sup>4, 5</sup> In others, the amount of autologous fat to be injected was at the clinician's discretion according to the visual degree of improvement achieved.<sup>6, 8-10</sup> Its lack of precision may be responsible for early diplopia and unsatisfactory aesthetic results requiring additional injections.<sup>4</sup> In our study, the volume to be injected was estimated by formulae proposed by *Greco et al.*<sup>16</sup> to calculate the retrobulbar cone volume using CT. This method has proved to be effective; however, for *in vivo* inoculations, considering that a reabsorption rate of up to 30-40% of the injected autologous fat is expected in a few weeks, this loss must have to be taken into account; otherwise, additional inoculations could be necessary.<sup>4-6</sup> In our study, the inoculated iodinated viscoelastic solutions were partially or completely extraconal in 3 and 2 cases respectively. This is most likely related to the inexperience of the author in performing this injection but also to a partial leakage of the more fluid component of the solution from the intraconal space. The inoculation of fat within the extraconal space can cause a slight swelling of the eyelids, inadequate cranial displacement of the eyeball and post-operative transitory pain. However, according to the literature, extraconal migration of autologous fat does not alter the function of extraocular muscles, optic vessels, and nerve.<sup>4, 6, 8, 10</sup> Differently in human medicine, hard materials like hydroxyapatite, cartilages, silicone or glass beads have been implanted in the orbit for the same purpose. However, these materials do not meet the physiologic and anatomical requirements of the orbit, so major complications such as vision loss, ocular motility restriction,

ocular nerve and vessels damage, and migration of these implants can occur.<sup>4, 6, 8, 12</sup> Minor complications related to autologous fat inoculation and reported in the literature include intraoperative retrobulbar haemorrhage, post-operative pain, periorbital swelling, ptosis and blurring of the vision. Most of these complications tend to resolve in a short period and without irreversible damage to relevant anatomical structures.<sup>6, 10</sup> Potential major complications such as acute blindness, fat embolism and oculocardiac reflex have not been reported.<sup>6, 8, 18</sup> The method's safety was also confirmed in our study by the absence of relevant damages at the necropsy and histopathological exam. Indeed, no injury to the eyeball, the ocular muscles, vessels and optic nerve was demonstrated. Obviously, further pre-clinical studies on living subjects are necessary to assess the number and extent of complications following this procedure. The main limitation of our study is represented by its cadaveric nature, hence the impossibility of confirming with certainty the lack of damage to the optical structures and other major complications such as vision loss. Additionally, the use of materials that, although viscoelastic, has different physical properties to autologous fat, so the amount of material to be inoculated and the result obtained may differ from our results. In conclusion, the retrobulbar filling could represent a possible technique for the treatment of enophthalmos in dogs. The supratemporal approach adopted for the injection manouvre has proved to be relatively simple and safe, without macroscopic and histopathological lesions to the retrobulbar structures. Both proposed CT methods used to estimate the degree of ocular displacement were able to detect the degree of rostral and lateral displacement of the eyeball. Further preclinical *in vivo* studies are necessary to investigate the procedure's

effectiveness, the modalities and sites of autologous fat harvesting and the rate of major complications.

#### 4.6 REFERENCES

1. Bernhard M Spiess SAP. Diseases and Surgery of the Canine Orbit. In: Kirk N Gelatt BCG, Thomas J Kern. (ed): *Veterinary Ophthalmology*. Oxford, OX4 2DQ, UK: Wiley-Blackwell, 2013;793 - 831.
2. Jones BR, Studdert VP. Horner's syndrome in the dog and cat as an aid to diagnosis. *Aust Vet J*. 1975;**51**: 329-332. 10.1111/j.1751-0813.1975.tb15939.x
3. Rubin LF. *Inherited Eye Diseases in Purebred Dogs*: Williams & Wilkins, 1989.
4. Ye L, Zhang L, Zhu Y, Zhang Y, Wu W, Zhang Y. Enophthalmos: Exploration of Quantitative Treatment With Retro-Orbital Fat Globules Injection. *Journal of Craniofacial Surgery*. 2020;**31**: 54-57. 10.1097/scs.0000000000005847
5. Cervelli D, Gasparini G, Moro A, Grussu F, Boniello R, Pelo S. Retrobulbar Lipofilling to Correct the Enophthalmos. *Journal of Craniofacial Surgery*. 2011;**22**: 1918-1922. 10.1097/SCS.0b013e318210bbc8
6. Chen H, Zhang Q, Qiu Q, Yang Z. Autologous Fat Graft for the Treatment of Sighted Posttraumatic Enophthalmos and Sunken Upper Eyelid. *Ophthalmic Plastic & Reconstructive Surgery*. 2018;**34**: 381-386. 10.1097/iop.0000000000001028

7. Agostini T, Perello R, Arcuri F, Spinelli G. Retroseptal Lipotransfer to Correct Enophthalmos in the Posttraumatic Amaurotic Eye. *Plastic and Reconstructive Surgery*. 2014;**134**: 989e-990e. 10.1097/prs.0000000000000664
8. Hardy TG, Joshi N, Kelly MH. Orbital volume augmentation with autologous micro-fat grafts. *Ophthalmic Plast Reconstr Surg*. 2007;**23**: 445-449. 10.1097/iop.0b013e31815928f8
9. Hunter PD, Baker SS. The treatment of enophthalmos by orbital injection of fat autograft. *Arch Otolaryngol Head Neck Surg*. 1994;**120**: 835-839. 10.1001/archotol.1994.01880320037009
10. Fox DM. Orbital Fat Injection: Technique and 5-Year Follow-Up. *Aesthetic Plast Surg*. 2019;**43**: 123-132. 10.1007/s00266-018-1205-z
11. Penninck D, Daniel GB, Brawer R, Tidwell AS. Cross-sectional imaging techniques in veterinary ophthalmology. *Clinical Techniques in Small Animal Practice*. 2001;**16**: 22-39. <https://doi.org/10.1053/svms.2001.22802>
12. Dubois L, Steenen SA, Gooris PJ, Bos RR, Becking AG. Controversies in orbital reconstruction-III. Biomaterials for orbital reconstruction: a review with clinical recommendations. *Int J Oral Maxillofac Surg*. 2016;**45**: 41-50. 10.1016/j.ijom.2015.06.024

13. Ramieri G, Spada MC, Bianchi SD, Berrone S. Dimensions and volumes of the orbit and orbital fat in posttraumatic enophthalmos. *Dentomaxillofacial Radiology*. 2000;**29**: 302-311.  
[10.1038/sj/dmfr/4600551](https://doi.org/10.1038/sj/dmfr/4600551)
14. Scrivani PV. Sense Organs, Circulatory System, and Endocrine System. In: Scrivani PV (ed): *Veterinary Head and Neck Imaging*, 2022;673-772.
15. Cakir B, Aygit AC, Omur-Okten O, Yalcin O. Retro-Orbital Intraconal Fat Injection: An Experimental Study in Rabbits. *Journal of Oral and Maxillofacial Surgery*. 2012;**70**: 242-250.  
[10.1016/j.joms.2011.02.091](https://doi.org/10.1016/j.joms.2011.02.091)
16. Greco A, Costanza D, Senatore A, Bruzzese D, Micieli F, Chiavaccini L, et al. A computed tomography-based method for the assessment of canine retrobulbar cone volume for ophthalmic anaesthesia. *Veterinary Anaesthesia and Analgesia*. 2021;**48**: 759-766.  
<https://doi.org/10.1016/j.vaa.2021.03.015>
17. Chiavaccini L, Micieli F, Meomartino L, Duffee LR, Vesce G. A novel supra-temporal approach to retrobulbar anaesthesia in dogs: Preliminary study in cadavers. *The Veterinary Journal*. 2017;**223**: 68-70.  
<https://doi.org/10.1016/j.tvjl.2017.04.013>

18. Manson PN, Grivas A, Rosenbaum A, Vannier M, Zinreich J, Iliff N. Studies on enophthalmos: II. The measurement of orbital injuries and their treatment by quantitative computed tomography. *Plast Reconstr Surg.* 1986;77: 203-214.

## Chapter V

Computed Tomographic assessment of pituitary gland dimensions and reference values in domestic short-haired cats.

Dario Costanza, Adelaide Greco, Luigi Auletta, Erica Castiello, Pierpaolo Coluccia, Luigi Navas, Leonardo Meomartino.

Portions of this study were presented as an oral communication at the 75th SISVET Congress, Lodi (Italy), 15 – 18 June 2022

## 5.1 ABSTRACT

The detection of subtle changes in the pituitary size has important diagnostic and therapeutic implications since the gland plays a major role in regulating the endocrine system. In cats, a few studies established the cut-offs values of linear dimensions of the pituitary gland, but those values were determined on small and inhomogeneous samples. The aims of this retrospective, interval reference study were: to determine by computed tomography the reference values for pituitary linear dimensions and for the pituitary-to-brain (P:B) ratio; to evaluate the intra- and inter-observer agreement of measurements; to assess the effects of sex, age and weight in a sample of domestic short-haired cats. Exclusion criteria were clinical, laboratory or CT alterations related to the pituitary gland or brain disease, fractures of the neurocranium, and a definitive diagnosis of diabetes mellitus. Pituitary dimensions and brain area were assessed by two different observers using multiplanar reconstructions and automated segmentation tools. Fifty-one cats were included in the final sample. The intraclass correlation coefficient for intra- and inter-observer reliability showed good/excellent and moderate/good reliability, respectively. No differences between sexes were detected ( $P > 0.05$ ). Findings from the current study provided as normal reference cut-off values for pituitary height (1.88 – 4.01) and P:B ratio (0.25 – 0.49), useful for assessing abnormally enlarged pituitary gland in DSH cats.

## 5.2 INTRODUCTION

The pituitary gland plays a pivotal role in regulating the endocrine system through the production, storage, and release of various hormones.<sup>1</sup> Pituitary tumors can originate from different cell lineages and can be either functional or non-functional. The clinical signs associated with the neoplasm depend on the secretory properties but also on the tumor's size. Indeed, also non-functional tumors can become clinically relevant when they enlarge enough to cause neurologic signs.<sup>2</sup> Furthermore, pituitary tumors can be incidental findings when skull imaging is performed for unrelated reasons (incidentalomas).<sup>3</sup> In humans, according to 2017 WHO "*classification of tumors of the pituitary gland*", pituitary neoplasms can be classified as adenomas or carcinomas. The latter is defined only by demonstrating metastatic spread.<sup>4</sup> This classification mainly focuses on immunohistochemical classification according to the hormone that the tumor express and so can be further subdivided into melanotroph, corticotroph, thyrotroph, lactotroph, somatotroph or gonadotroph. In dogs, corticotroph (ACTH-secreting) adenomas and adenocarcinomas responsible for pituitary-dependent hyperadrenocorticism prevail, while in cats, somatotroph (GH-secreting) tumors are the most reported.<sup>5</sup> In this last, the excessive secretion of growth hormone can result in chronic hypersomatotropism that can cause acromegaly and insulin resistance, due to the concomitant increase of insulin-like growth factor-1 (IGF-1). Of note, cats affected by somatotroph pituitary tumors are often brought to consultation for clinical signs related to poorly controlled diabetes, such as polyuria, polydipsia and polyphagia, rather than somatic changes due to acromegaly.<sup>6-8</sup> Somatotroph adenoma is the most reported pituitary tumor

in middle-aged to older male cats. Domestic short-haired (DSH) cats and Maine Coons seem predisposed.<sup>6-8</sup> The detection of anatomical alterations of the pituitary gland is performed using Magnetic Resonance Imaging (MRI) or Computed Tomography (CT).<sup>9</sup> These imaging techniques are paramount for diagnosis and for planning surgery or radiotherapy.<sup>3</sup> In many cases, the diagnosis of pituitary macroadenoma is straightforward since the pituitary mass dorsally protrudes from the *sella turcica* and compresses the adjacent brain parenchyma, sometimes with associated neurological signs.<sup>3, 9, 10</sup> Differently, in the case of microadenomas there are only subtle and often not visible change in pituitary size and contours.<sup>8, 10</sup> In literature there are few studies where the linear dimensions of the pituitary gland (height, width, and length) were established in cats using both MRI<sup>11</sup> and CT<sup>12-14</sup>. In order to increase diagnostic accuracy in the detection of pituitary microadenomas, the pituitary gland was also evaluated by Tyson *et al.*<sup>13</sup> using dynamic scans since pituitary tumors can alter the normal network of pituitary vessels and, consequently, the enhancement pattern. In order to address variation in pituitary gland size between dogs and cats of different sizes and breeds, the pituitary height-to-brain ratio (P:B ratio) was introduced.<sup>12, 15</sup> However, those studies were performed on cats using third-generation CT units<sup>12</sup> or thick MRI slices<sup>11</sup> and made on small and inhomogeneous samples. More recently, a study aimed to evaluate possible differences in pituitary size between mesaticephalic and brachycephalic cats found a significant difference between the two skull morphotypes.<sup>14</sup> These results highlight the need to obtain reference measures of the pituitary gland according to morphotype or, even better, according to breed. Of note, the DSH represents the most diffused cat worldwide.<sup>16</sup> We hypothesised that the

reference intervals for pituitary linear dimensions (height, length, and width) and the P:B ratio in DSH cats may be different than previously reported. Therefore, the primary aim of the present study was to establish normal reference range values of the linear pituitary dimensions and the P:B ratio in DSH cats. Secondary objectives were to evaluate the influence of age, body weight and sex on pituitary dimensions and P:B ratio. Finally, to evaluate the intra- and inter-observer agreement among two observers with different levels of expertise.

### **5.3 MATERIALS AND METHODS**

The single-centre, retrospective, reference interval, intra- and inter-observer agreement study was approved by the Ethical Animal Care and use committee of the University of Naples “Federico II”. The electronic clinical records and CT reports of DSH cats referred to the Interdepartmental Centre of Veterinary Radiology of the University of Naples “Federico II” in the set study period between September 2018 and October 2022 were retrieved from the picture archiving and communication system (dcm4chee-arc-light version 5.11.1, <http://www.dcm4che.org>) and CT images were reviewed. CT exams were performed for various reasons, including nasal discharge, nasopharyngeal polyps and other upper respiratory airways pathologies, eye and retrobulbar disease, oral pathologies, otitis media, and metastasis exclusion. Patients were excluded from the study if they had clinical, laboratory, or CT final report reporting alterations related to a) pituitary gland disease, b) neurologic signs different from vestibular symptoms, c) intracranial lesion detected on CT, d) fractures or conformational alterations of the neurocranium, e) polyuria or polydipsia, f) signs of acromegaly, d)

definitive diagnosis of diabetes mellitus. As part of the inclusion criteria for the current study, all CT studies were performed using the same CT unit and the same protocol. More in detail, all the patients were under general anaesthesia (the anaesthetic protocol adopted varied depending on the decision of the anesthesiologist in charge) and were positioned in sternal recumbency within a radiolucent polyurethane vacuum immobilisation mattress (Vacuumat, Génia, St. Hilaire de Chaléons, France) and with the forelimbs pulled caudally along the thorax. Computed tomography studies were obtained using a 16-slices MDCT unit (BrightSpeed, General Electric Healthcare, Milwaukee, WI, USA). All the studies were acquired using the same protocol: helical mode; slice thickness of 0.625 mm; pitch 0.9375:1; tube potential 120 kVp, 200 mA, 1-second tube rotation speed; soft tissue and bone reconstruction algorithms (General Electric proprietary “standard” and “bone” filters); post-contrast images acquired after a delay of 60 seconds. All the patients received a standardised intravenous dose (740 mgI/kg, i.e. 2ml/kg) of iopamidol (Iopamiro 370mgI/ml, Bracco Imaging s.p.a., Milano, Italy) using a rate of infusion of 1 ml/s followed by a 5 ml saline flush through a double-barrel power injector (EmpowerCTA<sup>+</sup>, Bracco Imaging s.p.a., Milano, Italy).

The sex, neutering status, weight (in kilograms), and age (in months) were recorded for each cat included in the preliminary sample group. After a preliminary evaluation, L.M., a professor of Veterinary Radiology with a Ph.D. and >25 of experience, decided to include or exclude each cat from the definitive sample group. CT studies were excluded from the definitive sample group if a) the postcontrast series of the skull acquired with soft tissue reconstruction algorithm was not available, b) the quality of the images was inadequate for a correct

interpretation, c) the presence of beam hardening artifacts preventing a correct evaluation of the pituitary gland. The same author anonymised all the CT studies before submitting them to two observers which reviewed the images using a commercial DICOM viewer software (Philips Extended Brilliance Workspace v. 4.5.5). Observer 1 (D.C.), a third-year Ph.D. student in Diagnostic Imaging and observer 2 (P.C), a veterinarian with two years of expertise in CT. The two observers were blinded regarding the clinical data and reasons for CT examination. All the measurements were performed once by each observer, independently and blinded to the results reported by the other. A pituitary gland measurement method was established prior to the analysis by two authors (D.C. and L.M) and recorded on a portable document file. Pituitary linear dimensions (height, length, width) expressed in millimeters (mm) were measured using electronic calipers on post-contrast images displayed using a standardised window [window width (WW): 450, window level (WL): 200]. Measurements were made on multiplanar reconstructions (MPR) images in order to obtain the best visualisation of the pituitary gland and avoid interpreting the *dorsum sellae* as a pituitary mass.<sup>10</sup> The pituitary height (PH) was measured at the level of the *pituitary fossa*, perpendicular to the basisphenoid bone, where the maximal pituitary height was visible both on the transverse plane (PHT) (Figure 5.1A) and on the sagittal plane (PHS) (Figure 5.1D). The pituitary length (PL) was measured on the sagittal plane where the maximal length was visible, parallel to the basisphenoid bone (Figure 5.1D). The pituitary width (PW) was determined on the transverse plane at the point of maximal width of the gland (Figure 5.1C). The brain area (BA) expressed in mm<sup>2</sup> was measured on the same slice of the PHT using an automated segmentation

tool (Figure 5.1B). When deemed necessary, the observer used the bone reconstruction algorithms with associated high contrast window (WW = 2000, WL = 800) to better delineate the brain edges.

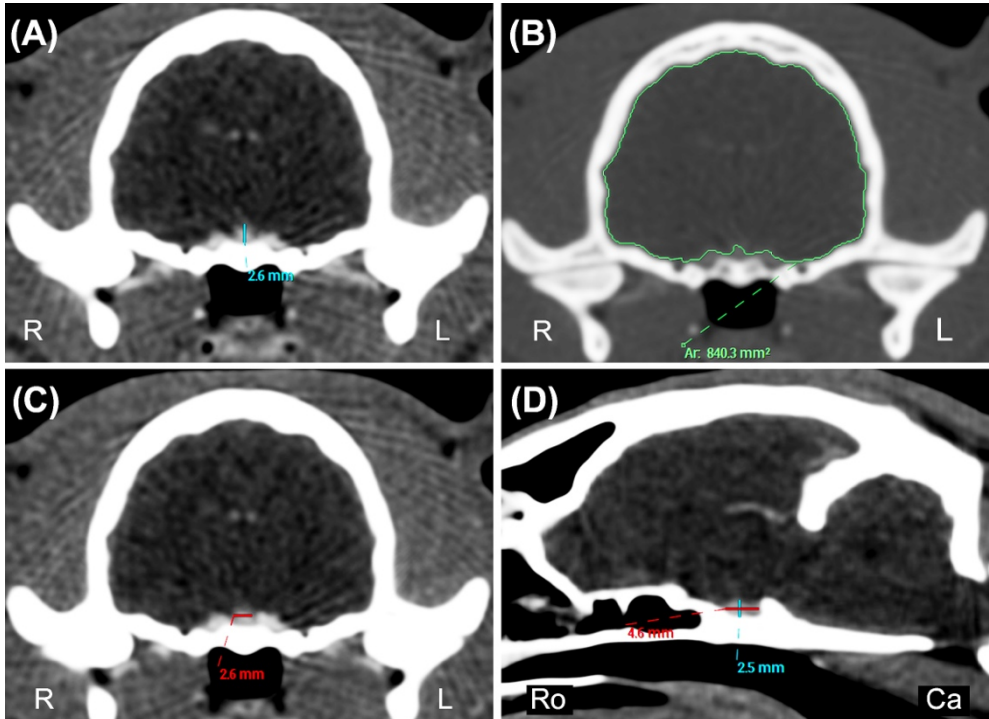


**FIGURE 5.5** **A-C** transverse and **D** sagittal soft tissue algorithm postcontrast CT images of the skull of a twelve-month-old DSH cat. **A**, Pituitary height (blue line) measured on the transverse plane (PHT) at the level of the pituitary fossa, perpendicular to the basisphenoid bone. **B**, Brain area (BA, green line) measured on the transverse plane, at the same level of the PTH using an automated segmentation tool. **C** Pituitary width (red line) measured on the transverse plane (PW) at the point of maximal width of the gland. **D** Pituitary height (blue line) measured on the sagittal plane (PHS) perpendicular to the basisphenoid bone and pituitary length (PL, red line) measured where the maximal length of the pituitary gland was visible and parallel to the basisphenoid bone. **A**, **C**, **D** manually windowed to WW = 455, WL = 234; **B** manually windowed to WW = 2000, WL = 800. Ca: Caudal; L: Left; R: Right; Ro: Rostral.

All the data were reported in an electronic spreadsheet (Microsoft Excel version 16.52 2021, Microsoft Corp. Redmond, WA, USA) and the P:B ratio was automatically computed for each cat as already reported in the literature:

$$\text{P:B ratio} = \frac{PHT(mm) \times 100}{BA(mm^2)}$$

Two months later, to assess the intra-observer agreement, the measurements were repeated once, independently by each of the two observers, on a smaller sample of thirty re-anonymised and re-randomly selected CT exams.

Statistical analyses were performed by one of the authors (L.A., former researcher with a Ph.D. and ten years of experience and specific training in statistics) using commercial software (JMP<sup>®</sup> Pro, v. 16.0, SAS Institute, Cary, NC, USA; MedCalc version 19.2.6, MedCalc Software Ltd, Acacialaan 22 8400 Ostend, Belgium; IBM<sup>®</sup> SPSS<sup>®</sup>, v. 26.0, IBM, Armonk, NY, USA). The normality of data was evaluated with the Shapiro-Wilk's *W* test. Continuous data were reported as mean  $\pm$  SD or median (range) depending on the distribution. For inter-observer agreement, measurements belonging to all the patients were included in the analysis, while for the intra-observer, only the measurements of the smaller sample were considered. For both inter- and intra-observer agreement, a two-way mixed effects intraclass correlation coefficient (ICC) for single measurement or single observer accordingly, and absolute agreement was calculated; the relative 95% confidence intervals (CI) were calculated, as well. The ICC was categorized according to Koo and Li.<sup>17</sup> Based on the reliability analysis results, all intra- and inter-observer measurements with an ICC  $>$  0.80 were averaged and subsequently analysed. For measurements that did not reach this value, the first measurements of observer 1, considered the most experienced, were used.

A Bland-Altman plot was used to explore the differences between PHS and PHT. The bias and 95% limits of agreement were calculated. Correlations between the measurements and body weight were tested with Pearson's correlation coefficient ( $r$ ), whereas those between the measurements and age using Spearman's rank correlation coefficient ( $r_s$ ). Finally, differences between males and females were tested with a pooled Student's  $t$ -test, with Welch's correction since variances resulted significantly different at the  $F$  test (PL, PW, BA, and P:B ratio), or a Mann-Whitney's  $U$  test (PHT and PHS), according to sex distribution and non-considering the neutering status. Finally, the reference range for each measurement was calculated according to the American Society for Veterinary Clinical Pathology (ASCV) guidelines for reference intervals.<sup>18</sup> Briefly, outliers were automatically identified according to Reed *et al.*<sup>19</sup> Then, data distribution was tested automatically with the Shapiro-Wilk's  $W$  test. Reference lower and upper limits, and the corresponding 90% CI were then calculated employing the robust method following Clinical Laboratory and Standards Institute (CLSI) recommendations (CLSI C28-A3), with bootstrapping (1000 iterations). No partitioning into subclasses based on age, body weight or sex was applied according to their lacking of correlation with the measurements. In all analyses,  $P < .05$  was considered statistically significant.

## 5.4 RESULTS

A total of the 59 CT studies of DSH cats performed in the set period were found and included in the preliminary group. After the preliminary review, 51 CT studies met the inclusion criteria, while eight were excluded for the following reasons: brain neoplasia ( $n = 4$ ), deformed cranium ( $n = 2$ ), and lack of post-contrast images ( $n = 2$ ). The DSH cats included in the final sample were 4 intact females (8%), 26 (51%) spayed females, 7 (14%) intact males, and 14 (27%) castrated males. The median age was 72 months (range 2 – 180), and the weight  $4.6 \pm 1.5$  kg. In all the cats included in the final sample, the pituitary gland was distinguishable from the adjacent structures with a good contrast enhancement and all the predetermined measurements were obtained. Sometimes, it was challenging to identify the pituitary edges with absolute precision due to the pituitary gland's small size. Additionally, since in some cats the gland's position was slightly oblique to the respect of the *sella turcica*, it was necessary to tilt the sagittal plane on MPR to determine PHS and PL to the best. For the determination of the BA, the automated segmentation tool allowed for a rapid delimitation of the brain area. Results for inter-observer agreement are summarised in Table 5.1. All measurements were within the moderate reliability class, but the BA, for which good reliability was detected.

<b>Measurement</b>	<b>ICC</b>	<b>95% CI</b>	<b>P</b>
PHT	0.69	0.38 – 0.84	<0.0001
PHS	0.58	0.37 – 0.74	<0.0001
PL	0.58	0.36 – 0.73	<0.0001
PW	0.66	0.46 – 0.79	<0.0001
BA	0.81	0.50 – 0.91	<0.0001

*TABLE 5.6 Intraclass correlation coefficients (ICC), relative 95% confidence intervals and p-values for the inter-observer reliability test. Abbreviations: PHT: pituitary height in the transverse plane; PHS: pituitary height in the sagittal plane; PL: pituitary length; PW: pituitary width; BA: brain area.*

Results for the intra-observer agreement are summarised in Table 5.2. Reliability was good for all measurements from observer 1, but for PL, that resulted moderate; on the other hand, reliability resulted moderate for all measurements from observer 2, but for BA, that resulted excellent.

Measurement	Operator 1			Operator 2		
	ICC	95% CI	P	ICC	95% CI	P
PHT	0.81	0.63 – 0.91	<0.0001	0.66	0.17 – 0.86	<0.0001
PHS	0.87	0.71 – 0.94	<0.0001	0.60	-0.04 – 0.85	<0.0001
PL	0.51	0.19 – 0.73	0.001	0.70	0.10 – 0.89	<0.0001
PW	0.78	0.59 – 0.89	<0.0001	0.60	0.08 – 0.83	<0.0001
BA	0.82	0.66 – 0.91	<0.0001	0.92	0.84 – 0.96	<0.0001

TABLE 5.2 Intraclass correlation coefficients (ICC), relative 95% confidence intervals and p-values for the intra-observer reliability test. Abbreviations: CI, confidence interval; BA, brain area; ICC, intraclass correlation coefficient; P:B ratio, pituitary gland height to brain area ratio; PHS, maximal pituitary height on the sagittal plane; PHT, maximal pituitary height on the transverse plane; PL: pituitary length; PW: pituitary width.

All the measures were weakly correlated with body weight, whereas only PHS and PL weakly correlated with age. No differences between sexes were detected for any measurement (PHT,  $P = 0.40$ ; PHS,  $P = 0.68$ ; PL,  $P = 0.31$ ; PW,  $P = 0.21$ ; BA,  $P = 0.30$ ; P:B ratio,  $P = 0.94$ ). Correlation coefficients and relative  $p$ -values are summarised in Table 5.3.

Measurement	Mean $\pm$ SD	Range (Min – Max)	Lower limit (90% CI)	Upper limit (90% CI)
PHT (mm)	2.94 $\pm$ 0.52	2.0 – 4.1	1.88 (1.68 – 2.10)	4.01 (3.81 – 4.20)
PHS (mm)	2.95 $\pm$ 0.55	1.9 – 4.0	1.84 (1.63 – 2.08)	4.10 (3.89 – 4.27)
PL (mm)	3.17 $\pm$ 0.52	2.0 – 4.4	2.13 (1.92 – 2.37)	4.23 (4.03 – 4.42)
PW (mm)	3.24 $\pm$ 0.61	2.1 – 4.8	1.92 (1.66 – 2.15)	4.41 (4.12 – 4.71)
BA (mm <sup>2</sup> )	789.02 $\pm$ 61.85	647.87 – 962.85	659.51 (634.51 – 687.61)	910.96 (883 – 938.01)
P:B ratio	0.37 $\pm$ 0.06	0.25 – 0.48	0.25 (0.23 – 0.28)	0.49 (0.47 – 0.51)

TABLE 5.3 Mean  $\pm$  standard deviation, upper and lower limits of the reference value (and corresponding 90% CI) of the pituitary gland linear measurements, brain area and pituitary-to-brain ratio. Abbreviations. CI, confidence interval; BA, brain area; Max, maximum; Min, minimum; P:B ratio, pituitary gland height to brain area ratio; PHS, maximal pituitary height on the sagittal plane; PHT, maximal pituitary height on the transverse plane; PL: pituitary length; PW: pituitary width; SD, standard deviation.

The PHT was  $2.94 \pm 0.52$  mm and the PHS  $2.95 \pm 0.55$  mm and the Bland–Altman plots showed low bias ( $-0.01$ ) and limits of agreement ( $-0.79 - 0.76$ ) between the methods with (Figure 5.2).

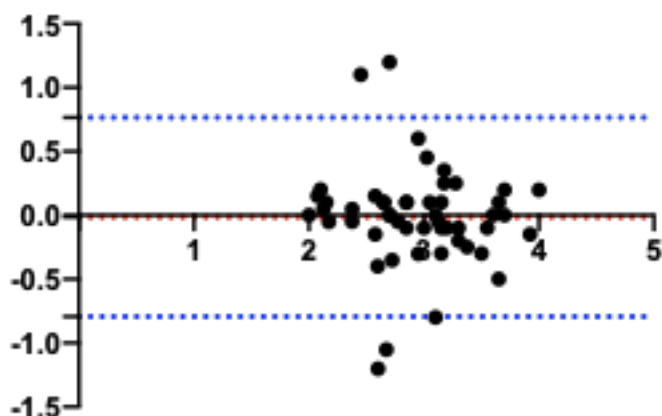


*FIGURE 5.2 Bland-Altman plot comparing measurements of the pituitary gland height measured in the transverse (PHT) and sagittal (PHS) plane. The y-axis shows the difference between the two measurements, and the x-axis shows the average. The blue dotted lines represent the 95% confidence intervals, and the red dotted line represents the bias.*

All the measurements described resulted normally distributed, and no outliers were detected in any of them. The reference intervals, mean  $\pm$  standard deviation and range (minimum to maximum) for linear measurements and P:B ratio are reported in Table 5.4.

Measurement	Mean $\pm$ SD	Range (Min – Max)	Lower limit (90% CI)	Upper limit (90% CI)
PHT (mm)	2.94 $\pm$ 0.52	2.0 – 4.1	1.88 (1.68 – 2.10)	4.01 (3.81 – 4.20)
PHS (mm)	2.95 $\pm$ 0.55	1.9 – 4.0	1.84 (1.63 – 2.08)	4.10 (3.89 – 4.27)
PL (mm)	3.17 $\pm$ 0.52	2.0 – 4.4	2.13 (1.92 – 2.37)	4.23 (4.03 – 4.42)
PW (mm)	3.24 $\pm$ 0.61	2.1 – 4.8	1.92 (1.66 – 2.15)	4.41 (4.12 – 4.71)
BA (mm <sup>2</sup> )	789.02 $\pm$ 61.85	647.87 – 962.85	659.51 (634.51 – 687.61)	910.96 (883 – 938.01)
P:B ratio	0.37 $\pm$ 0.06	0.25 – 0.48	0.25 (0.23 – 0.28)	0.49 (0.47 – 0.51)

TABLE 5.4 Mean  $\pm$  standard deviation, upper and lower limits of the reference value (and corresponding 90% CI) of the pituitary gland linear measurements, brain area and pituitary-to-brain ratio. Abbreviations. CI, confidence interval; BA, brain area; Max, maximum; Min, minimum; P:B ratio, pituitary gland height to brain area ratio; PHS, maximal pituitary height on the sagittal plane; PHT, maximal pituitary height on the transverse plane; PL: pituitary length; PW: pituitary width; SD, standard deviation.

## 5.5 DISCUSSION

The primary aim of the study was to evaluate the linear pituitary dimensions, P:B ratio and to establish the normal reference range values in DSH cat. Secondary objectives were to evaluate the influence of age, body weight and sex on those measurements and evaluate the intra- and inter-observer agreement. Pituitary dimensions and, consequently, the P:B ratio assessed by CT can vary widely in DSH cat. Measurements had a moderate/good inter-observer agreement, while the intra-observer agreement was good/excellent for the most experienced (observer 1). All the linear measurements had negligible/low correlation with body weight, and only PHS and PL had a low correlation with age. Results of the ICC for the intra-observer agreement suggest that it was influenced mainly by the experience of the operator; indeed, observer 1, considered the most experienced, showed good reliability and, except for PL and BA, higher ICC values compared to observer 2. The ICC for inter-observer agreement revealed a moderate/good agreement between observers. In a previous study<sup>20</sup> assessing the intra- and interobserver agreement accuracy and reproducibility of CT measurements of the pituitary gland in dogs on a phantom model, the authors found an excellent level of agreement for PH and P:B ratio between the observers. However, a systematic and significant difference was present between them. The authors concluded that due to this systematic variation, intra- and inter-patient comparisons have to be performed preferably by the same observer. In a previous study, Van Hoe *et al.*<sup>21</sup> suggested a fundamental role of image windowing in the manual measurement of small parts. Accordingly, the

moderate agreement between observers in the current study may mainly rely on the operator's experience level and ability to obtain the best window levels and width to measure the pituitary gland. The ICC results for BA indirectly support this hypothesis. Indeed, the BA was the measurement with the higher level of agreement between observers and is probably related to the automated segmentation tool used for obtaining it that makes the measurement not operator dependent. The Bland-Altman plot showed minimal bias (- 0.01) between PHT and PHS. Therefore, both methods can be used to determine the pituitary height. However, in the authors opinion, the determination of the pituitary height is easier with PHT than PHS, due to the oblique position of the pituitary gland in some cats. On the other hand, on the sagittal MPR, it is possible measure the PHS and PL in a single image. In a previous study<sup>12</sup> performed on fifteen cats, of which ten were DSH, the authors found a significant correlation between pituitary dimensions and body weight. However, the correlation between those variables was not reported. Additionally, considering only the DSH cats, the authors reported a significant difference between those weighing < 3 kg and those above this value. In our study, although body weight was positively correlated with all pituitary dimensions, the degree of correlation was negligible/low. Therefore, an actual effect of body weight on pituitary dimensions is doubtful as reported by other studies.<sup>11,14</sup> In the current study, we decided to include also skeletally immature cats since in humans is well-known the progressive growth of the pituitary gland during puberty<sup>22, 23</sup> and the small size of the pituitary gland in elderly people.<sup>24</sup> Similarly, Häußler *et al.*<sup>14</sup> found a positive correlation between age

and pituitary height, width and length in a sample of brachycephalic cats with 25% of them with less than 15 months, while this correlation was not performed in the mesaticephalic group. In our sample of mesaticephalic cats, age was weakly correlated with PHS and PL. Consequently, a significant influence of age on pituitary dimensions is unlikely. No correlation was found between gender and pituitary dimensions. This finding agrees with a previous study<sup>12</sup> but partially disagrees with the study from Häußler *et al.*<sup>14</sup> where male cats had larger pituitary width. A bias in our study may have been introduced by the high number of neutered females constituting more than half of the whole group. Further studies with homogeneous gender groups are needed to clarify the incidence of gender and neutering on the pituitary gland.

This is the first study where reference values for the pituitary linear dimensions and P:B ratio were established according to the guidelines of the ASVCP.<sup>18</sup> The obtained values are wider and partly differ from those already reported in the literature.<sup>11-14</sup> This discrepancy can be mainly related to the larger sample size, which tends to be more representative of the actual DSH cat population, including a few healthy cats with pituitary sizes at the extremes of the reference interval. Another possible cause may be related to the deployment of different CT units. In the current study and differently from the previous, all the CT studies were performed using a MDCT unit providing high spatial resolution and real isotropic images. These, technical aspect facilitated the use of MPR and allows precise assessment of the pituitary gland.<sup>25</sup> Finally, a further cause of divergence may be related to the different experiences of the observers. The main limitation of this study is the absence of IGF-1 assay in cats

included in the final sample. Consequently, it is impossible to exclude acromegaly categorically. However, none of the subjects had clinical, CT or laboratory findings consistent with acromegaly or diabetes mellitus. Given the small number of laboratories that perform this analysis and the relatively high cost, the assay for IGF-1 is not performed as part of the routine serum analysis panel in our institution as it is reserved for cats with clinical suspicion of acromegaly. Another limitation is the absence of necropsy and, therefore, the possibility of categorically ruling out pituitary lesions and verifying the degree of agreement between the actual measurements of the pituitary gland and those obtained by CT. In conclusion, this study provides reference values for pituitary dimensions and P:B ratio in DSH cats. The reference values are wider than the mean values previously reported. Pituitary linear dimensions and P:B ratio exhibit a good intra-operator agreement but a moderate inter-operator agreement, likely consequent to the millimetric dimensions of the gland. Software that automatically defines the structures of interest may help reduce this operator-related variability. In the sample analysed, although significant correlations were found between body weight and pituitary size and between age and pituitary height and length, the actual effect of these variables on the pituitary gland remains questionable. In addition, no differences between genders were found. According to this study, pituitary gland with PHT > 4mm or a P:B ratio > 0.49 have to be considered enlarged. The reference ranges obtained from this study may help assess pituitary size in cats with suspected neoplastic lesions affecting the pituitary gland in surgical or radiation therapy planning and monitoring response to treatment.

## 5.6 REFERENCES

1. Davis SW, Ellsworth BS, Pérez Millan MI, Gergics P, Schade V, Foyouzi N, et al. Pituitary gland development and disease: from stem cell to hormone production. *Curr Top Dev Biol.* 2013;**106**: 1-47. 10.1016/b978-0-12-416021-7.00001-8
2. Lunn KF, Boston SE. 26 - Tumors of the Endocrine System. In: Vail DM, Thamm DH, Liptak JM (eds): *Withrow and MacEwen's Small Animal Clinical Oncology (Sixth Edition)*. St. Louis (MO): W.B. Saunders, 2020;565-596.
3. Owen TJ, Martin LG, Chen AV. Transsphenoidal Surgery for Pituitary Tumors and Other Sellar Masses. *Veterinary Clinics of North America: Small Animal Practice.* 2018;**48**: 129-151. <https://doi.org/10.1016/j.cvsm.2017.08.006>
4. Lopes MBS. The 2017 World Health Organization classification of tumors of the pituitary gland: a summary. *Acta Neuropathologica.* 2017;**134**: 521-535. 10.1007/s00401-017-1769-8
5. Sanders K, Galac S, Meij BP. Pituitary tumour types in dogs and cats. *Vet J.* 2021;**270**: 105623. 10.1016/j.tvjl.2021.105623

6. Reusch CE. Chapter 2 - Disorders of Growth Hormone. In: Feldman EC, Nelson RW, Reusch CE, Scott-Moncrieff JCR (eds): *Canine and Feline Endocrinology (Fourth Edition)*. St. Louis: W.B. Saunders, 2015;37-76.
7. Gunn-Moore D. Feline endocrinopathies. *Veterinary Clinics of North America: Small Animal Practice*. 2005;**35**: 171-210.  
<https://doi.org/10.1016/j.cvsm.2004.09.002>
8. Niessen SJM, Forcada Y, Mantis P, Lamb CR, Harrington N, Fowkes R, et al. Studying Cat (*Felis catus*) Diabetes: Beware of the Acromegalic Imposter. *PLOS ONE*. 2015;**10**: e0127794.  
10.1371/journal.pone.0127794
9. Holmes SP. Imaging the Feline Neurologic System. *Feline Diagnostic Imaging*, 2020;77-111.
10. Hecht S, Schwarz T. Pituitary Gland. *Veterinary Computed Tomography*, 2011;197-203.
11. Wallack ST, Wisner ER, Feldman EC. Mensuration of the pituitary gland from magnetic resonance images in 17 cats. *Vet Radiol Ultrasound*. 2003;**44**: 278-282. 10.1111/j.1740-8261.2003.tb00455.x

12. Nadimi S, Molazem M, Jarolmasjed S, Esmaili Nejad MR. Volumetric evaluation of pituitary gland in dog and cat using computed tomography. *Vet Res Forum*. 2018;**9**: 337-341. 10.30466/vrf.2018.33073
13. Tyson R, Graham JP, Bermingham E, Randall S, Berry CR. Dynamic computed tomography of the normal feline hypophysis cerebri (Glandula pituitaria). *Vet Radiol Ultrasound*. 2005;**46**: 33-38. 10.1111/j.1740-8261.2005.00006.x
14. Häußler TC, von Pückler KH, Thiel C, Enderlein S, Failing K, Ondreka N, et al. Measurement of the normal feline pituitary gland in brachycephalic and mesocephalic cats. *J Feline Med Surg*. 2018;**20**: 578-586. 10.1177/1098612x17723774
15. Kooistra HS, Voorhout G, Mol JA, Rijnberk A. Correlation between impairment of glucocorticoid feedback and the size of the pituitary gland in dogs with pituitary-dependent hyperadrenocorticism. *J Endocrinol*. 1997;**152**: 387-394. 10.1677/joe.0.1520387
16. Irving McGrath J, Zhang W, Hollar R, Collings A, Powell R, Foale RD, et al. More Than a Moggy; A Population Genetics Analysis of the United Kingdom's Non-Pedigree Cats. *Genes (Basel)*. 2021;**12**. 10.3390/genes12101619

17. Koo TK, Li MY. A Guideline of Selecting and Reporting Intraclass Correlation Coefficients for Reliability Research. *J Chiropr Med.* 2016;**15**: 155-163. 10.1016/j.jcm.2016.02.012
18. Friedrichs KR, Harr KE, Freeman KP, Szladovits B, Walton RM, Barnhart KF, et al. ASVCP reference interval guidelines: determination of de novo reference intervals in veterinary species and other related topics. *Vet Clin Pathol.* 2012;**41**: 441-453. 10.1111/vcp.12006
19. Reed AH, Henry RJ, Mason WB. Influence of statistical method used on the resulting estimate of normal range. *Clin Chem.* 1971;**17**: 275-284.
20. van der Vlugt-Meijer RH, Meij BP, Voorhout G. Intraobserver and interobserver agreement, reproducibility, and accuracy of computed tomographic measurements of pituitary gland dimensions in healthy dogs. *Am J Vet Res.* 2006;**67**: 1750-1755. 10.2460/ajvr.67.10.1750
21. Van Hoe L, Haven F, Bellon E, Baert AL, Bosmans H, Feron M, et al. Factors influencing the accuracy of volume measurements in spiral CT: a phantom study. *J Comput Assist Tomogr.* 1997;**21**: 332-338. 10.1097/00004728-199703000-00034

22. Argyropoulou M, Perignon F, Brunelle F, Brauner R, Rappaport R. Height of normal pituitary gland as a function of age evaluated by magnetic resonance imaging in children. *Pediatric Radiology*. 1991;**21**: 247-249.  
10.1007/BF02018614
23. Sari S, Sari E, Akgun V, Ozcan E, Ince S, Saldir M, et al. Measures of pituitary gland and stalk: from neonate to adolescence. *Journal of Pediatric Endocrinology and Metabolism*. 2014;**27**: 1071-1076.  
doi:10.1515/jpem-2014-0054
24. Lurie SN, Doraiswamy PM, Husain MM, Boyko OB, Ellinwood EH, Jr., Figiel GS, et al. In vivo assessment of pituitary gland volume with magnetic resonance imaging: the effect of age. *J Clin Endocrinol Metab*. 1990;**71**: 505-508. 10.1210/jcem-71-2-505
25. Schwarz T, O'Brien R. CT Acquisition Principles. *Veterinary Computed Tomography*, 2011;9-27.

## Chapter VI

### The heart-to-single vertebra ratio: A new objective method for radiographic assessment of cardiac silhouette size in dogs

Dario Costanza, Adelaide Greco, Diego Piantedosi, Dario Bruzzese, Maria Pia Pasolini, Pierpaolo Coluccia, Erica Castiello, Cláudia Sofia Baptista, Leonardo Meomartino

Vet Radiol Ultrasound. 2022 Dec 8. doi: 10.1111/vru.13201. Online ahead of print.

## 6.1 ABSTRACT

Vertebral heart size (VHS) is widely determined in clinical practice as an objective method to assess the cardiac silhouette dimensions. However, a key limitation is that it is impossible to determine VHS in dogs with vertebral alterations. This retrospective, method comparison, observer agreement study sought to overcome this limitation by using the heart to single vertebra ratio (HSVR), by evaluating the level of agreement between VHS and HSVR, as well as the intra- and inter-observer agreement for HSVR. Three independent observers retrospectively evaluated thoracic radiographs obtained over a set time-period. Exclusion criteria were the presence of alterations of the thoracic spine and the inability to clearly outline the cardiac silhouette. The lengths of the vertebral bodies, from the fourth to eighth thoracic vertebra, and VHS were measured on each radiograph. The HSVR was calculated by dividing the sum of the cardiac long and short axes by the length of each vertebral body. Eighty dogs of different breeds were included in the final analysis. Lin's concordance correlation coefficients revealed strong correlations between VHS and HSVR (0.91–0.96), and the Bland–Altman plots showed low bias (0.01–0.2) between the methods. The mean absolute errors indicated low average magnitudes of error (0.11–0.28). The intraclass correlation coefficients showed good to excellent inter-observer (0.87–0.92;  $P = 0.000$ ) and intra-observer (0.87–0.99;  $P < .001$ ) agreement. In the authors' opinion, this new method, which is less time consuming and more objective, could offer a valuable alternative to VHS.

## 6.2 INTRODUCTION

Although echocardiography is considered the gold standard modality for studying the heart, radiography plays a fundamental role in assessing the size of the cardiac silhouette and ruling out the presence of concomitant pulmonary disorders such as vascular congestion, pulmonary oedema, and pneumonia.<sup>1</sup> However, radiographic assessment of the cardiac silhouette dimensions is not always straightforward and is quite subjective; indeed, variations may occur owing to different inherent conformations of the thorax among different canine morphotypes.<sup>2</sup> Over the years, several methods have been proposed to objectively determine the dimensions of the cardiac silhouette.<sup>3-5</sup> However, these methods are not widely used in clinical practice because of their limitations, including variations in cardiac silhouette inclination, thoracic conformation, the breathing phase in which the radiograph is acquired, difficulty in correctly positioning the patient, the presence of concurrent lung pathologies that alter the cardiothoracic ratio, and the inaccuracy of determining the anatomical landmarks used for measurements.<sup>4, 6, 7</sup> In 1995, Buchanan and Bücheler described the vertebral heart score (VHS) as an objective method for assessing heart size.<sup>8</sup> Since then, a number of studies have evaluated its reliability by assessing the intra- and inter-observer agreement, the effects of sex, breathing, cardiac cycle, body condition score, and recumbency on the measurements, and determined indices for individual breeds that tend to deviate from the initially reported cut-off values.<sup>9-25</sup> VHS is very useful in clinical practice because it is relatively simple to determine at initial and follow-up examinations.<sup>19, 26, 27</sup> However, some limitations exist, including the difficulty of determining VHS in patients with *spondylosis deformans*,

reduced intervertebral disc spaces, or vertebral malformations such as hemivertebrae, butterfly vertebrae or wedge vertebrae. Of note, vertebral abnormalities artifactually increase VHS.<sup>11, 24</sup> We hypothesised that a single vertebra preserves its proportion to the respect of the whole body as well as the thoracic vertebral tract proposed by Buchanan and Bucheler.<sup>8</sup> The use of a single vertebra, without shape and dimensions alterations, could allow the clinician to objectively evaluate cardiac silhouette dimensions, even in patients with thoracic spine alterations. Therefore, the primary aim of this study was to develop a novel method, termed the heart to single vertebra ratio (HSVR). Secondary objectives were to test the level of agreement between the newly described method and VHS, and to evaluate the intra- and inter-observer agreement among three observers with different levels of experience.

### 6.3 MATERIALS AND METHODS

The single-centre, retrospective, method comparison, observer agreement study was approved by the Clinical Ethical Review Board of the University of Naples “Federico II” (PG/2022/0062754). The electronic records of canine patients referred to the Interdepartmental Centre of Veterinary Radiology of the University of Naples ‘Federico II’ in the set study period between September 2018 and January 2021 were retrieved from the picture archiving and communication system (dcm4chee-arc-light version 5.11.1, <http://www.dcm4chee.org>) and the images were reviewed. Radiography was performed for various reasons, including cardiologic screening, pre-anaesthetic evaluation, and exclusion of metastases. All radiographic examinations were obtained on awake, unседated patients during inspiration and used a computed radiography system (Agfa CR-30, Agfa HealthCare, Mortsel, Belgium) equipped with a focused Potter–Bucky grid and a focus-to-film distance of 100 cm. The dogs were restrained manually or with sandbags, attempting to avoid spinal or heart mispositioning that could cause geometric distortions or make it difficult to correctly visualise the anatomical landmarks. All radiographic examinations included at least the right-lateral view, which was used to assess the heart dimensions. Exclusion criteria were as follows: (a) presence of alterations affecting the thoracic spine (e.g., hemivertebrae, butterfly vertebrae, spondylitis, *spondylosis deformans*, kyphosis, or reduced intervertebral disc space); (b) inability to correctly visualise the cardiac silhouette (e.g., pleural effusion, right middle lung lobe increased opacity, cardiac neoplasm, or mediastinal masses); (c) positioning or technical errors (e.g., overexposure, underexposure, or motion artefacts); and (d) skeletal immaturity.

The breed, sex, weight (in kilograms), and age (in years) were recorded for each dog. The decisions on whether to include or exclude radiographs were made by one author (D.C), a second-year Ph.D. student in diagnostic imaging. All the selected radiographs, in DICOM format, were anonymized by the same author before submitting them to three observers to assess the inter-observer agreement. One month later, the same author randomly selected from the same set of radiographs a smaller sample using the ‘randbetween’ tool (Microsoft Excel version 16.52 2021, Microsoft Corp., Redmond, WA, USA) to assess the intra-observer agreement among the three observers. All radiographic measurements were performed using the right-lateral view by three independent operators with different levels of experience using the ‘line’ function in an open-source DICOM viewer (Horos version 3.3.6, 64-bit, Nimble Co LLC d/b/a Purview, Annapolis, MD, USA, <https://www.horosproject.org>) on the same workstation (iMac 5K, 27-inch, Apple Inc., Cupertino CA, USA). Observers 1 (L.M) and 2 (A.G) are professors of veterinary radiology with a Ph.D. and >25 and >10 years of experience, respectively. Observer 3 (D.P) is a professor of cardiology with a Ph.D. and >15 years of experience. All the observers were blind regarding the clinical data and reasons for thoracic radiography. All measurements were performed one time by each observer, independently and blinded to the results reported by the other observers by following the same oral and written instructions provided in a portable document format file. First, the length of the vertebral body of the fourth (T4), fifth (T5), sixth (T6), seventh (T7), and eighth (T8) thoracic vertebrae, including the respective caudal intervertebral disc space, was measured. Then, the cardiac long axis (LA) and short axis (SA) were measured as described by Buchanan

and Bücheler (Figure 6.1).<sup>8</sup> The LA was defined as the axis traced from the ventral border of the carina (the origin of the left mainstem bronchus) to the cardiac apex, and the SA was defined as the line perpendicular to the LA at the point of the maximum width of the cardiac silhouette. To calculate VHS, the two axes were repositioned over the thoracic vertebrae starting from the cranial endplate of T4. VHS was then expressed as the number of thoracic vertebrae (v) to the nearest 0.1v. Additionally, the sum of the cardiac axes (LA+SA) was divided by the length of the vertebral body, including the respective caudal intervertebral disc space, for T4, T5, T6, T7, and T8 to determine  $HSVR^{T4}$ ,  $HSVR^{T5}$ ,  $HSVR^{T6}$ ,  $HSVR^{T7}$ , and  $HSVR^{T8}$ , respectively.

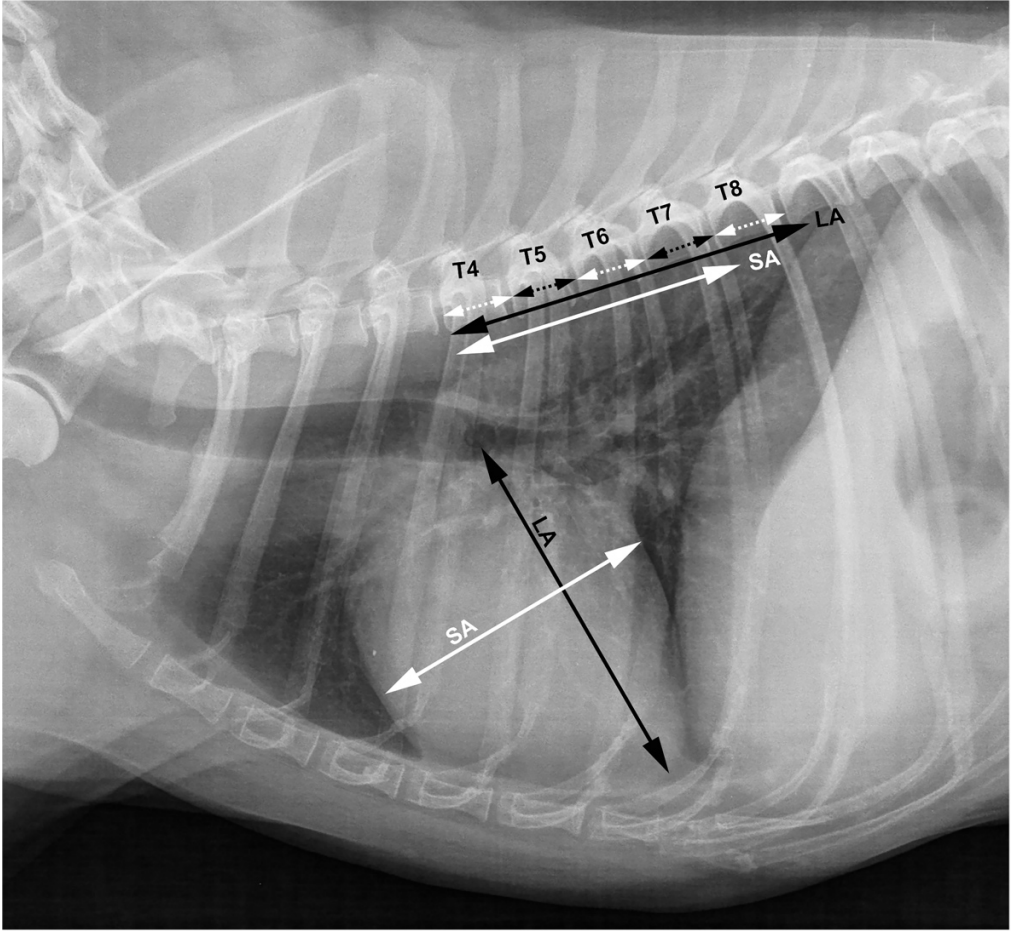


*FIGURE 6.7 Representative right lateral thoracic radiographic image (kVp 80; mAs 4) of a mixed-breed dog depicting the measurements of the length of each single vertebral body between T4 and T8, including the corresponding caudal intervertebral disc spaces (black and white dotted arrows labelled T4–T8). The cardiac long axis (LA) and short axis (SA) were measured as described by Buchanan and Bücheler.<sup>8</sup> In this method, the LA (doubled-headed black arrow) was traced from the ventral border of the carina to the cardiac apex and the SA (doubled-headed white arrow) was traced perpendicular to LA at the point of the maximum width of the cardiac silhouette, and then transposed ventral to the column starting from the T4 cranial endplate.*

All data were reported independently by each operator in an electronic spreadsheet (Microsoft Excel version 16.52 2021, Microsoft Corp.). One month later, to assess the degree of intra-observer agreement, the measurements were repeated once, in a single session, independently by each of the three observers on a smaller sample of thirty re-anonymised and re-randomly selected radiographs.

Statistical analyses were performed by one of the authors (D.B. a full professor in biostatistics and epidemiology with a Ph.D. in statistics, biostatistician of the Animal Welfare Committee of the University of Napoli “Federico II”) using open-source statistics software (R version 4.0.1, R Foundation for Statistical Computing, Austria, <https://www.R-project.org>). Descriptive statistics were calculated for age, weight, and breed. Numerical variables were summarized using the median value and range (minimum to maximum). The concordance between the HSVR and VHS values for the 80 radiographs as determined by observer 1, who was considered the most experienced observer, was assessed using Lin’s concordance correlation coefficient (CCC) with the corresponding 95% Confidence Interval (95% CI).<sup>28</sup> The strength of the agreement was scored using the cut-off values proposed by McBride<sup>29</sup> and further analysed using Bland–Altman plots. Error between the VHS and HSVR values was estimated using the mean absolute error (MAE). Intra- and inter-observer agreement was assessed using intraclass correlation coefficients (ICC) and the results were interpreted as suggested by Koo and Li.<sup>30</sup> In all analyses,  $P < .05$  was considered statistically significant.

## 6.4 RESULTS

A total of 300 thoracic radiographic examinations were performed during the time-period. After applying the exclusion criteria, radiographs for 80 dogs (23 intact females, 26 spayed females, 23 intact males, and 8 castrated males) were included in the final sample for assessing the agreement between VHS and HSVR and among the observers. The exposure settings (kilovoltage peak, milliamperere and seconds) varied according to the size of the dog and the body condition score. Reasons for radiographic examination included suspicions of heart disease, and other reasons are summarised in Table 6.1.

Reasons for thoracic radiography for included dogs	n = 80 (%)
Exclusion of metastases	25 (31.25%)
Cardiomyopathies	22 (27,5%)
Cough	16 (20%)
Pre-anaesthetic evaluation	9 (11.25%)
Suspected tracheal collapse	2 (2.5%)
Suspected oesophageal regurgitation	1 (1.25%)
Suspected aspiration pneumonia	1 (1.25%)
Pulmonary hypertension	1 (1.25%)
Systemic thromboembolism	1 (1.25%)
Systemic Leishmaniasis	1 (1.25%)
Dirofilariosis	1 (1.25%)

TABLE 6.8 Reasons for thoracic radiography for included dogs and numbers (%) of dogs in each reason category.

One month later, 30 radiographs, randomly selected from the same set, were used for assessing the intra-observer agreement. The median age was 11 years (range 1–16 years) and the median bodyweight was 10 kg (range 1.3–30.5 kg). The breeds represented were mixed-breed ( $n = 48$ ), Dachshund ( $n = 4$ ), Beagle ( $n = 4$ ), Maltese ( $n = 4$ ), English Cocker spaniel ( $n = 3$ ), Miniature Poodle ( $n = 3$ ), Yorkshire terrier ( $n = 2$ ), Jack Russell terrier ( $n = 2$ ), and one of the each following: Chihuahua, Standard Poodle, Dalmatian, Doberman Pinscher, Labrador Retriever, German Shepherd, Pit bull, Irish Setter, Shih Tzu, and English Springer spaniel. The CCC showed substantial agreement of HSVR<sup>T7</sup> (0.983; 95% CI 0.974–0.989), HSVR<sup>T8</sup> (0.964; 95% CI 0.946–0.977), HSVR<sup>T6</sup> (0.96; 95% CI 0.94–0.973), and HSVR<sup>T5</sup> (0.958; 95% CI 0.936–0.972) with VHS, and moderate agreement of HSVR<sup>T4</sup> with VHS (0.938; 95% CI 0.90–0.95) (Figure 6.2A–E). The Bland–Altman plots for HSVR versus VHS showed a bias of 0.019 for HSVR<sup>T7</sup> ( $\pm 0.18$ ; 95% CI  $-0.34$  to  $0.38$ ), 0.11 for HSVR<sup>T5</sup> ( $\pm 0.27$ ; 95% CI  $-0.42$  to  $0.63$ ),  $-0.13$  for HSVR<sup>T8</sup> ( $\pm 0.22$ ; 95% CI  $-0.57$  to  $0.30$ ), 0.18 for HSVR<sup>T6</sup> ( $\pm 0.21$ ; 95% CI  $-0.24$  to  $0.60$ ), and 0.20 for HSVR<sup>T4</sup> ( $\pm 0.30$ ; 95% CI  $-0.38$  to  $0.70$ ) (Figure 6.2 F–J).

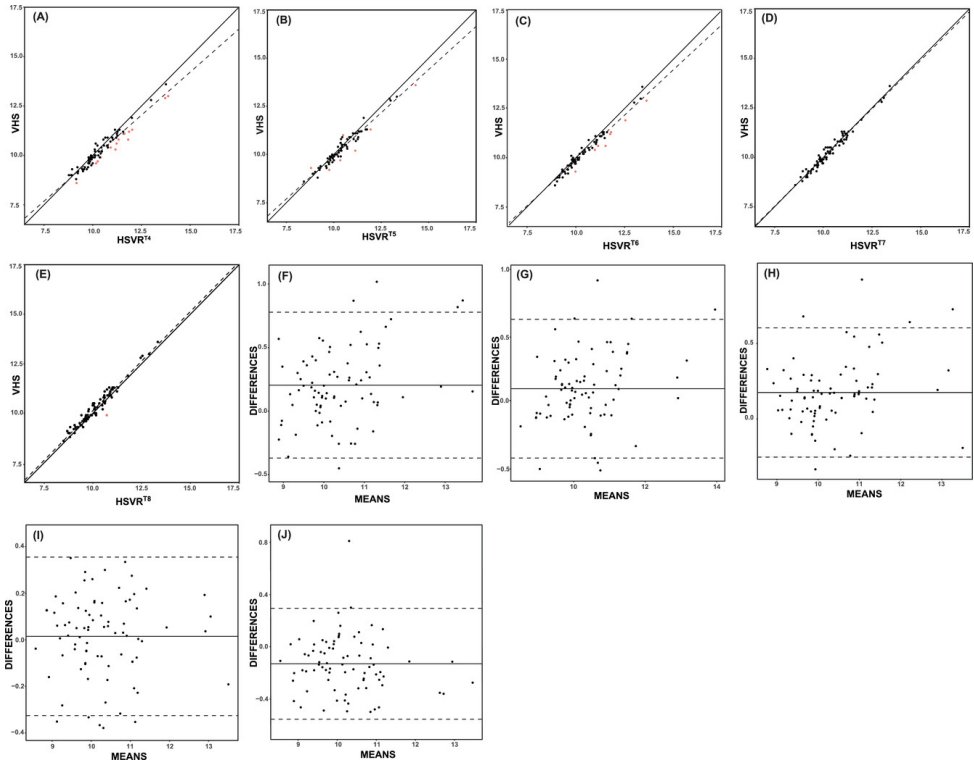


**FIGURE 6.2** Lin's concordance correlation coefficient (CCC) and related Bland–Altman plots. **(A–E)** Lin's CCC comparing VHS with HSVRI determined using T4 **(A)**, T5 **(B)**, T6 **(C)**, T7 **(D)** and T8 **(E)**. The y axes show the VHS index, and the x axes show the HSVR. The continuous lines represent the lines of perfect agreement (i.e. the ideal condition where HSVR equals VHS), the dashed lines represent the estimated least squares lines, and the red dots represent outliers. **(F–J)** Bland–Altman plots comparing VHS with HSVR obtained using T4 **(F)**, T5 **(G)**, T6 **(H)**, T7 **(I)** and T8 **(J)**. The x axes show the mean of both measurements, the y axes show the difference between the two measurements, the dashed lines represent the 95% confidence intervals, and the continuous lines represent the bias.

The MAE for the comparison between HSVR and VHS was lowest for HSVR<sup>T7</sup> (0.14; 95% CI 0.12–0.16) followed by HSVR<sup>T8</sup> (0.20; 95% CI 0.16–0.23), HSVR<sup>T6</sup> (0.22; 95% CI 0.18–0.26), HSVR<sup>T5</sup> (0.22; 95% CI 0.23–0.33), and HSVR<sup>T4</sup> (0.28; 95% CI 0.23–0.33). The ICC showed good to excellent inter-observer (Table 6.2;  $P = .000$ ) and intra-observer (Table 6.3;  $P < .001$ ) agreement for all measurements.

	ICC (n = 80)	
		95% CI
VHS	0.92	0.86–0.95
HSVR <sup>T4</sup>	0.88	0.82–0.92
HSVR <sup>T5</sup>	0.90	0.86–0.93
HSVR <sup>T6</sup>	0.88	0.81–0.92
HSVR <sup>T7</sup>	0.87	0.81–0.92
HSVR <sup>T8</sup>	0.89	0.85–0.93

TABLE 6.2 Intraclass correlation coefficients for inter-observer agreement among the three observers.

Abbreviations: CI, confidence interval; ICC, intraclass correlation coefficient; HSVR<sup>T4</sup>, heart to single vertebra ratio determined using the fourth thoracic vertebra; HSVR<sup>T5</sup>, heart to single vertebra ratio determined using the fifth thoracic vertebra; HSVR<sup>T6</sup>, heart to single vertebra ratio determined using the sixth thoracic vertebra; HSVR<sup>T7</sup>, heart to single vertebra ratio determined using the seventh thoracic vertebra; HSVR<sup>T8</sup>, heart to single vertebra ratio determined using the eighth thoracic vertebra; VHS, vertebral heart size index

	ICC (95% CI)		
	(n = 30)		
	Observer 1	Observer 2	Observer 3
VHS	0.96 (0.93–0.98)	0.96 (0.93–0.98)	0.93 (0.87–0.96)
HSVR <sup>T4</sup>	0.98 (0.97–0.99)	0.95 (0.90–0.97)	0.92 (0.85–0.95)
HSVR <sup>T5</sup>	0.98 (0.96–0.99)	0.96 (0.92–0.98)	0.90 (0.83–0.95)
HSVR <sup>T6</sup>	0.88 (0.78–0.93)	0.95 (0.91–0.97)	0.92 (0.85–0.95)
HSVR <sup>T7</sup>	0.99 (0.97–0.99)	0.88 (0.79–0.94)	0.90 (0.82–0.95)
HSVR <sup>T8</sup>	0.97 (0.94–0.98)	0.87 (0.78–0.93)	0.94 (0.89–0.97)

TABLE 6.3 Intraclass correlation coefficients for intra-observer agreement between the three observers. Abbreviations: CI, confidence interval; ICC, intraclass correlation coefficient; HSVRT<sup>4</sup>, heart to single vertebra ratio determined using the fourth thoracic vertebra; HSVRT<sup>5</sup>, heart to single vertebra ratio determined using the fifth thoracic vertebra; HSVRT<sup>6</sup>, heart to single vertebra ratio determined using the sixth thoracic vertebra; HSVRT<sup>7</sup>, heart to single vertebra ratio determined using the seventh thoracic vertebra; HSVRT<sup>8</sup>, heart to single vertebra ratio determined using the eighth thoracic vertebra; VHS, vertebral heart size index

## 6.5 DISCUSSION

The primary aim of this study was to describe a new objective method for radiographic assessment of cardiac silhouette dimensions in patients where VHS cannot be determined owing to alterations affecting the thoracic vertebral bodies or intervertebral disc spaces. The secondary aims of the study were to assess the level of agreement between the new method and VHS, including intra- and inter-observer agreement. Findings from our study supported our hypotheses. The HSVR is a simple, quick and reliable method with an excellent agreement with the VHS and substantial intra- and inter-observer agreement. Congenital alterations of the thoracic spine, of uncertain clinical relevance, are present in many dogs, particularly brachycephalic breeds,<sup>31</sup> and this means it is impossible to correctly determine VHS.<sup>11</sup> Similarly, acquired spinal alterations (e.g. severe *spondylosis deformans*) tend to worsen with age and make VHS unreliable for follow-up of the cardiac silhouette in the same patient. Eventually, these alterations hinder the ability to predict the onset of potentially serious disorders such as pulmonary oedema.<sup>26, 27, 32</sup> Determining HSVR by comparing the cardiac axes with a single thoracic vertebra overcomes this intrinsic limitation of VHS and represents a more objective evaluation of cardiac silhouette dimensions, even in patients with alterations involving some thoracic vertebrae between T4 and T8. In the present study, we decided to calculate the VHS and vertebral length, including the respective caudal intervertebral disc space, since its absence would have led to an overestimation of HSVR when compared to VHS. Indeed, multiple intervertebral disc spaces are implicitly included when the cardiac LA and

SA are transposed over the spine for VHS estimation. Finally, not considering the intervertebral disc space in determining the VHS will lead to erroneously obtain the same VHS value when the transposed cardiac axis reaches either the caudal endplate of one vertebra or the cranial endplate of the following vertebra.<sup>22</sup> In the present analyses, HSVRT<sup>7</sup> showed substantial agreement with VHS, together with low bias and mean error between the methods. The results of the present analyses also indicate that, when it is not possible to determine HSVRT<sup>7</sup>, it is possible to use the other ratios in the following order of preference: HSVRT<sup>8</sup>, HSVRT<sup>5</sup>, and HSVRT<sup>6</sup>. Although these indices showed slightly lower agreement with VHS than did HSVRT<sup>7</sup>, they still showed substantial agreement and low bias. Of the five ratios evaluated, HSVRT<sup>4</sup> is perhaps least favourable because it showed the lowest, although still acceptable, level of agreement with VHS and relatively higher bias compared with HSVR calculated using the other thoracic vertebrae. The method's reliability is also supported by the high correlation between VHS and HSVR despite the broad heterogeneity of the study sample, which mostly comprised mixed-breed dogs and a variety of pure-breed dogs of different sizes and thoracic conformations. Furthermore, the presence or absence of an underlying cardiac disease was not considered in order to increase the randomness of the sample, making it more representative of the dog population in clinical settings. The good to excellent inter- and intra-observer agreement confirms the reliability of this new method, probably due to the easier method of calculating the cardiac silhouette dimensions in vertebral units and the clear anatomical landmarks. In fact, as previously described, the inter- and intra-observer agreement for VHS is related to individual variations in the identification of the anatomical

landmarks used to track the cardiac axes and converting the length of the cardiac axes into vertebral units.<sup>14, 15, 17, 19, 22, 23, 25, 27, 33</sup> Similar to the objective VHS proposed by Sánchez *et al.*,<sup>33</sup> the cardiac axes measured for HSVR are normalised for the vertebral length without transposing the cardiac axes over the thoracic spine and without the need to span the conversion of the cardiac axis in vertebral units, thus reducing the method's susceptibility to differing inter-observer interpretation.<sup>12, 22</sup> In this way, it is possible to avoid some of the limiting factors, such as inter-observer variation in the interpretation of VHS, and may allow more objective evaluation of cardiac silhouette dimensions.<sup>22, 33</sup> However, unlike the above-mentioned objective VHS, HSVR is determined using a single vertebral body rather than the entire T4–T8 distance. Therefore, HSVR is suitable for the objective evaluation of cardiac dimensions in patients with thoracic spine alterations. Furthermore, HSVR is quicker and easier to determine than VHS because it is not necessary to transpose the cardiac axes on the thoracic spine. These advantages of HSVR could increase the clinical applications of quantitative radiographic evaluation of the cardiac silhouette, which is difficult to interpret, and may reduce the risk of erroneous subjective interpretation.<sup>33</sup> Some limitations of this study include the following: the relatively high experience of the three observers. Although previous studies of VHS have demonstrated that the difference between observers is more strongly linked to identification of the anatomic landmarks than to the observer's experience,<sup>14, 15, 17, 19, 22, 23, 25, 27, 33</sup> further studies involving inexperienced observers would be useful to verify its use. Another possible limitation of the HSVR is the need to use breed-specific cut-off values, the same as VHS, because there is intrinsic variability in the

ratio between the heart size and vertebral body length among different breeds. In conclusion, HSVR is a simple and reliable modality for assessing the cardiac silhouette size in dogs with thoracic spine alterations. Given the simplicity of determining HSVR, as there is no need to transpose the cardiac axes on the thoracic spine, non-specialists could benefit more than radiologists in using this method.

## 6.6 REFERENCES

1. Bahr R. Chapter 35 - Canine and Feline Cardiovascular System. In: Thrall DE (ed): Textbook of Veterinary Diagnostic Radiology (Seventh Edition): W.B. Saunders, 2018;684-709. <https://doi.org/10.1016/B978-0-323-48247-9.00047-4>
2. Adams W.H.; Hecht S. Heart and great vessels. In: Hecht S (ed): Diagnostic Radiology in Small Animal Practice. Great Easton, Essex, United Kingdom.: 5m Books, 2020;155-175.
3. Hamlin RL. Analysis of the cardiac silhouette in dorsoventral radiographs from dogs with heart disease. J Am Vet Med Assoc. 1968;153: 1446-1460.
4. Suter PF, Lord PF. Cardiac Diseases. In: Suter PF (ed): Thoracic Radiography: A Text Atlas of Thoracic Diseases of the Dog and Cat. Wettswil, Switzerland: Peter F. Suter, 1984;351 - 516.
5. Toombs JP, Ogburn PN. Evaluating canine cardiovascular silhouettes: radiographic methods and normal radiographic anatomy. Compendium on Continuing Education for the Practicing Veterinarian. 1985;7: 579-587.

6. Holmes RA, Smith FG, Lewis RE, Kern DM. The effects of rotation on the radiographic appearance of the canine cardiac silhouette in dorsal recumbency. *Veterinary Radiology*. 1985;26: 98-101. <https://doi.org/10.1111/j.1740-8261.1985.tb01390.x>
7. Silverman S, Suter PF. Influence of inspiration and expiration on canine thoracic radiographs. *J Am Vet Med Assoc*. 1975;166: 502-510.
8. Buchanan JW, Bücheler J. Vertebral scale system to measure canine heart size in radiographs. *J Am Vet Med Assoc*. 1995;206: 194-199.
9. Greco A, Meomartino L, Raiano V, Fatone G, Brunetti A. Effect of left vs. right recumbency on the vertebral heart score in normal dogs. *Vet Radiol Ultrasound*. 2008;49: 454-455. <https://doi.org/10.1111/j.1740-8261.2008.00406.x>
10. Bavegems V, Van Caelenberg A, Duchateau L, Sys SU, Van Bree H, De Rick A. Vertebral heart size ranges specific for whippets. *Vet Radiol Ultrasound*. 2005;46: 400-403. <https://doi.org/10.1111/j.1740-8261.2005.00073.x>
11. Jepsen-Grant K, Pollard RE, Johnson LR. Vertebral heart scores in eight dog breeds. *Vet Radiol Ultrasound*. 2013;54: 3-8. <https://doi.org/10.1111/j.1740-8261.2012.01976.x>
12. Lamb CR, Wikeley H, Boswood A, Pfeiffer DU. Use of breed-specific ranges for the vertebral heart scale as an aid to the radiographic

diagnosis of cardiac disease in dogs. *Vet Rec.* 2001;148: 707-711.

<https://doi.org/10.1136/vr.148.23.707>

13. Puccinelli C, Citi S, Vezzosi T, Garibaldi S, Tognetti R. A radiographic study of breed-specific vertebral heart score and vertebral left atrial size in Chihuahuas. *Vet Radiol Ultrasound.* 2021;62: 20-26.

<https://doi.org/10.1111/vru.12919>

14. Luciani MG, Withoef JA, Mondardo Cardoso Pissetti H, Pasini de Souza L, Silvestre Sombrio M, Bach EC, et al. Vertebral heart size in healthy Australian cattle dog. *Anat Histol Embryol.* 2019;48: 264-267.

<https://doi.org/10.1111/ahe.12434>

15. Birks R, Fine DM, Leach SB, Clay SE, Eason BD, Britt LG, et al. Breed-Specific Vertebral Heart Scale for the Dachshund. *J Am Anim Hosp Assoc.* 2017;53: 73-79. <https://doi.org/10.5326/jaaha-ms-6474>

16. Marin LM, Brown J, McBrien C, Baumwart R, Samii VF, Couto CG. Vertebral heart size in retired racing Greyhounds. *Vet Radiol Ultrasound.* 2007;48: 332-334. <https://doi.org/10.1111/j.1740-8261.2007.00252.x>

17. Baisan RA, Vulpe V. Vertebral heart size and vertebral left atrial size reference ranges in healthy Maltese dogs. *Vet Radiol Ultrasound.* 2021.

<https://doi.org/10.1111/vru.13027>

18. Kraetschmer S, Ludwig K, Meneses F, Nolte I, Simon D. Vertebral heart scale in the beagle dog. *J Small Anim Pract.* 2008;49: 240-243. <https://doi.org/10.1111/j.1748-5827.2007.00531.x>
19. Taylor CJ, Simon BT, Stanley BJ, Lai GP, Thieman Mankin KM. Norwich terriers possess a greater vertebral heart scale than the canine reference value. *Vet Radiol Ultrasound.* 2020;61: 10-15. <https://doi.org/10.1111/vru.12813>
20. Bodh D, Hoque M, Saxena AC, Gugjoo MB, Bist D, Chaudhary JK. Vertebral scale system to measure heart size in thoracic radiographs of Indian Spitz, Labrador retriever and Mongrel dogs. *Vet World.* 2016;9: 371-376. <https://doi.org/10.14202/vetworld.2016.371-376>
21. Kallassy A, Calendrier E, Bouhsina N, Fusellier M. Vertebral Heart Scale for the Brittany Spaniel: Breed-Specific Range and Its Correlation with Heart Disease Assessed by Clinical and Echocardiographic Findings. *Vet Sci.* 2021;8. <https://doi.org/10.3390/vetsci8120300>
22. Hansson K, Haggstrom J, Kwart C, Lord P. Interobserver variability of vertebral heart size measurements in dogs with normal and enlarged hearts. *Vet Radiol Ultrasound.* 2005;46: 122-130. <https://doi.org/10.1111/j.1740-8261.2005.00024.x>
23. Olive J, Javard R, Specchi S, Bélanger MC, Bélanger C, Beauchamp G, et al. Effect of cardiac and respiratory cycles on vertebral heart score

measured on fluoroscopic images of healthy dogs. *J Am Vet Med Assoc.* 2015;246: 1091-1097. <https://doi.org/10.2460/javma.246.10.1091>

24. Bagardi M, Locatelli C, Manfredi M, Bassi J, Spediacci C, Ghilardi S, et al. Breed-specific vertebral heart score, vertebral left atrial size, and radiographic left atrial dimension in Cavalier King Charles Spaniels: Reference interval study. *Vet Radiol Ultrasound.* 2022;63: 156-163. <https://doi.org/10.1111/vru.13036>

25. Bagardi M, Manfredi M, Zani DD, Brambilla PG, Locatelli C. Interobserver variability of radiographic methods for the evaluation of left atrial size in dogs. *Vet Radiol Ultrasound.* 2021;62: 161-174. <https://doi.org/10.1111/vru.12930>

26. Lord P, Hansson K, Kwart C, Häggström J. Rate of change of heart size before congestive heart failure in dogs with mitral regurgitation. *J Small Anim Pract.* 2010;51: 210-218. <https://doi.org/10.1111/j.1748-5827.2010.00910.x>

27. Lord PF, Hansson K, Carnabuci C, Kwart C, Häggström J. Radiographic heart size and its rate of increase as tests for onset of congestive heart failure in Cavalier King Charles Spaniels with mitral valve regurgitation. *J Vet Intern Med.* 2011;25: 1312-1319. <https://doi.org/10.1111/j.1939-1676.2011.00792.x>

28. Lin LI. A concordance correlation coefficient to evaluate reproducibility. *Biometrics*. 1989;45: 255-268.
29. McBride G. A proposal for strength-of-agreement criteria for Lin's concordance correlation coefficient. NIWA client report: HAM2005-062. 2005;45: 307-310.
30. Koo TK, Li MY. A Guideline of Selecting and Reporting Intraclass Correlation Coefficients for Reliability Research. *J Chiropr Med*. 2016;15: 155-163. <https://doi.org/10.1016/j.jcm.2016.02.012>
31. Ryan R, Gutierrez-Quintana R, Ter Haar G, De Decker S. Prevalence of thoracic vertebral malformations in French bulldogs, Pugs and English bulldogs with and without associated neurological deficits. *Vet J*. 2017;221: 25-29. <https://doi.org/10.1016/j.tvjl.2017.01.018>
32. Reynolds CA, Brown DC, Rush JE, Fox PR, Nguyenba TP, Lehmkuhl LB, et al. Prediction of first onset of congestive heart failure in dogs with degenerative mitral valve disease: the PREDICT cohort study. *J Vet Cardiol*. 2012;14: 193-202. <https://doi.org/10.1016/j.jvc.2012.01.008>
33. Sánchez X, Prandi D, Badiella L, Vázquez A, Llabrés-Díaz F, Bussadori C, et al. A new method of computing the vertebral heart scale by means of direct standardisation. *J Small Anim Pract*. 2012;53: 641-645. <https://doi.org/10.1111/j.1748-5827.2012.01288.x>

## Chapter VII

### Ultrasonographic measurement of kidney-to-aorta parameters in Whippets

Dario Costanza, Maria Pia Pasolini, Adelaide Greco, Giuseppina Mennonna, Luigi Auletta, Francesco Lamagna, Leonardo Meomartino.

Vet Radiol Ultrasound. 2021 Jul;62(4):476-482. doi: 10.1111/vru.12958.

## 7.1 ABSTRACT

In a previous study, an ultrasonographic method to assess kidney size in dogs as a ratio of kidney length to aortic luminal diameter (KL/AoD ratio) was proposed. The main limitation of this method was the wide range of normal values (5.5 – 9.1), which resulted in poor sensitivity and specificity. The aim of this prospective, observational, reference interval study was to determine whether the KL/AoD normal cut-off values in a single breed (Whippets) would have a narrower range than the previously reported normal reference ranges. The influence of sex, age, weight, and side on kidney length (KL) and of sex, age, weight, and scanning plane (longitudinal vs. transversal) on aortic luminal diameter (AoD) were also investigated. Thirty-six clinically healthy Whippets (16 males, 20 females) without ultrasonographic renal lesions were included in this study. The 95% confidence interval of mean KL/AoD was found to be narrower than the previously reported range (i.e. 6.3 – 6.9 versus 5.5 – 9.1). This was considered to be especially notable in that the KL in this breed exhibits marked sexual dimorphism. The KL/AoD ratio did not differ between right versus left sides or male versus female sexes in Whippets ( $p > 0.05$ ). Findings from the current study provided KL/AoD ratio normal reference range cut-off values for future use in Whippets and supported the use of breed-specific KL/AoD ratio values for characterizing abnormal renal size in other canine breeds.

## 7.2 INTRODUCTION

Ultrasonography is a standard diagnostic test for evaluating dogs with suspected renal disease, however subjective assessments can be affected by the degree of the operator's expertise.<sup>1</sup> Previous research studies have described quantitative ultrasound methods for more objectively characterizing renal size in dogs. Some studies have correlated renal linear measurements with body weight<sup>2,3</sup> or with the length of the sixth or seventh lumbar vertebra.<sup>4</sup> Other studies have described methods for sonographically estimating the kidney volume.<sup>5-7</sup> In general clinical practice, the time necessary to perform these measurements can be a constraint and therefore renal ultrasonographic dimensions are more commonly evaluated subjectively.<sup>8,9</sup> In 2007, a new method for more quickly quantifying canine renal size was proposed: a ratio of kidney length (KL) to aortic luminal diameter (AoD).<sup>10</sup> That method was found to have good reproducibility when applied by different operators.<sup>10,11</sup> However, the main limitation of this method was the wide range of normal cut-off values, which increased the likelihood of having an overlap in values for dogs with versus without renal pathologies. One possible reason for the wide range of normal values could have been the use of different breeds, different morphologies (i.e. brachymorphic, mesomorphic and dolichomorphic), and different body weights.<sup>3,12</sup> We hypothesized that the cut-off values for a single breed of dog would be narrower and thus of greater clinical value. Primary objectives of this study were to determine normal cut-off values of the KL/AoD ratio in a sample of clinically normal Whippets and compare the results with the previously published reference values.<sup>10</sup> Secondary

objectives were to test the effects of sex, age, weight, and side on KL and of sex, age, weight, and scanning plane (longitudinal vs. transversal) on AoD.

### 7.3 MATERIALS AND METHODS

The prospective, observational, reference interval study was approved by the Clinical Ethical Review Board of the University of Naples “Federico II” (n° 64674), and performed at Interdepartmental Center of Veterinary Radiology of the University Federico II of Napoli and at three private breeding kennels. The sample size for the study was based on a prospective power analysis performed with G\*Power (v. 3.1.9.2, March 2014, Heinrich-Heine-Universität Düsseldorf, Germany) selecting correlation from the *t* tests family, applying one tail, an effect size of 0.4 (mean effect size according to Cohen) a significance level ( $\alpha$ ) = 0.05 and a power of 80%. The number of dogs meeting the inclusion criteria were enrolled in a period of time between March and December 2017. Only clinically healthy dogs and without ultrasonographic renal lesions were included. Dogs were considered to be clinically healthy if there were no history of signs consistent with renal disease and the clinical examination was unremarkable for diseases related with the urinary system. Final decisions for dog inclusion or exclusion were made by a professor of Veterinary Medicine (M.P.P.) for the clinical examinations and by a professor of Veterinary Radiology for the ultrasound examinations (L.M.). For each included dog, the following clinical characteristics were recorded by a first-year Ph.D. student (D.C.): sex, weight (in kg), age (in months) and findings from the physical examination eventually compatible with systemic disease and/or renal function

impairment (i.e. hyperthermia/hypothermia, muscle wasting, lethargy, weakness, etc.). Ultrasonography examinations were performed by a professor of Veterinary Radiology with twenty-four years of experience in ultrasonography (L.M.). Dog were physically restrained in the right and left lateral recumbent position or in a standing position at the discretion of the ultrasonographer. No sedatives were administered. Transducer-skin contact was achieved after first moistening the skin with alcohol and then applying acoustic coupling gel. The US exams were performed using one of two devices (MyLab Class C Vet or MyLab 30 Vet, Esaote, Genova, Italy), each equipped with a 3.5–10 MHz microconvex electronic transducer. Each kidney was preliminarily evaluated in order to rule out parenchymal alterations. Using previously described protocols,<sup>10</sup> the KL was measured on still images acquired in the dorsal plane (Figure 7.1A), when the distance between the two poles was maximum and, the renal pelvis clearly visible, to avoid oblique scans and consequently a possible underestimation of the kidney length. The AoD was assessed from the left side, in transversal (AoDT) and longitudinal (AoDL) scans, just caudal to the origin of the left renal artery. During the examination the operator was careful not to apply excessive pressure on the abdominal wall and compress the aorta. Measurements were made from still images acquired at the maximum luminal diameter, after reviewing cine-loop frames to account for aortic pulsation. Measurement cursors were placed at the borders of the lumen, after excluding the vessel walls (Figure 7.1B). Both the kidneys and the aorta diameters were measured in triplicate and the average values were used for statistical analyses.

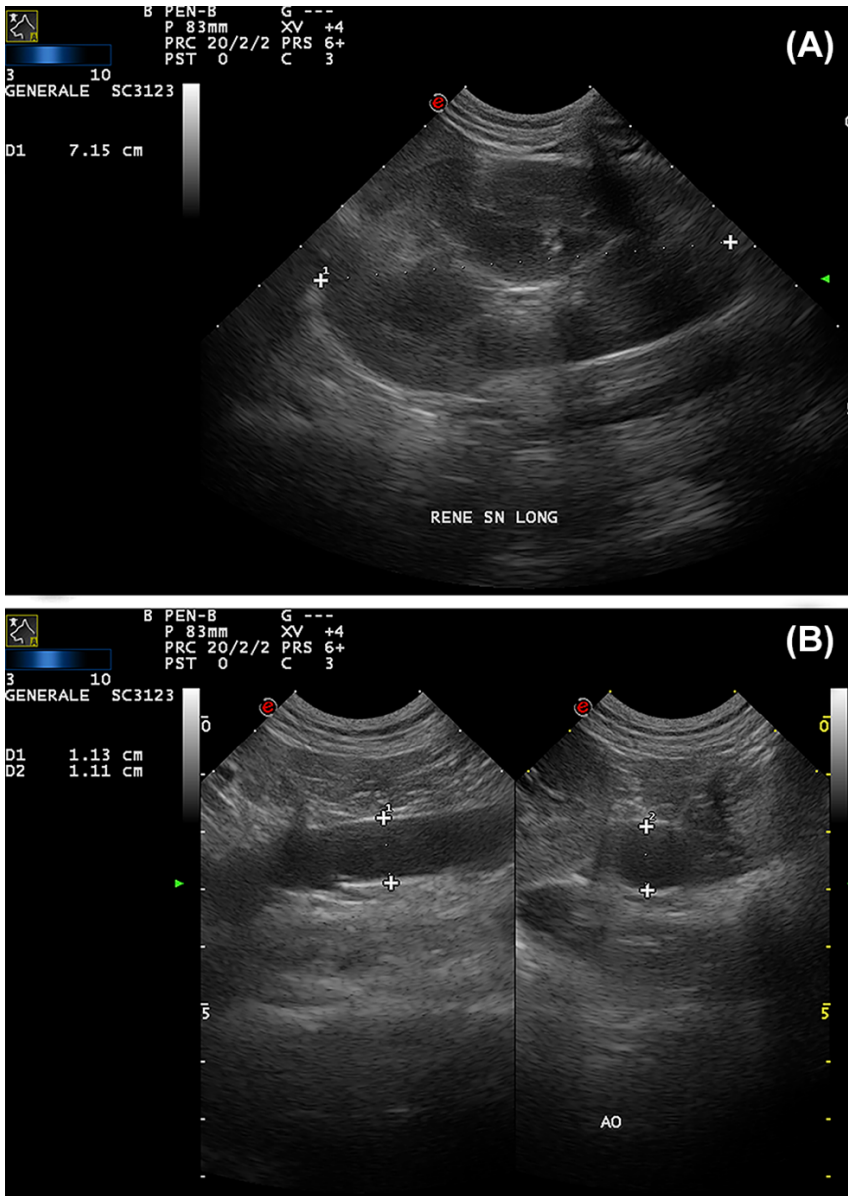


**FIGURE 7.9 (A)** Measurement of the kidney length (7.15 cm) on a dorsal ultrasound scan (patient in right lateral recumbency; multifrequency microconvex probe working at 6,5 MHz). **(B)** The abdominal aorta is scanned from the left side and the aortic luminal diameter is measured just caudal to the emergence of the left renal artery. The aortic luminal diameter is measured on longitudinal (1.13 cm) and transversal (1.11 cm) scans by placing the electronic calipers at the border of the lumen, after excluding the vessel walls.

Statistical analyses were performed by an observer with a Ph.D. degree and eight years of expertise in statistics (L.A.). Data were entered into an electronic spreadsheet (Microsoft Excel ver.16.10 2016, Microsoft Corp., Redmond, WA, USA) and statistical analyses were performed using dedicated software (IBM SPSS Statistics, v. 26.0 IBM Corporation, Armonk, NY, USA; Prism ver.7.0, GraphPad Software, Inc. La Jolla CA USA). The normality of data distribution was evaluated using the Shapiro–Wilk test. Descriptive statistics, including the mean, range (minimum to maximum), standard deviation and 95% confidence interval (CI) of the mean were calculated for KL, AoDT, AoDL, and the ratios KL/AoDL and KL/AoDT (Table 7.1).

	<b>MEAN ± SD (n =36)</b>	<b>95% C.I.</b>	<b>RANGE (Min-Max)</b>
<b>KL (cm)</b>	6.2 ± 0.7	6 - 6.4	4.9 - 8.2
<b>AoL (cm)</b>	0.94 ± 0.11	0.91 - 0.98	0.71 - 1.3
<b>AoT (cm)</b>	0.98 ± 0.1	0.95 - 1	0.78 - 1.3
<b>KL/AoDL</b>	6.7 ± 0.83	6.5 - 6.9	5 - 9.1
<b>KL/AoDT</b>	6.5 ± 0.78	6.3 - 6.7	4.1 - 8.2

*TABLE 7.10 Descriptive statistics for the kidney lengths, aortic luminal diameter and the kidney-to-aorta ratios in a sample of clinically normal Whippets. Values in the sample were normally distribute. Abbreviations: KL= kidney length; AoDL= aortic luminal diameter measured on longitudinal scans; AoDT= aortic luminal diameter measured on transversal scans; KL/AoDL= kidney-to-aorta ratio obtained from longitudinal scans of the abdominal aorta; KL/AoDT= kidney-to-aorta ratio obtained from transversal scans of the abdominal aorta; SD= standard deviation; 95% CI= confidence interval; Min= minimum ; Max= maximum.*

A mixed linear model was applied to evaluate the effects of sex, age (considered as a continuous variable), and bodyweight (as fixed principal effects) and of subject and side (as random factorial effects) on KL, KL/AoDL, and KL/AoDT; AoDT and AoDL were also assessed after adjusting for the effects of sex, age, and bodyweight (fixed effects) and of the subject (random effects). Since sex, age, and bodyweight significantly affected KL, AoDT and AoDL, the effects of age and sex were also tested within sex in a general linear model, prior to further analysis. *Post hoc* tests were selected according to variable type (continuous vs. categorical) and distribution. Differences in KL, AoDL, and AoDT between males and females were tested using the pooled Student's *t* test with Levene's test. Correlations of age with KL, AoDL, and AoDT were studied using Spearman's rank correlation coefficient ( $r_s$ ) within males and with Pearson's product moment test ( $r$ ) within females. The correlation between bodyweight and KL was studied with Spearman's rank correlation coefficient ( $r_s$ ). Correlations of bodyweight with AoDL and AoDT were studied using Pearson's product moment test ( $r$ ) within both sexes and in the whole sample. AoDL and AoDT were compared using a Bland–Altman plot and the intraclass correlation coefficient (ICC) for absolute agreement was calculated with 95% CI, using a two-way mixed model for single measurements. KL was normalized to the AoD derived from both longitudinal (KL/AoDL) and transversal (KL/AoDT) scans, and the ratios were studied using the same statistical approaches used for AoDL and AoDT. In all analyses,  $P < 0.05$  was considered statistically significant.

## 7.4 RESULTS

The power analysis yielded a samples size of 34 Whippets. A total of 39 Whippets (17 males and 22 females all intact) met all criteria for inclusion. Three dogs (2 females and 1 male) were excluded due to the presence of mild pyelectasia (2) and irregular renal contour (1). Included dogs ranged from 10 months to 14 years of age and weighed between 10 and 20 kg (mean  $14.12 \pm 2.38$  kg). The mixed linear model identified significant effects of sex ( $P < 0.0001$ ) and bodyweight ( $P = 0.029$ ) on KL, but no effects of age ( $P = 0.66$ ), subject ( $P = 0.30$ ), or side ( $P = 0.78$ ). The effect of bodyweight was independent of sex ( $P = 0.07$ ). KL differed significantly between males and females, and was longer in males ( $P < 0.0001$ ). There was no correlation between KL and age. However, there was a positive linear correlation between KL and bodyweight ( $r_s = 0.64$ ,  $P < 0.0001$ , Figure 7.2).

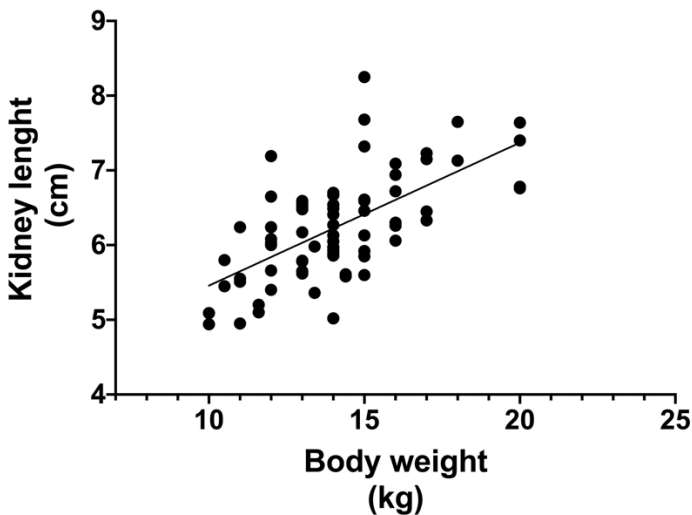
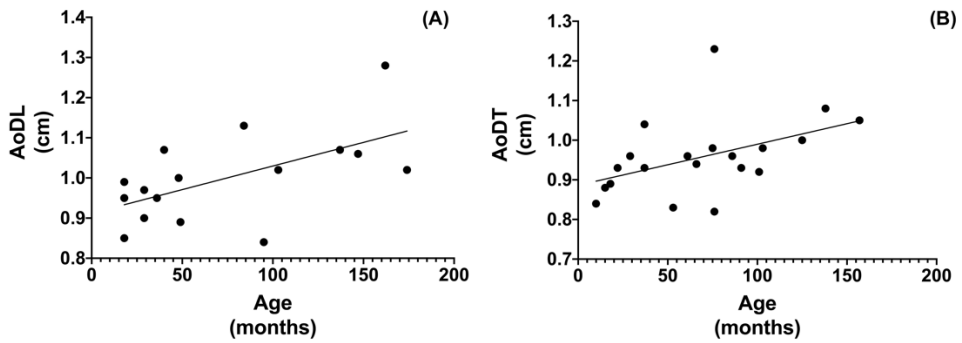


FIGURE 7.2 Correlation between kidney length (in cm) and bodyweight (in kg).

For both AoDT and AoDL, the mixed linear models found significant effects of sex ( $P < 0.0001$ ), age ( $P < 0.0001$ ), and bodyweight ( $P < 0.0001$ ). In male Whippets, both AoDL (Figure 7.3A) and AoDT were positively correlated with age ( $r_s = 0.56$ ,  $P = 0.03$ , for both). A positive correlation was also identified in females for AoDT ( $r = 0.46$ ,  $P = 0.04$ , Figure 7.3B), but not for AoDL ( $r = 0.16$ ,  $P = 0.49$ ).



**FIGURE 7.3** (A) Correlation between aortic luminal diameter measured on longitudinal scans (AoDL) and age (in months) of male Whippets. (B) Correlation between the aortic luminal diameter measured on transversal scans (AoDT) and age (in months) of female Whippets.

In all dogs combined, a significant positive correlation with age was found for both AoDL ( $r = 0.44$ ,  $P = 0.007$ ,) and AoDT ( $r = 0.30$ ,  $P = 0.07$ ,). A Bland–Altman plot showed minimal bias ( $-0.03 \pm 0.11$ ; 95% CI  $-0.25$  to  $0.17$ , Figure 7.4A) and an ICC of  $0.63$  ( $P < 0.0001$ ; 95% CI  $0.40$ – $0.77$ ) between AoDL and AoDT.

None of the effect variables included in the mixed linear model had any effect on either KL/AoDL or KL/AoDT. The Bland–Altman plot showed a bias of  $0.27 (\pm 0.73$ ; 95% CI  $-1.15$  to  $1.70$ , Figure 7.4B) and an ICC of  $0.69$  ( $P < 0.0001$ ; 95% CI  $0.49$ – $0.81$ ) between KL/AoDL and KL/AoDT.

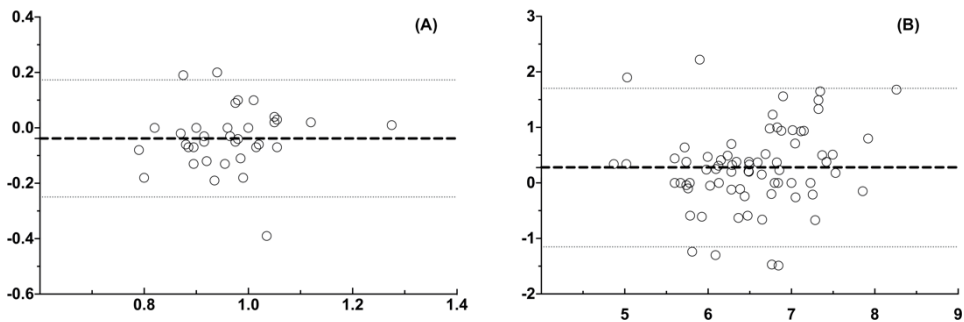


**FIGURE 7.4 (A)** Bland–Altman plot comparing the aortic luminal diameters, measured on longitudinal and transversal scans (AoDL and AoDT). **(B)** Bland–Altman plot comparing the kidney-to-aorta ratio obtained from longitudinal and transversal scans of the abdominal aorta (KL/AoDL and KL/AoDT). The y axis shows the difference between the two measurements and the x axis shows the average of both measurements. The dotted lines represent the 95% confidence intervals and the dashed line represents the bias.

## 7.5 DISCUSSION

Breed-specific findings from the current study of Whippets, as hypothesized, contributed narrower KL/AoD cut-off values than those previously proposed by Mareschal et al.<sup>10</sup> This is consistent with findings from studies of other morphometric indexes such as the Vertebral Heart Score.<sup>13,14</sup> Use of ratios with adjacent structures, categorization by body conformation (i.e. brachymorphic, mesomorphic, and dolichomorphic), or determining breed-specific values can help to maximize clinical utility.<sup>3,12.</sup>

The ultrasonographer for the current study considered the KL and AoD to be relatively easy to obtain, as previously reported.<sup>10,11</sup> The cranial margin of the right kidney was sometimes more difficult to clearly outline, due to its more cranial position within the rib cage, particularly when imaging was performed with the dog in a standing position. This position was used in some dogs to reduce the stress associated from placing them in the lateral recumbent position. Similar to previous reports,<sup>4,10</sup> the absolute length of the kidney was not significantly different between the right and left kidneys, although the right kidney was slightly larger than the left one in other studies.<sup>2,11,12</sup> The positive correlation between KL and bodyweight, as previously reported,<sup>2</sup> was also identified in our study. This was particularly notable given the fact that the bodyweights showed a fairly narrow range in our sampled dogs (10–20 kg). It has been previously reported that end-stage kidney disease and aging are associated with reductions in renal dimensions.<sup>15</sup> This would suggest that a negative correlation would occur between age and kidney dimensions. However, we found no such correlation in our study. The KL/AoD did not differ between the right and left kidney in our sampled dogs. Furthermore, even though Whippets

show marked sexual dimorphism, the KL/AoD ratio was not significantly different between the two sexes. These findings supported normalization of KL using AoD to help minimize outside sources of variability based on differences between sexes and facilitating comparability of results. Findings also supported using only one range of the KL/AoD ratio for both kidneys and both sexes.

In a previous radiographic study that compared KL relative to the body length of the second lumbar vertebra (L2), there were significant differences between dogs grouped by skull type, particularly between dolichocephalic and brachycephalic dogs.<sup>3</sup> Therefore, it is possible that the KL/AoD cut-off values obtained in the present study could be used as a reference for other dolichocephalic breeds, particularly sighthound breeds. However, given the differences in body conformation among breeds within the same skull types, and considering the high correlation between bodyweight and KL; this theory would need to be confirmed in studies of other dolichocephalic and/or dolichomorphic breeds. We did identify a positive correlation between age and AoD in our sampled dogs. This could have been due to an increase in systemic arterial pressure that occurs with aging.<sup>16,17</sup> One study found that systemic arterial pressure is significantly greater in males and in sighthound dogs (e.g. Whippets).<sup>17</sup> Another explanation could involve degeneration of vessel walls, as reported in healthy humans.<sup>18</sup> Blood pressure was not measured in dogs for the current study and may therefore warrant further investigation. The positive correlation between AoD and bodyweight likely reflected an expected relationship between AoD and the size of the dog.

We also found that the AoD measured in longitudinal and transversal scans displayed minimal bias and a high ICC. In the original study that proposed the KL/AoD ratio,<sup>10</sup> the measurements obtained from longitudinal scans showed a higher degree of agreement between different operators. That result indicated greater variability of measurements obtained using transversal scans. A proposed reason was that the ultrasound beam is never perpendicular to the long axis of the vessel in this orientation. For this reason, the authors concluded that it is preferable to measure the AoD on longitudinal scans.<sup>10</sup> In another study of dogs aged  $\leq 18$  months, the KL/AoD ratio was easier to obtain using transversal scans than with longitudinal scans.<sup>11</sup> The authors reported that this was due to motion artifacts and the small sizes of the anatomical structures. Previous studies that measured vessel diameters suggested that transversal scans may be used as exploratory scans, and recommended obtaining the measurements using longitudinal scans, since the transversal scans are affected by multiple refraction artifacts that reduce their quality.<sup>19,20</sup> In our study, we found no significant differences in AoD between the longitudinal and transversal scans, with minimal bias on a Bland–Altman plot and a large ICC. Regarding the KL/AoD ratio, although the Bland–Altman plot showed greater bias, the ICC was slightly larger and had a narrower 95% CI. In order to establish whether longitudinal or transversal scans are better for measuring AoD, we think that other imaging modalities, such as CT or MRI, are needed to provide a more objective measurement of AoD.<sup>21</sup> The main limitations of our study may include the relatively small number of dogs used and their classification as healthy on the basis of the physical examination and ultrasonographic examination alone. For the *a priori* power

analysis we selected a power of 80%, which should be considered fair in view of the inclusion of a single pure breed, and on statistical considerations *per se*. Yet, our results should be confirmed on larger samples. The dog's state of hydration and any subclinical cardiac pathologies that can affect blood pressure and, consequently, the AoD was not investigated. Furthermore, although the dogs did not show any clinical or US signs of kidney disease, we cannot exclude the possibility of subclinical kidney disease.

In conclusion, findings from the current study supported the use of breed-specific normal reference values for KL//AoD ratios. In this sample of Whippets, taking into account the 95% CI of the mean KL//AoD, a value of <6.3 could indicate decreased renal size, whereas a value >6.9 could indicate an enlarged kidney. This range (6.3 – 6.9) is narrower than the previously reported range (5.5 – 9.1),<sup>10</sup> and may help to minimize possible overlap with pathological values for future clinical patients. Although Whippets show marked sexual dimorphism, the KL//AoD ratio was not significantly different between the two sexes. Further studies are needed to obtain reference range measurements for each breed or class of dogs. Studies are also needed in order to determine the effect of hydration status and systemic arterial pressure on aorta diameter and therefore on the KL//AoD ratio.

## 7.6 REFERENCES

- 1.Hecht S, Henry GA. Ultrasonography of the urinary tract. In Bartges J, Polzin DJ. *Nephrology and Urology of Small Animals*. Wiley-Blackwell Oxford UK: 2011:128-145
- 2.Barr FJ, Holt PE, Gibbs C. Ultrasonographic measurement of normal renal parameters. *J Small Anim Pract* 1990;31:180–184.
- 3.Lobacz MA, Sullivan M, Mellor D, Hammond G, Labruyère J, Dennis R. Effect of breed, age, weight and gender on radiographic renal size in the dog. *Vet Radiol Ultrasound* 2012;53:437–441
- 4.Barella G, Lodi M, Sabbadin LA, Faverzani S. A new method for ultrasonographic measurement of kidney size in healthy dogs. *J Ultrasound* 2012;15:186–191.
- 5.Barr FJ. Evaluation of ultrasound as a method for assessing renal size in the dog. *J Small Anim Pract* 1990;31:174–179.
- 6.Nyland TG, Kantrowitz BM, Fisher P, Olander HJ, Hornhof WJ. Ultrasonic determination of kidney volume in the dog. *Vet Radiol Ultrasound* 1989;30:174–180.
- 7.Felkai CS, Voros K, Vrabely T, Karsai F. Ultrasonographic determination of renal volume in the dog. *Vet Radiol Ultrasound* 1992;33:292–296.

8.Nyland TG, Widmer WR, Matton JS. Urinary Tract. In Matton JS, Nyland TG. *Small Animal Ultrasound*. 3<sup>rd</sup> Ed. St.Louis Missouri: Elsevier Saunders 2015:557-607

9.Seiler GS. Kidneys and ureters. In Thrall D, ed. *Textbook of Veterinary Diagnostic Radiology* .7<sup>th</sup> Ed. St.Louis Missouri: Elsevier Saunders 2018:823-845.

10.Mareschal A, d'Anjou MA, Moreau M, Alexander K, Beauregard G. Ultrasonographic measurement of kidney-to-aorta ratio as a method of estimating renal size in dogs. *Vet Radiol Ultrasound* 2007;48:434–8.

11.Kawalilak LT, Pease AP, Nelson NC. Evaluation of ultrasonographically determined ratios of kidney length to aorta diameter for assessment of kidney size in healthy young dogs. *Am J Vet Res* 2019;80(8):764-770

12.Sohn J, Yun S, Lee J, Chang D, Choi M, Yoon J. Reestablishment of radiographic kidney size in Miniature Schnauzer dogs. *J Vet Med Sci* 2016;78(12):1805-1810

13.Buchanan JW, Bücheler J. Vertebral scale system to measure canine heart size in radiographs. *J Am Vet Med Assoc* 1995;206(2):194-199

14.Bavegems V, Van Caelenberg A, Duchateau L, Sys SU, Van Bree H, De Rick A. Vertebral heart size ranges specific for whippets. *Vet Radiol Ultrasound* 2005;46(5):400–403.

15. Bragato N, Borges NC, Fioravanti MC. B-mode and Doppler ultrasound of chronic kidney disease in dogs and cats. *Vet Res Commun* 2017;41:307-315.

16. Syme HM. Epidemiology of Hypertension. In Elliot J, Syme HM, Jepson RE, ed. *Hypertension in the Dog and Cat*. Springer Nature Switzerland AG 2020:67-99

17. Bodey AR, Michell AR. Epidemiological study of blood pressure in domestic dogs. *J Small Anim Pract* 1996;37:116-125

18. Sonesson B, Hansen F, Stale H, Länne T. Compliance and Diameter in the Human Abdominal Aorta – The Influence of Age and Sex. *Eur J Vasc Surg* 1993;7:690-697

19. Pasolini MP, Spinella G, Del Prete C, Valentini S, Coluccia PP, Auletta L, Greco M, Meomartino L. Ultrasonographic assessment of normal jugular veins in Standardbred Horses. *BMC Vet Res* 2019;15:343.

20. Casella IB, Presti C, Porta RMP, Sabbag CRD, Bosch MA, Yamazaki Y. A practical protocol to measure common carotid artery intima-media thickness. *Clinics* 2008;63:515–20.

21. Hoey SE, Heder BL, Hetzel SJ, Waller KR<sup>3rd</sup>. Use of computed tomography for measurement of kidneys in dogs without renal disease. *J Am Vet Med Assoc*

END OF THE DOCUMENT